M3LW-22OR0402033

Light Water Reactor Sustainability Program

Stress Corrosion Cracking of Ni-base Alloys in PWR Primary Water Containing KOH vs. LiOH

July 2022

U.S. Department of Energy

Office of Nuclear Energy

M3LW-22OR0402033

Stress Corrosion Cracking of Ni-Base Alloys in PWR Primary Water Containing KOH vs. LiOH

Ziqing Zhai
Mychailo B. Toloczko
Ferdinan C. Colon
Ryan A. Bouffioux

July 2022

Prepared for the
U.S. Department of Energy
Office of Nuclear Energy

ABSTRACT

The U.S. nuclear industry is considering replacing lithium hydroxide (LiOH) with potassium hydroxide (KOH) for pH control in pressurized water reactor (PWR) primary water for economic reasons. Among the many aspects of reactor operation that need to be assessed before switching to KOH, it is necessary to evaluate the stress corrosion cracking (SCC) response of Ni-base alloys in a KOH environment to ensure that SCC susceptibility is not increased by KOH water chemistry. In collaboration with an ongoing Electric Power Research Institute (EPRI) -led KOH qualification program, this project is performing SCC evaluations on selected materials in both LiOH and KOH-containing PWR primary water chemistries. This report documents the research progress accomplished in FY22 on this topic, focusing on the SCC growth behavior of Alloy X-750, Alloy 718 and Alloy 82H. SCC growth rates have been assessed in these materials using in-situ measurement of crack extension in PWR primary water chemistries with on-the-fly changes between LiOH and KOH, allowing uninterrupted, direct comparison of SCC growth rates of KOH vs. LiOH. To date, no obvious difference has been observed in SCC growth behavior in the tested materials between KOH and corresponding reference LiOH water chemistries.

ACKNOWLEDGEMENTS

The authors gratefully acknowledge the financial support from the Office of Nuclear Energy, U.S. Department of Energy, through the Light Water Reactor Sustainability Program Materials Research Pathway. In addition, support is recognized from EPRI for technical guidance on material selection and determination of test methods and the U.S. Nuclear Regulatory Commission for providing test systems for the SCC growth rate testing performed in this study. Dr. John Jackson and Mr. Michael Heighes from Idaho National Laboratory are acknowledged for preparing the Alloy X-750 material for this study. Dr. Dave Morton from Naval Nuclear Laboratory is acknowledged for providing the Alloy 82H material used for this study. Dr. Raul Rebak and Mr. Steve Buresh from GE Global Research are acknowledged for assisting in cold forging the Alloy 82H material. The authors would also like to acknowledge Dr. Peter Andresen (formerly with GE Global Research Center and currently with Andresen Consulting) for helpful discussions on testing details. Key technical assistance from Anthony Guzman, Michael Blazon, and Javier Gutierrez at Pacific Northwest National Laboratory is acknowledged for materials preparation activities.

CONTENTS

FIGURES

TABLES

ACRONYMS

AMS	Aerospace Material Specifications
ASTM	American Society for Testing and Materials
BOC	Beginning-of-cycle
BSE	Backscattered electron
BWR	Boiling water reactor
CMTR	Certified materials test report
CT	Compact tension
DCPD	Direct current potential drop
EDS	Energy-dispersive X-ray spectroscopy
EOC	End-of-cycle
EPRI	Electric Power Research Institute
GEGRC	General Electric Global Research Center
IG	Intergranular
INL	Idaho National Laboratory
KOH	Potassium hydroxide
LiOH	Lithium hydroxide
LWR	Light water reactor
NRC	Nuclear Regulatory Commission
PH	Precipitation-hardened
PNNL	Pacific Northwest National Laboratory
PW	Primary water
PWR	Pressurized water reactor
SAE	Society of Automotive Engineers
SCC	Stress corrosion cracking
SCCGR	Stress corrosion crack growth rate
SE	Secondary electron
SEM	Scanning electron microscopy
TG	Transgranular
UHP	Ultra-high purity
VVER	Voda Voda Energo Reactor (Russian type PWR)

Evaluation of Stress Corrosion Cracking Behavior of Ni-Base Alloys in PWR Primary Water Containing KOH vs. LiOH

1. PROJECT BACKGROUND

1.1 Objective

The LWRS task at Pacific Northwest National Laboratory (PNNL) is primarily directed at investigating the long-term stress corrosion cracking (SCC) behavior of light water reactor (LWR) component materials. The objective is to enable better lifetime performance predictions, safety assessments, and risk management during the extended operation of the nation's existing LWR fleet. The research scope is defined with regulatory and industry needs and is linked to state-of-the-art laboratory testing and microscopic characterizations.

1.2 Background of Current Study

"Western" pressurized water reactors (PWRs), i.e., those based on Westinghouse, Babcock & Wilcox, or Combustion Engineering designs and their licensed derivatives, use isotopically specific Li-7 (i.e., ≥99.94% ^{7}Li as ^{7}LiOH) for primary system pH control to reduce general corrosion and manage crud solubility, transfer, and deposition. Naturally-occurring lithium cannot be used because its ^{6}Li content would generate an untenable increase in tritium production, a significant radioactive effluent and waste concern. Due to recent difficulties encountered in procuring the isotopically-specific Li-7 that should be used to prevent tritium generation in PWRs, there is commercial interest in investigating an alternative chemical for pH control [1, 2]. Naturally occurring potassium hydroxide (KOH) has been used for this purpose in VVER (Water-Water Energetic Reactor) reactors for more than 40 years, leading to a proposal to investigate it as an alternative to LiOH to maintain pH control. However, KOH has not been qualified for use in the current "Western" PWR fleet. A key concern regarding this application is the potential effect of KOH on the structural materials employed in the reactor internals. While VVERs have not experienced unusual problems with SCC, they use few Ni-base alloys, whereas "Western" PWRs make greater use of Ni-base alloys and their welds in the primary system and pressure boundary components. Therefore, among the many aspects of reactor operation that need to be assessed before switching to KOH, it is necessary to evaluate the SCC response of Ni-base alloys in a KOH environment to ensure that SCC susceptibility is not increased by KOH water chemistry. In support of a qualification program on KOH for PWR primary coolant pH control developed and implemented by the Electric Power Research Institute (EPRI) [2], PNNL has begun SCC testing on selected Ni-base alloys in 2021 to evaluate the effect of KOH vs. LiOH on SCC initiation and growth behavior of these materials. The testing materials and water chemistry conditions were selected based on discussions with EPRI to complement the testing carried out on their own [1, 3]. The test results will help determine if a plant demonstration of the use of KOH is acceptable from a materials-related damage perspective.

1.3 Focus of Current Report

This report documents the second-year research activities on the SCC behavior of Ni-base alloys in KOH vs. LiOH containing PWR primary water. The testing materials and the evaluated water chemistry conditions were selected based on discussions with EPRI, who is organizing a qualification program to assist the US PWR utilities in a potential transition to KOH. SCC growth behavior is being evaluated on compact tension (CT) specimens with on-the-fly changes between LiOH- and KOH-containing

beginning-of-cycle (BOC), end-of-cycle (EOC), and mid-cycle water chemistries. Direct current potential drop (DCPD) technique is used for in-situ monitoring of crack extension, allowing direct comparisons of the effect of KOH vs. LiOH on the SCC crack growth behavior of the tested materials. To date, no significant effect of KOH vs. LiOH has been observed during the completed evaluations.

2. EXPERIMENTAL METHODS

This chapter provides a detailed description of the SCC crack growth testing approach we used for this study. A special focus will be given to explain how on-the-fly water chemistry change between KOH and LiOH was performed during SCC growth rate testing, which enables a direct comparison of the effect of KOH vs. LiOH without disrupting the test. In addition, microscopy characterization techniques used in this study will also be introduced.

2.1 SCC Crack Growth Test Systems and Testing Approach

2.1.1 Overview of SCC Crack Growth Test Systems

Although the LWRS SCC initiation test systems can be converted to perform stress corrosion crack growth rate (SCCGR) evaluations, they are fully occupied in FY21 by SCC initiation testing of cold-worked Alloy 690 and Alloy X-750. As a result, two U.S. Nuclear Regulatory Commission (NRC) owned SCCGR test systems were borrowed under an agreement to investigate the effect of KOH vs. LiOH on the SCC growth behavior of Alloy X-750 and Alloy 718.

The NRC SCCGR test systems at PNNL were designed and constructed to measure crack length under well-defined material and environmental conditions and ensure that the growth rate response is reproducible and characteristic of the test conditions. An example of the SCCGR test system is shown in Figure 1. Detailed information on the development of these test systems can be found elsewhere [4]. However, two key features of these test systems are reviewed here because they are important to the KOH vs. LiOH evaluations.

Firstly, crack length is measured in-situ. This has high value because it allows for evaluating SCCGR response before and after "on-the-fly" changes in environmental conditions. For SCCGR testing, it is the best means to ensure that a measurement is not affected by extraneous parameters associated with alternative approaches such as stopping a test to change water chemistry. On-the-fly evaluations are also time and cost-efficient.

Secondly, control of ion species in the test system recirculating water loop is attained using a mixed bed demineralizer. For testing in simulated standard PWR primary water, a controlled amount of boric acid and lithium hydroxide are introduced to the demineralizer. An amount is selected such that stable B and Li values are attained in the test system water, i.e., the demineralizer neither absorbs nor releases B and Li as the water passes through it when no other ions are present. The relevance to the KOH evaluation effort is that this approach to PWR primary water chemistry simulation requires preparing a dedicated demineralizer for each water chemistry to be investigated. It also requires a carefully planned procedure for swapping out water on-the-fly. This approach will be discussed in detail in the next section.

Figure 1. The typical SCCGR test system used at PNNL.

2.1.2 General SCC Crack Growth Testing Approach

Although the PNNL SCCGR test systems have been designed for use with both 1T and 0.5T CT specimens, the primary specimen geometry used in this project is the 0.5T CT with side grooves. The details of the specimen geometry are shown in Figure 2. Before loading a specimen in the autoclave, the sample thickness, notch depth, and width values are all measured and recorded into the data record for the test. Using the sample dimensions and the yield strength (YS) of the specimen at the test temperature, following American Society for Testing and Materials (ASTM) Standard E-1681, an upper limit on the value of the stress intensity (K) is calculated using the formula:

$$K = \sigma_{ys}\sqrt{D/1.27} \quad (1)$$

where σ_{ys} is the YS at the test temperature and D is the smallest of the specimen thickness, the remaining uncracked specimen width, and the crack length. In the case of materials with large amounts of work hardening (where the ratio of ultimate tensile strength to yield strength is greater than 1.3), such as annealed 300-series stainless steels and Ni-base alloys, the average of the yield and ultimate stress is used in place of the YS following ASTM guidelines. This value is not considered a strict limit but rather provides a reference point for what may be considered a high-stress intensity for a given material.

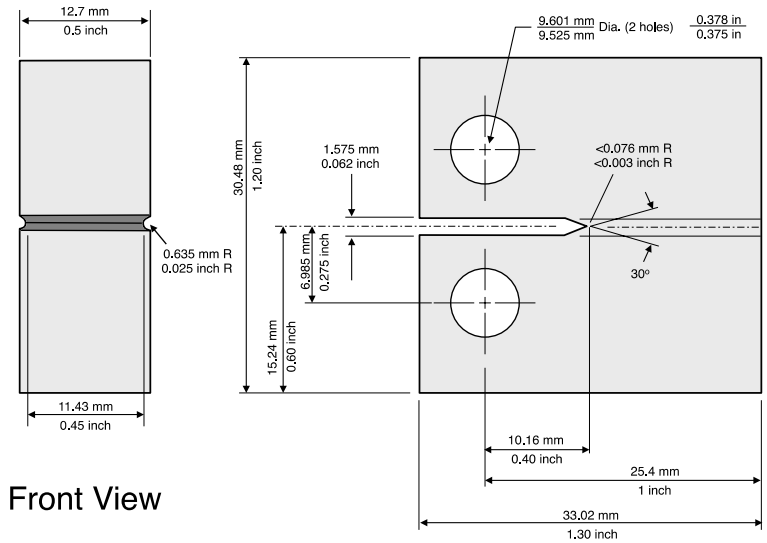

Figure 2. Schematic drawing of a 0.5T CT specimen. Oversized loading holes (~9.5 mm diameter) are used to accommodate ceramic inserts that provide electrical isolation between the CT specimen and clevises. The dimensions for 1T CT specimens are approximately double.

Crack growth tests are usually performed with two specimens loaded in series into a test system, allowing a greater range of material conditions to be examined in a shorter period of time, or to assess test reproducibility by using two samples from the same material condition. After the sample dimensions are measured, and spot-weld locations are marked on the sample, it is cleaned and inserted into a test system. Precracking of a sample is done in situ at the test temperature when a single specimen is being tested. Initial precracking of two or more specimens mounted in series is impossible in situ because the length of time needed to nucleate a precrack is inconsistent. Consequently, precracking two specimens in series would likely lead to specimens having different precrack lengths. The differing precrack lengths would make it impossible to maintain and control the K level in both specimens during and after precracking. Thus, the approach for testing at PNNL is to nucleate a crack individually on each of the two specimens under fatigue in air, followed by continued precracking of the two samples loaded together in situ. Crack transitioning steps are carefully selected to grow the precrack in high-temperature water using the following stages: (1) fatigue, (2) corrosion fatigue, and (3) SCC. Typically, this means producing initial precracks of ~1 mm in air followed by an additional ~1 mm by cycling in situ before transitioning to slow cyclic loading plus hold times to promote SCC. An Instron servohydraulic test frame is used to precrack CT specimens in air, and the same DCPD electronics and system control software used for the crack growth systems is also used for the Instron test frame.

The first step in precracking is to cycle the sample at a relatively high frequency (2–10 Hz) with a large load ratio (R) and K_{max} less than or equals to the K level chosen for constant K. As the crack begins to grow from the notch, R is increased and frequency is reduced while the K_{max} value is increased. By precracking in this way, each precrack segment can grow beyond the plastic zone created by the previous segment. For all samples, cyclic loading steps at 0.1 Hz down to 0.001 Hz are performed in high-temperature water. The final phase involves crack transitioning by very slow cycling with a hold time ranging from 1 h to 24 h. This grows the crack beyond the precracking plastic zone and allows the crack to transition from transgranular (TG) fatigue to the crack growth morphology that normally occurs under constant K conditions. Depending on the material susceptibility, this may be either TG or intergranular (IG) cracking. For materials such as Alloy X-750 and Alloy 718 that readily undergo intergranular SCC growth in LWR environments, obtaining a steady SCC growth rate after transitioning to constant K can easily be accomplished by following a standard procedure, which will be presented later in Chapters 4 and 5.

2.1.3 Uncertainties in Crack Growth Data Measurements

While the noise resolution of the PNNL DCPD test method is more than ±3 μm and allows for establishing trends in the CGR down to ~$5x10^{-10}$ mm/s, the accuracy of these rates depends on some factors that cannot be fully assessed. For example, crack front irregularity can affect the DCPD-measured growth rate. Still, there is no way to document the variation in the shape of the crack front as the crack grew; therefore, this effect cannot be accurately included in post-test crack length corrections. Another issue is that it is often impossible to uniquely identify each test phase on a crack surface after the test has ended. As a result, the post-test correction is typically based on the entire in situ portions of the test. An additional complication is the effect of ligament or contact formation on constant K crack growth. Even though attempts are made during the test to assess these effects, there are no post-test means of assessing exactly how well this method works. Crack growth testing experience and interactions with the international expert community have produced many insights into issues, but many uncertainties cannot be effectively quantified. Based on our experience, state-of-the-art testing methods, and data analysis approach, we believe overall uncertainties for crack growth-rate measurements are on the order of ±50% for SCC-susceptible materials with steady growth response. Uncertainty in reported stress intensity for a relatively straight final crack front is ≤10% after correcting for observed crack length. Still, for a highly uneven final crack, the local variability is not easily quantified and may be substantial.

2.1.4 Water Chemistry Control for the KOH vs. LiOH Study

This study aims to produce quantitative SCCGR data through in-situ measurement of crack length in KOH-based water chemistries and in corresponding reference LiOH-based water chemistries that will serve as the point of comparison. The water chemistries to be evaluated in the SCC growth rate testing were determined by EPRI with details listed in Table 1. The effects of KOH relative to LiOH will be evaluated in the beginning of cycle (BOC) water chemistry and the end of cycle (EOC) water chemistry. A mid-cycle water chemistry will also be evaluated. This mid-cycle B/K chemistry is being evaluated because B-10 decays by thermal neutron absorption during reactor operation to produce Li-7: $^{10}B(n,\alpha)^{7}Li$ [1]. LiOH and KOH concentrations were selected to provide neutral pH at 310°C. pH at the 360°C test temperature is slightly basic. For these particular bases, this occurs at molar-equivalent concentrations.

Table 1. Nominal PWR primary water chemistries identified by EPRI for the KOH vs. LiOH study.

Environment	ppm B, ppm Li, or ppm K	pH(310°C)	pH(360°C)
BOC	1500 B / 2.2 Li	7.0	8.39
	1500 B/ 12.4 K		
EOC	10 B / 0.23 Li	7.0	8.26
	10 B / 1.30 K		
Mid-cycle	1000 B / 3.3 K + 1.0 Li	7.0	8.36

The key to the test is to make on-the-fly changes between Li- and K-containing water chemistries with no change in any other conditions. By following this methodology, a direct comparison of SCCGR of KOH vs. LiOH is obtained with no other changes to the test. To achieve this, the desired test system water and corresponding demineralizer filters were prepared beforehand. Mixed bed demineralizer filters were equilibrated to the designated chemistry at room temperature by circulating deaerated water through a loop with the demineralizer and adding the corresponding chemicals until the desired B and Li or K values are attained and are stable.

To gain experience and ensure that the on-the-fly water chemistry changes would be successfully implemented during testing, a water chemistry change trial from 1500 ppm B/2.2 ppm Li to 1500 ppm B/12.4 ppm K and then to 10 ppm B/0.23 ppm Li was performed before the start of the actual tests. All

the other environmental conditions (e.g., temperature, dissolved hydrogen, etc.) were set to the same target values used in the test. A simplified water board setup in preparation for these changes is illustrated in Figure 3. The on-the-fly changes were accomplished by draining 95 volume% of the old solution inside the water column and then switching the inlet flow to draw water from the prepared new deaerated solution in a five-gallon container. This refills the water column and pushes the new solution through the autoclave and the water board. In addition, the solution being purged from the autoclave was decanted into a disposal container during all autoclave volume exchanges using the outlet before reaching the demineralizer filter (Figure 3). This process is repeated approximately for 5–6 autoclave volume exchanges. The first three exchanges take place with the demineralizer valved out from the water chemistry control board. After the third volume exchange, a demineralizer configured for the new target water chemistry is valved in. Table 2 summarizes the evolution of monitored environmental parameters during the entire process of an on-the-fly water chemistry change trial run from 1500 ppm B/2.2 ppm Li to 1500 ppm B/12.4 ppm K. The changeover usually took ~5 hours to complete, but 24 hours was given for the system to equilibrate. Whether the final concentration of the solution is on par with the target can be determined by acquiring a water sample after the equilibration is reached.

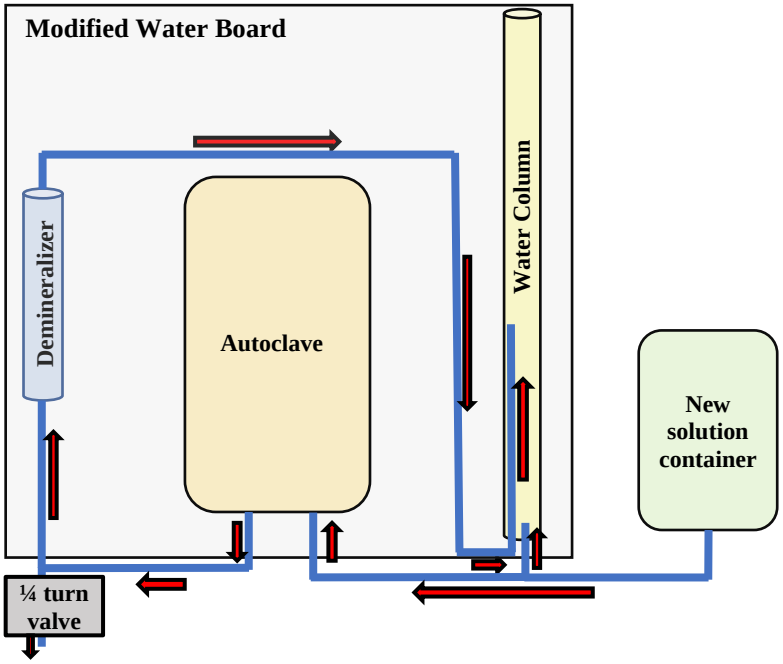

Figure 3. Simplified schematic of the modified water board setup for on-the-fly chemistry changes used in the SCCGR test system. The red arrows indicate the direction of the water flow.

Table 2. Environmental parameter tracking at each autoclave volume exchange during the trial on-the-fly water chemistry changeover from 1500 ppm B/2.2 ppm Li to 1500 ppm B/12.4 ppm K.

Vol. change #	Resistivity (Kohm-cm)	Conductivity (µS/cm)	pH	Temp (°C)	B content (ppm)	Li content (ppm)	K content (ppm)
0	47.32	21.13	6.15	23.45	1512	2.19	0
1	38.78	25.79	N/A	24.89	N/A	N/A	N/A
2	36.62	27.31	N/A	24.97	N/A	N/A	N/A
3	35.17	28.43	N/A	25.00	N/A	N/A	N/A
4	33.90	29.49	N/A	24.94	N/A	N/A	N/A
5	29.83	33.52	6.09	23.55	1637	~ 0	12.97
6	30.21	33.10	6.18	23.49	1501	~ 0	12.77

2.2 Microstructural Characterizations

2.2.1 Pre-Test Examinations

2.2.1.1 Matrix Microstructure Examination

Both optical microscopy and scanning electron microscopy (SEM) were utilized to document the microstructure of materials investigated in this study. Three ~10×10 mm pieces were sampled to allow documenting the microstructure in the "A", "B", and "C" observation directions of the Alloy X-750 and Alloy 718 materials following the designation specified in Figure 4.

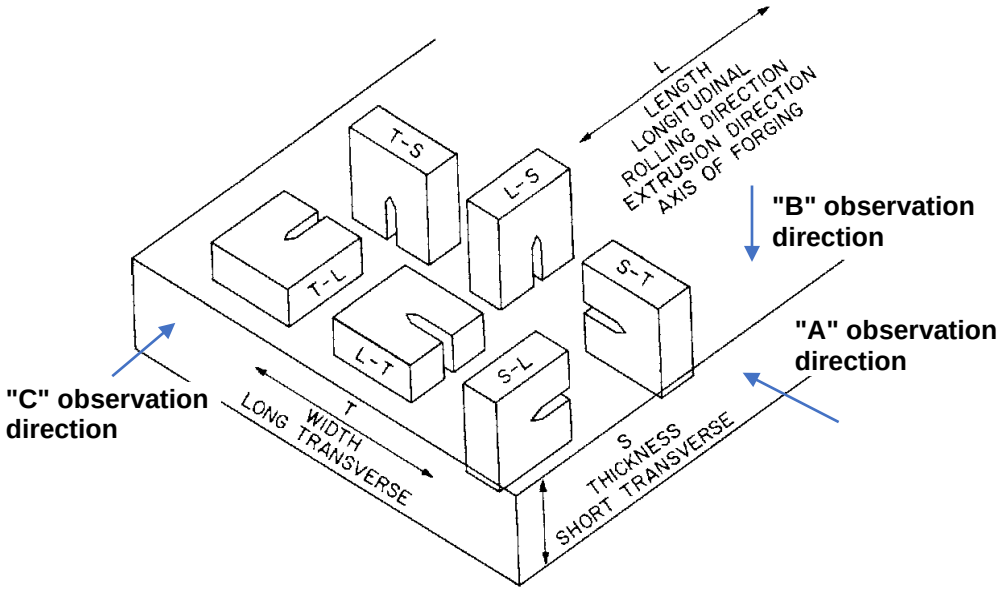

Figure 4. Definitions of the S-L, T-L, and S-T crack growth planes relative to plate fabrication conditions. The first letter indicates the loading direction, and the second letter indicates the crack growth direction in that plane. "A", "B", and "C" observation directions are noted.

The metallographic examinations of the materials were performed using an Olympus BX51M optical microscope with DP74 camera to examine grain size, precipitate distribution, and the presence of banding. The samples were polished to a colloidal silica finish and then dip-etched for ~1 min in Kalling's #2 etchant (100 mL ethanol, 100 ml HCl, 5 g $CuCl_2$) to reveal grain boundaries and precipitates. Large mappings of an area of ~6×4 mm were acquired on all three planes under darkfield conditions at a resolution of 0.59 μm/px for each optical micrograph. Acquisition routines were performed using Olympus Stream v2.2 software for stage control and collage assembly.

High-resolution SEM examinations were performed on all non-etched samples to identify intragranular and IG precipitates and confirm microstructure. This task was performed using a JEOL 7600F scanning electron microscope with most images acquired at a low-kV backscattered electron (BSE) mode. Energy-dispersive X-ray spectroscopy (EDS) was also employed to help identify the type of precipitates found in the materials.

2.2.1.2 Pre-Test Examination of CT Specimens

Prior to the SCC growth rate testing, all CT specimens were fatigue pre-cracked in air. Since two specimens from each material were loaded in series for testing, a decision must be made on which one is the controlling sample during the test for active load control implementation. To facilitate the decision-

making, the side grooves of all specimens were highly polished before the air fatigue precracking so that the crack to-be-produced could be clearly visualized under microscopes. The polishing was completed in two phases. In the first phase, sandpaper with increasing grades from #400 to #1200 was wrapped around a stick to manually remove the affected surface during the electrical discharge machining of the CT specimens. Then a small dremel with a felt head was used to sequentially polish the side grooves using diamond paste down to a 1 μm finish. Upon the completion of air fatigue precracking, both side grooves of every specimen were examined under the Olympus BX51M optical microscope for crack length measurement. The specimen that exhibited more even crack length in both side grooves among the two from the same material was selected as the controlling specimen for the SCC growth rate tests.

2.2.2 Post-Test Specimen Examinations

Post-test characterizations focus on examining the crack growth surface after the specimens were fatigue opened in air, and water bathed in deionized water to remove loose corrosion products deposited on the crack surface. The examination started with using the same optical microscope mentioned above to record crack growth surface morphology and measure crack extension (both pre-crack and environmental crack) in each specimen. This was followed by SEM examination using the JEOL 7600F scanning electron microscope to document high-resolution montage imaging of each specimen's entire crack growth surface. Topology data were acquired in high-kV, secondary electron (SE) mode that allows for detailed examination of cracking morphology [intergranular (IG) vs. transgranular (TG)]. Compositional data were acquired in low-kV, BSE mode that utilizes the relatively shallow interaction volume compared to high-kV in an effort to capture the different thickness in the oxide layer formed on the crack growth surface, which can facilitate differentiation of the different stages during an SCC growth rate test.

3. TESTING MATERIALS

Based on discussions with EPRI, Alloy X-750, Alloy 718, and Alloy 82H were selected for the SCC testing on the effect of KOH vs. LiOH at PNNL. Alloys X-750 and 718 are high-strength Ni-base alloys commonly used in LWRs for springs and fasteners, often in situations close to the fuel where irradiation exposure is high. They were often chosen for their high strength, general corrosion resistance, and resistance to irradiation-induced relaxation. In addition, while Alloy 600 and its weld metal Alloy 182 have already been evaluated by EPRI as part of their qualification program on KOH for PWR primary coolant pH control [3], Alloy 82H, another compatible weld metal of Alloy 600, had not been studied. Therefore, a due-diligence study is also performed on Alloy 82H in this research. The Alloy X-750 material evaluated in this study is a commercial Alloy X-750 heat originally sourced from a utility by EPRI with known susceptibility to SCC. The Alloy 718 material used for this study was fabricated by Special Metals and was purchased in a solution annealed condition. An LWR-relevant thermal treatment was applied in-house. The Alloy 82H material investigated in this study was acquired from Naval Nuclear Laboratory (NNL) and has received a post weld heat treatment (PWHT). In this chapter, the thermal-mechanical history and microstructure of these testing materials will be provided. The selection of testing orientations for SCC initiation and crack growth specimens will also be presented.

3.1 Alloy X-750

3.1.1 General Information of the Selected Heat

The Alloy X-750 material used for this study was purchased from Southern Co. by EPRI. Originally intended for a boiling water reactor (BWR) core shroud tie rod repair, it was removed from a spare upper support bracket and sent to GEGRC and Idaho National Laboratory (INL) for fracture toughness and SCC evaluation in BWR environments [5, 6]. As part of an EPRI's BWR Vessel and Internals Project, the bracket was dissembled, and one of the arms was sectioned into several parts (Figure 5) for detailed characterizations. The support bracket was machined from a 51.3 mm thick by 1219 mm wide by 2438 mm long plate of Alloy X-750 from Haynes International heat 2750-5-7656. The heat chemistry shown in Table 3 is from the certified materials test report (CMTR). Alloy X-750 is a gamma prime (γ') (Ni_3[Ti,Al]) precipitation strengthened superalloy designed for high-temperature strength, oxidation, and creep resistance and is used in structural support applications for LWRs. The composition of Alloy X-750 is close to that of Alloy 600 except for higher contents of titanium (Ti), aluminum (Al), and additions of niobium (Nb), which are the primary strengthening elements. High strength is developed by heat treatment after solution annealing that leads to a homogeneous distribution of gamma prime precipitates that are coherent with the austenite matrix. Among the choices of heat treatment available for Alloy X-750, two have been used extensively: a two-step thermal treatment at 885°C and 704°C (AH), or a high-temperature solution annealing at ~1100°C followed by single-step aging at 704°C for 20 hours and air cool (HTH) [7, 8]. The latter optimizes the precipitation of grain boundary carbides that appears to confer maximum resistance to PWSCC provided thermal aging is preceded by at least 40% cold work. The heat treatment condition of the as-supplied plate was not specified. A subsequent full heat treatment was performed by INL and consisted of a solution anneal step at 1107°C for 1 hour, followed by a water quench, and then a γ' precipitation heat treatment of 704°C for 20.25 hours.

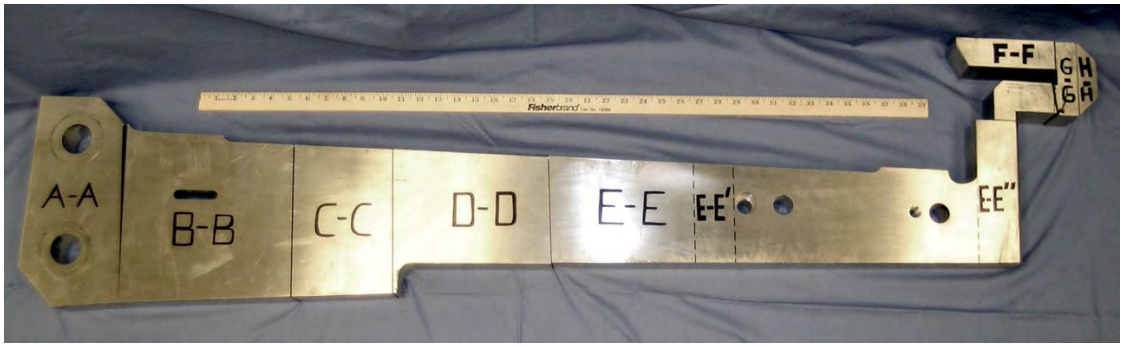

Figure 5. Primary sections cut from one arm of Alloy X-750 stabilizer support bracket [9].

Table 3. Chemical composition (wt. %) taken from the certified material test report of Alloy X-750 heat 2750-5-7656, obtained from billet end compared to the Alloy X-750 specifications. One element name in the document was illegible.

Element	Alloy X-750 Specification	Alloy X-750 Heat 2750-5-7656
C	<0.08	0.04
Cr	14-17	14.99
Fe	5-9	7.80
Mn	<1	0.197
Ni	>70	70.83
Ti	2.25-2.75	2.42
Al	0.4-1	0.77
Co	<1	0.726
P	<0.008	<0.005
Cu	<0.5	0.0151
S	<0.01	0.002
Si	<0.5	0.253
Nb+Ta	0.7-1.2	0.99 (Ta: <0.01)
Unreadable element name in the CMTR		0.976

3.1.2 Characterizations of the Alloy X-750 Material

Macrostructural and microstructural analyses were performed at GEGRC on metallographic samples taken out from all sections for the Alloy X-750 stabilizer support bracket (Figure 5) [10]. The description of these features provided here largely follows their reported observations. Overall banding was observed throughout the support bracket in terms of both grain size banding and carbide banding, with a representative example shown in Figure 6. It features alternating regions of significantly different grain sizes produced during the fabrication of the plate. It also features prevalent carbide banding. The carbide banding appears as wavy lines of black specks that vary in density. Closer examinations revealed that the small spherical-shaped particles that compose the carbide atmospheres in the bands are secondary MC-type carbides. Larger primary M(C,N) carbonitrides with a blocky morphology are also present in the bands but at lower densities (Figure 7).

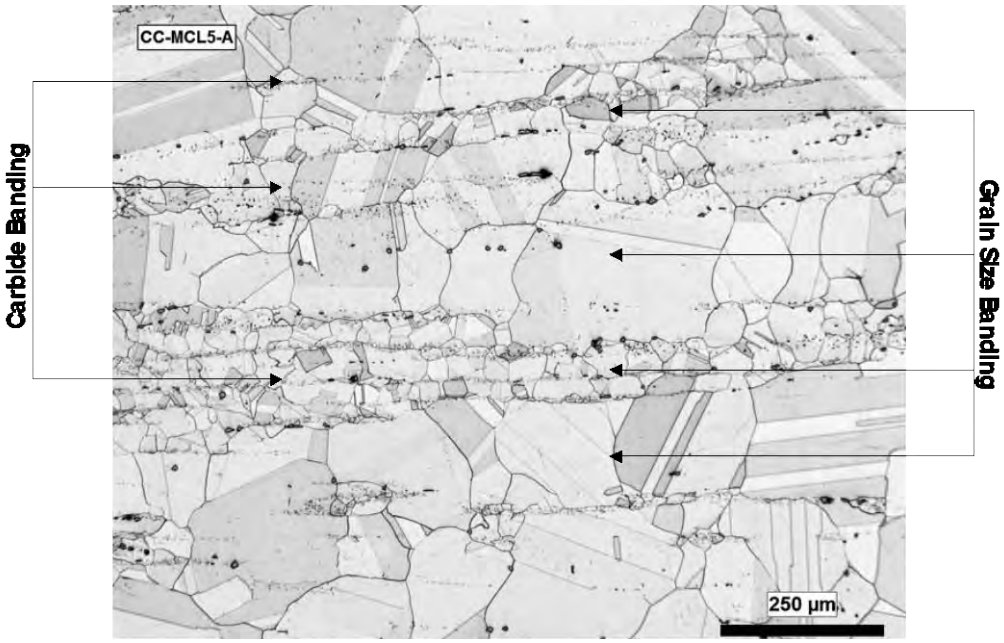

Figure 6. Representative optical micrograph from GE of Alloy X-750 taken from section C-C longitudinal orientation with grain and carbide banding identified [9].

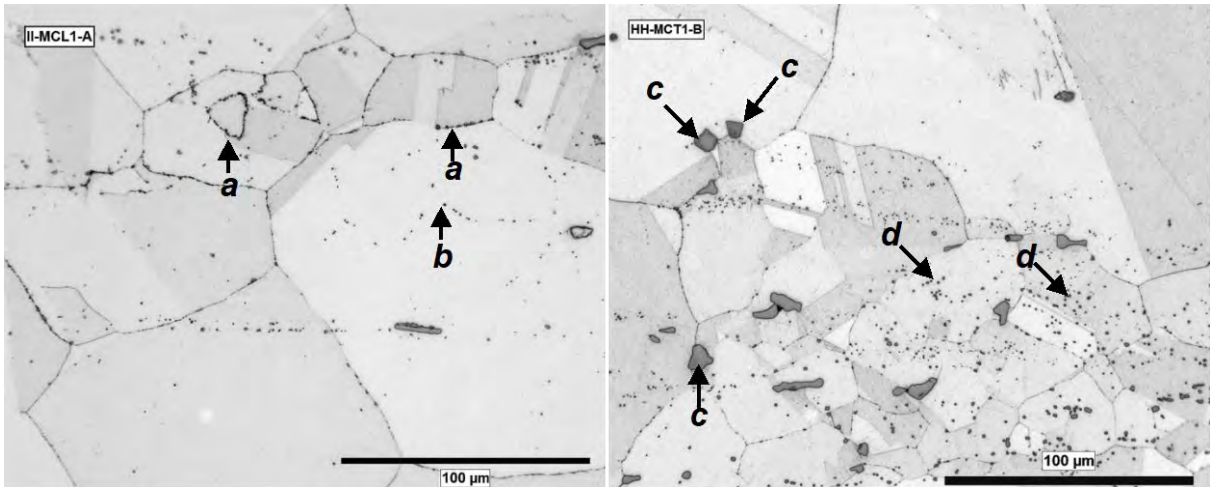

Figure 7. Second phases in GE-acquired optical micrographs of the Alloy X-750. a) grain boundaries decorated with secondary MC-type carbides, b) prior grain boundaries decorated with MC-type carbides, c) primary M(C,N) carbonitrides, d) secondary MC-type carbides [9].

With the facilitation of EPRI, PNNL acquired a leftover block from the C-C section from INL for the current study (Figure 8). Heavier banding has been reported for this section as compared to other sections [9]. To confirm the microstructure, macroscopic optical analysis of the S, L, and T planes (relative to the plate production direction) in cross-section was performed at PNNL on the acquired block following the designation specified in Figure 4. As shown in Figures 9-11, extensive banding microstructures in the S plane can be seen in this material. While often appearing concurrently, carbide banding tends to be more prominent than the bands of finer grains, especially when viewed in the "A" direction. Bands of high-density carbides usually repeat within every 300 µm in the short-transverse direction and exhibit a length of 100s of micrometers to more than 1 mm in the longitudinal direction regardless of the grain size

(Figure 9). In the "B" observation direction, a one-to-one correlation between fine-grain clusters and ultra-dense carbide atmospheres was observed (Figure 10). The "C" observation direction features strata-like carbide banding, with the carbide banding appearing more prominent than in the "A" observation direction. In addition, the carbide banding often extends across the entire width (~4 mm) of the field of view (Figure 11). This information helped determine the specimen orientation for SCC testing and is expected to be useful for interpreting the SCC initiation and crack growth behavior observed in the specimens, which will be discussed later.

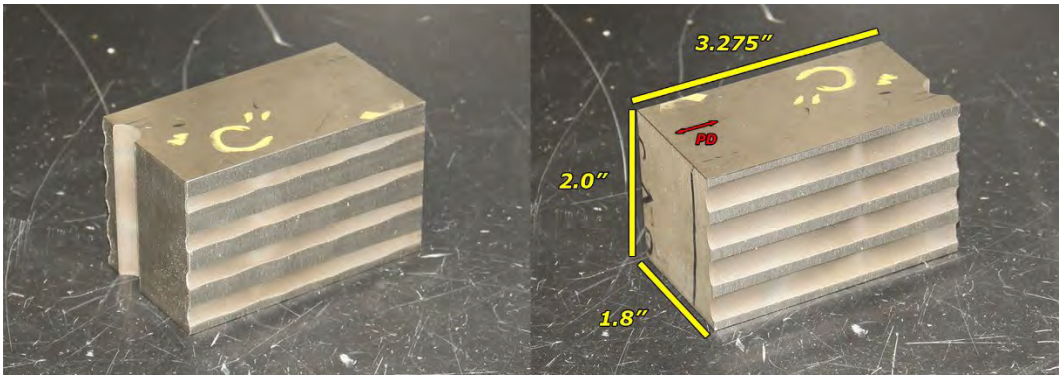

Figure 8. The Alloy X-750 block (heat 2750-5-7656) from Section C-C in Figure 5 received by PNNL for the KOH vs. LiOH primary water chemistry study. The dimensions are specified in inches in the image. “PD” = plate fabrication processing direction.

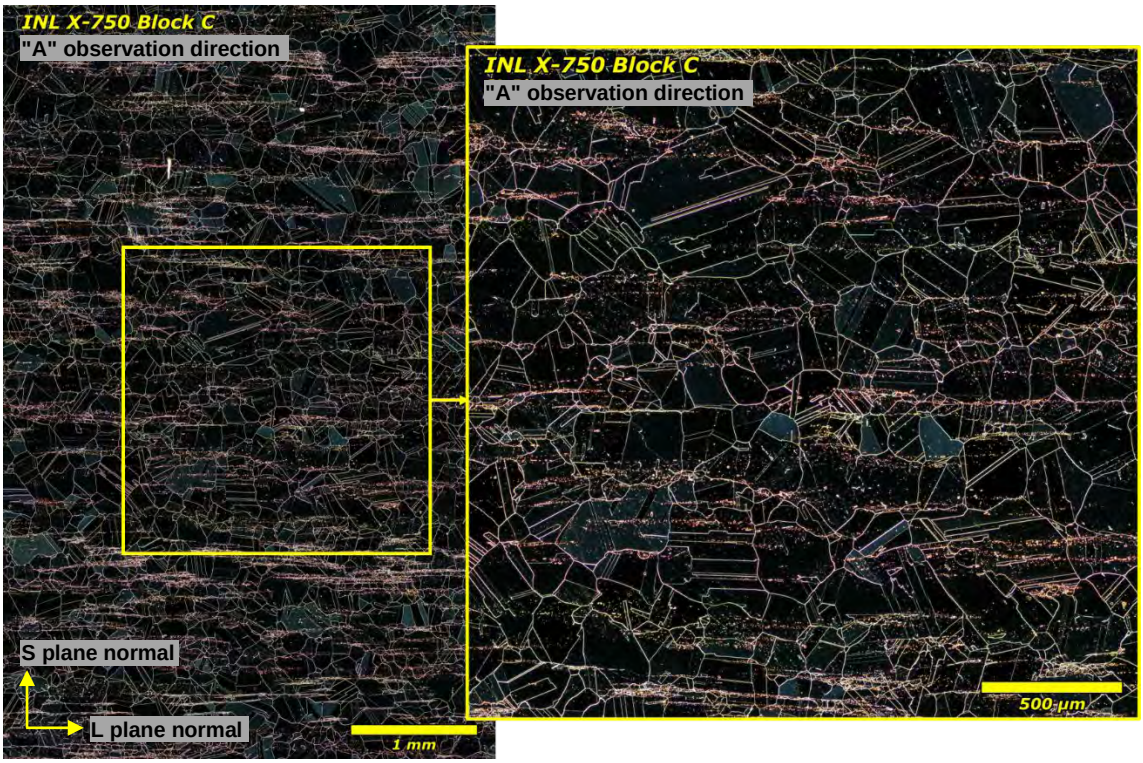

Figure 9. Representative optical micrograph of the banding microstructure revealed in the "A" observation direction of the Alloy X-750 block received from INL (heat 2750-5-7656).

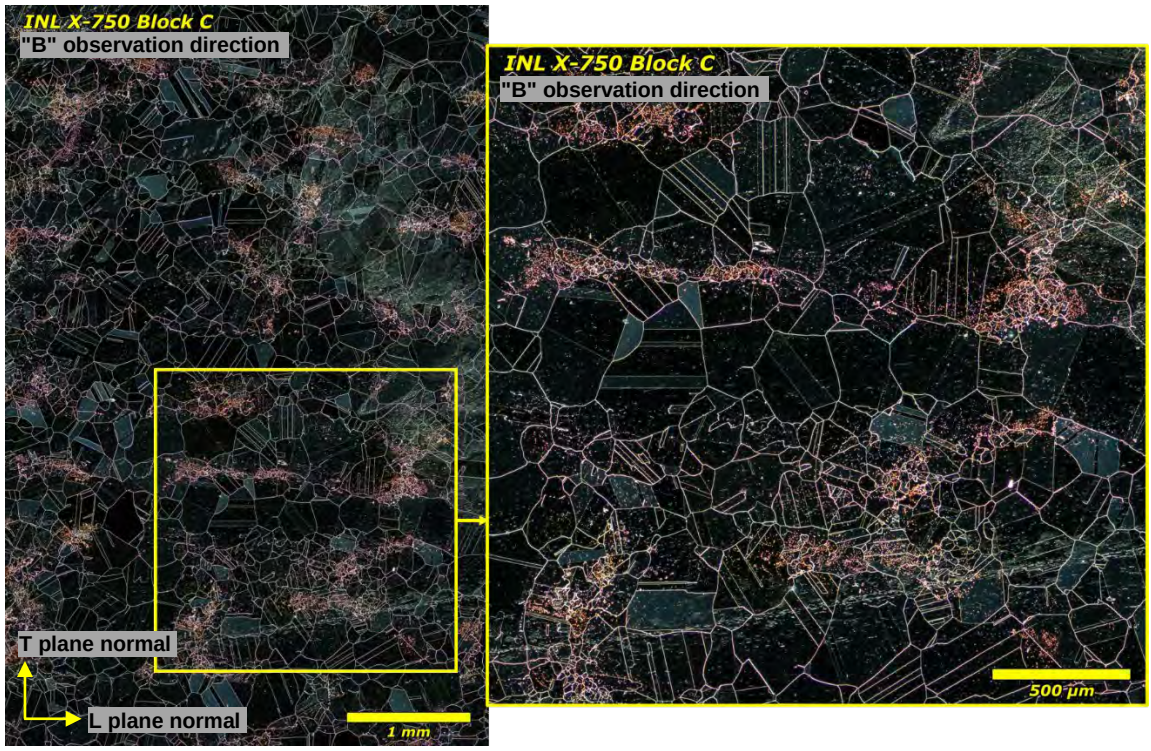

Figure 10. Representative optical micrograph of the banding microstructure revealed in the "B" observation direction of the Alloy X-750 block received from INL (heat 2750-5-7656).

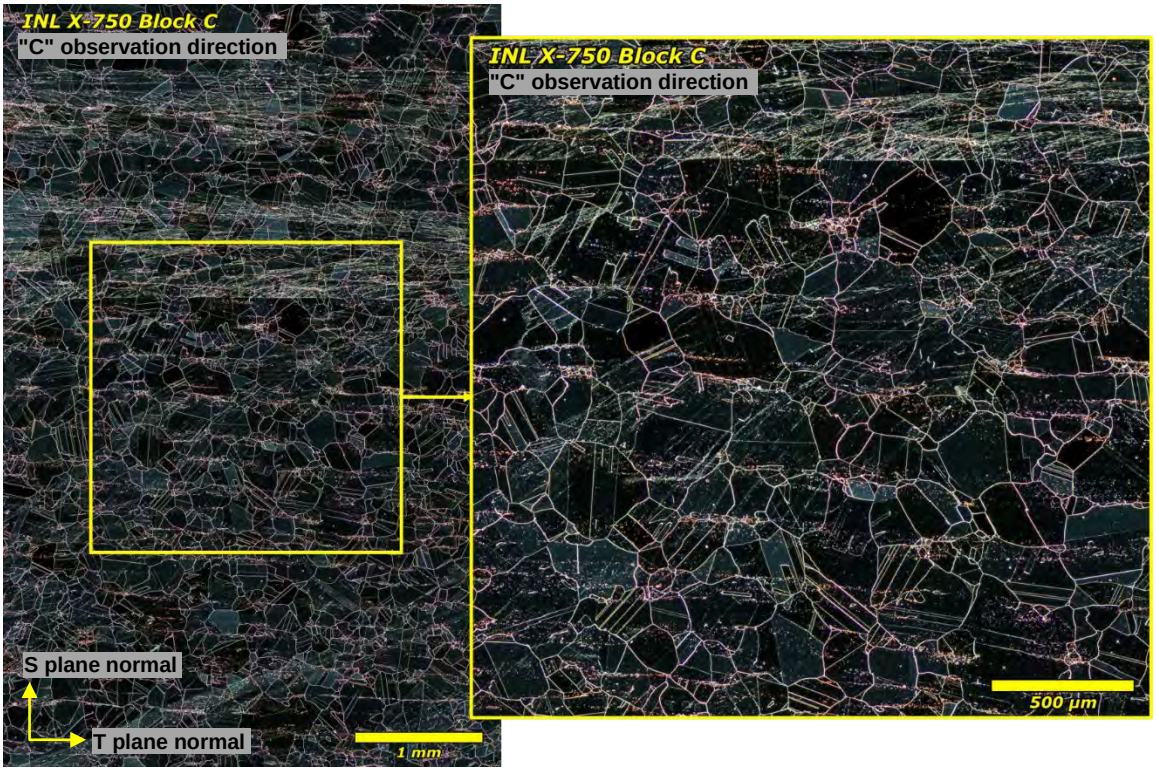

Figure 11. Representative optical micrograph of the banding microstructure revealed in the "C" observation direction of the Alloy X-750 block received from INL (heat 2750-5-7656).

SEM examinations were also performed at PNNL to examine the distribution and type of precipitates in the received Alloy X-750 block, with a focus on IG phases in the fine-grain banding regions as seen in the "A", "B", and "C" observation directions. Samples polished to a colloidal silica finish were used for this purpose. Representative microstructures and grain boundary precipitates are shown in Figures 12 and 13. The high-energy grain boundaries feature a fine disperse of <100 nm precipitates with occasional larger phases of ~500 nm – 1 μm in size. Qualitative SEM-EDS analysis suggested that the fine precipitates are mostly $Cr_{23}C_6$ type carbides and the larger phases are Nb/Ti-rich carbides (Figure 14). High-resolution characterizations performed by GEGRC revealed a duplex γ' size distribution of 5 and 25 nm at grain boundaries, which is consistent with the HTH heat treatment with some variation in the solution annealing process used [9]. Unfortunately, these γ' phases were not resolved at PNNL using the current SEM and EDS imaging conditions. More detailed characterizations using alternative sample preparation techniques such as special etching as GEGRC did, or TEM analysis are planned to better record these fine-size phases.

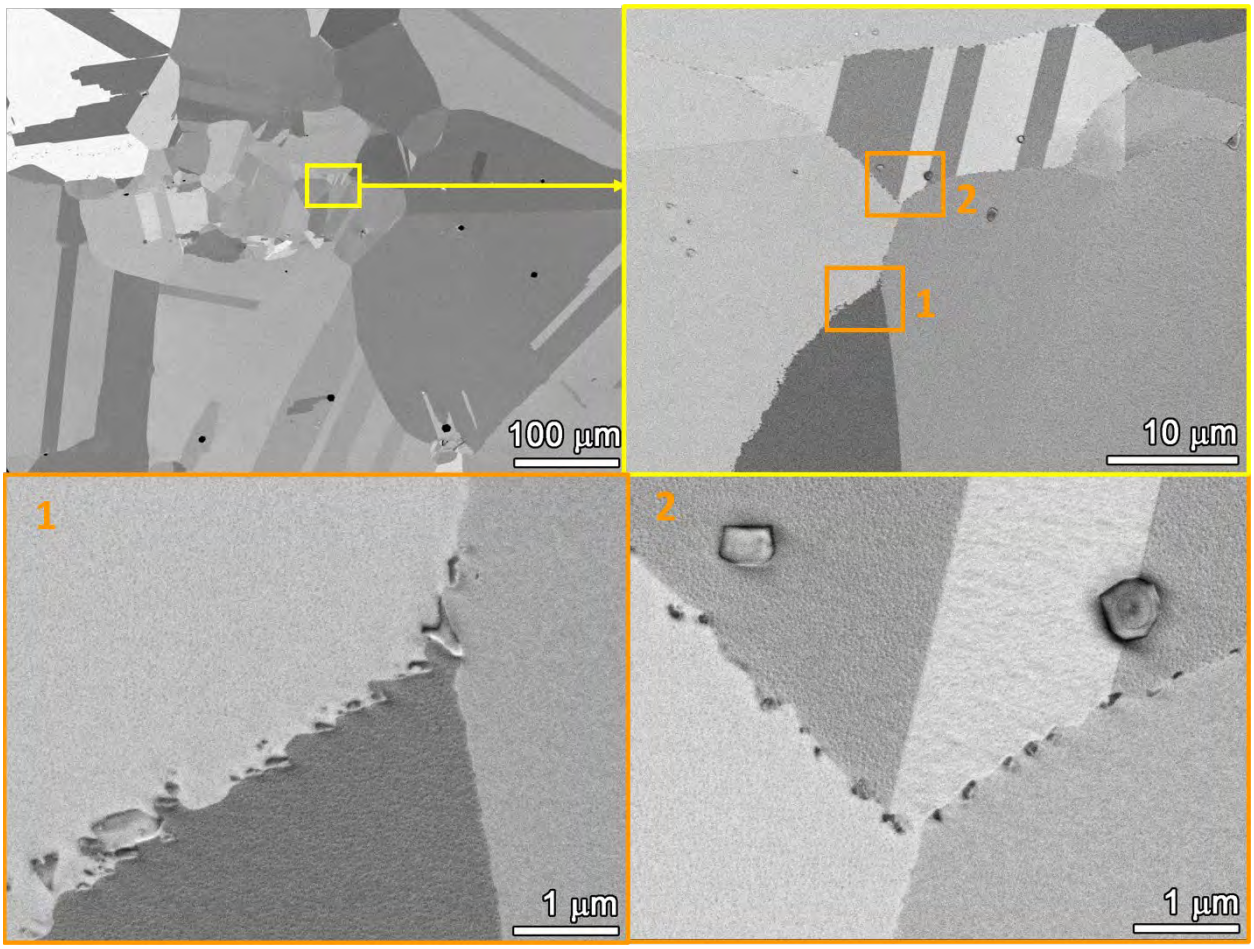

Figure 12. SEM-BSE images showing the grain microstructure and precipitation distribution in the fine grain banding in the "A" observation direction of the Alloy X-750 block received from INL (heat 2750-5-7656).

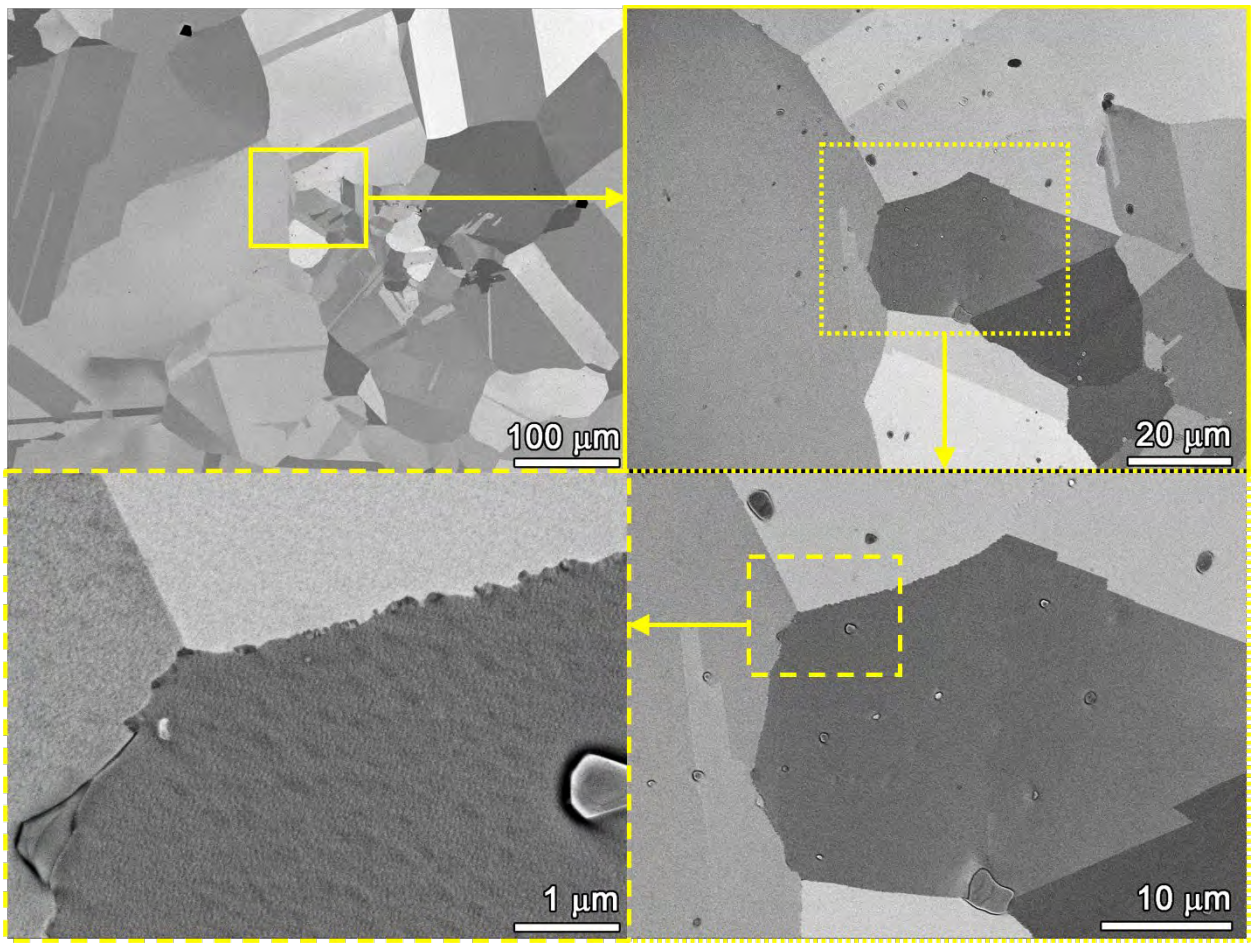

Figure 13. SEM-BSE images showing the grain microstructure and precipitation distribution in the fine grain banding region in the "B" observation direction of the Alloy X-750 block received from INL (heat 2750-5-7656).

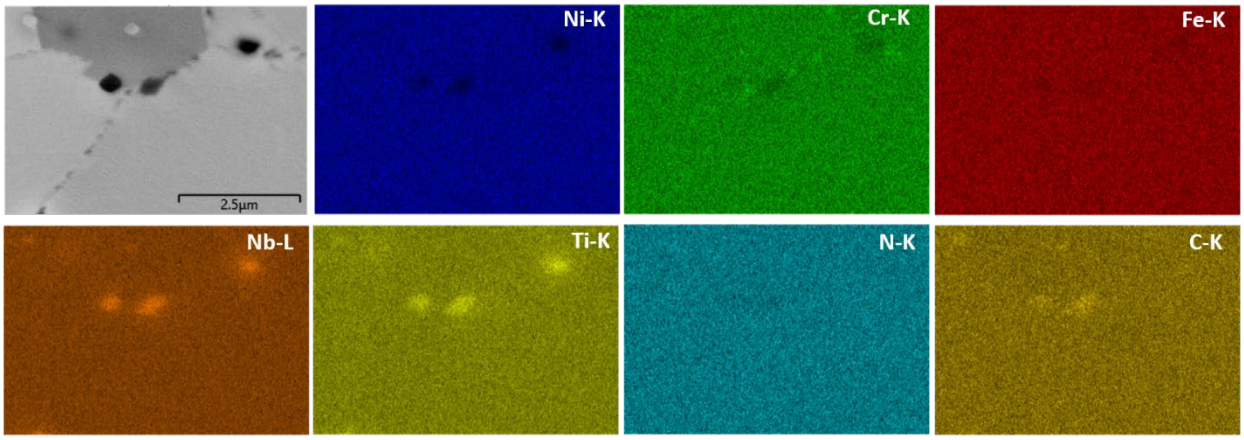

Figure 14. Qualitative SEM-EDS analysis of the chemical composition of the grain boundary precipitates observed in the "A" observation direction of the Alloy X-750 block received from INL (heat 2750-5-7656).

3.2 Alloy 718

3.2.1 General Information

Alloy 718 is an age-hardenable nickel-base alloy containing 17-21% Cr and a higher niobium (Nb) content than Alloy X-750. It can be heat treated to very high strength due to precipitation of a fine distribution of nanometer size γ', Ni_3(Al,Ti), and γ", Ni_3(Nb). Alloy 718 has found increasing use in LWRs for springs and bolts in fuel elements because of its significant strength and resistance to corrosion and thermal/irradiation-induced relaxation. Service experience has generally been good, but recently there have been instances of cracking and deleterious effects, leading to early assembly discharge and, possibly, fuel failures [10]. Early LWR applications of Alloy 718 usually adapted heat treatments intended for aircraft engine and gas turbine applications. While these heat treatments produce grain boundary precipitates that were very beneficial for minimizing high-temperature creep, the precipitates themselves are not necessarily beneficial for SCC resistance in LWR environments. This is often correlated with the presence of the δ phase, Ni_3Nb. δ phase is a thermodynamically more stable form than the γ" strengthening phase. Its formation results in γ" denuded zones on either side of grain boundaries that may, in principle, allow localized strain concentration [11, 12]. However, others have not observed a major effect of δ phase on product performance, and instead note that it is a necessary feature to avoid excessive grain growth during solution annealing prior to thermal aging [13]. Subsequent commercial heat treatments developed for Alloy 718 resulted in high SCC initiation resistance, particularly in PWR environments. However, test results from these commercial heats show that crack propagation rates could be quite high depending upon the type of heat treatment [10].

For this study, PNNL purchased an L14" × W4" × T2" block from an Inconel Alloy 718 plate heat HT6097EK11 manufactured by Special Metals. It has typical Alloy 718 composition in conformance with Alloy 718 specifications as listed in Table 4. The material was solution annealed and certified by Special Metals to Society of Automotive Engineers (SAE) Aerospace Material Specifications (AMS) 5596 [14]. A conventional two-step precipitation hardening heat treatment (age at 718 °C for 8 hours, cool to 621 °C at 55 °C/h, age for 8 hours, and air cool to room temperature) compliant with SAE AMS5663 [15] was applied to the block at PNNL. This heat treatment was selected because it is known to enhance the SCC susceptibility of Alloy 718. This would help us complete the SCC testing within a reasonable test duration that otherwise could last too long for the program.

Table 4. Chemical composition (wt. %) of Alloy 718 Heat HT6097EK11 in comparison to the Alloy 718 specifications.

Element	A718 Spec	Alloy 718 Heat HT6097EK11
C	<0.08	0.03
Cr	17-21	18.68
Fe	Bal.	17.69
Mn	<0.35	0.09
Ni	50-55	53.53
Mo	2.8-3.3	2.88
Ti	0.65-1.15	0.92
Al	0.2-0.8	0.57
Co	<1	0.22
P	<0.015	0.01
Cu	<0.3	0.12
S	<0.015	0.001
Si	<0.25	0.08
Nb+Ta	4.75-5.5	5.04 (Nb: 5.03, Ta: 0.004)
B	/	0.002
Bi	/	0.000019
Pb	/	0.00008

3.2.2 Characterizations of the Alloy 718 Material

After the precipitation hardening treatment, hardness measurements and material characterizations were performed on the "A", "B", and "C" observation directions to evaluate the mechanical properties and microstructures. The samples were polished to a colloidal silica finish that removed all the hardened damage layer produced during machining. The hardness measurements were carried out on a CM-700AT Clark Microhardness Tester equipped with a FutureTech FM-ARS9000 fully automated hardness testing system. A 3×3 array of indents was acquired on each sample using a load of 300 g, an indent spacing of 0.225 mm (maintains >3d spacing between the indents), and a dwell time of 12 s. These parameters were chosen following our standard procedure for measuring the hardness of Ni-base alloys [16]. As summarized in Table 5, the results suggest that the precipitation-hardened Alloy 718 material exhibits a similar average hardness between ~430–445 HV in all planes, which meets the post-heat treatment hardness criteria (>342 HV) specified in SAE AMS5663.

Table 5. Vickers hardness measured on the "A", "B", and "C" observation planes of the precipitation-hardened Alloy 718 (heat number HT6097EK11).

	"A" plane	**"B" plane**	**"C" plane**
Hardness (HV)	427.20±3.69	445.57±10.67	433.05±14.79

The samples were then etched using the same etching procedure used for the Alloy X-750 optical examinations. The results are shown for each observation direction in Figures 15-17. Anisotropic shape grains with a long axis aligned to the longitudinal direction were found when viewing the microstructure from the "A" direction, where the L-plane normal corresponds to the plate processing direction (Figure

15). While some variation exists in grain size between <100 to ~200 μm, no obvious banding was observed in this material. SEM examinations and EDS analysis were also performed on non-etched samples to evaluate precipitate types and their distribution. Figures 18 and 19 show that stringers of intragranular coarse (Nb, Ti)C carbides and TiN carbonitrides were occasionally found along the processing direction in the "A" observation direction. In some cases, NbC-type carbides are seen to nucleate on the TiN carbonitrides (Figure 20, middle image). Figures 18 and 20 also revealed a semi-continuous distribution of sub-micrometer to a few micrometer-sized, thin platelet-like secondary phase precipitates on most of the high-energy grain boundaries and some prior grain boundaries. Their bright contrast in the SEM-BSE images and enrichment in Nb are consistent with the δ phase, a common feature in precipitation-hardened Alloy 718 [12]. In addition, much finer, 10s–100s of nanometer-sized $Cr_{23}C_6$ type precipitates were frequently dispersed along the high-energy grain boundaries adjacent to the δ phases. An example is provided in Figure 21, where high content of Cr was observed at several locations coincident with the darker-contrasted precipitates in the corresponding SEM BSE image.

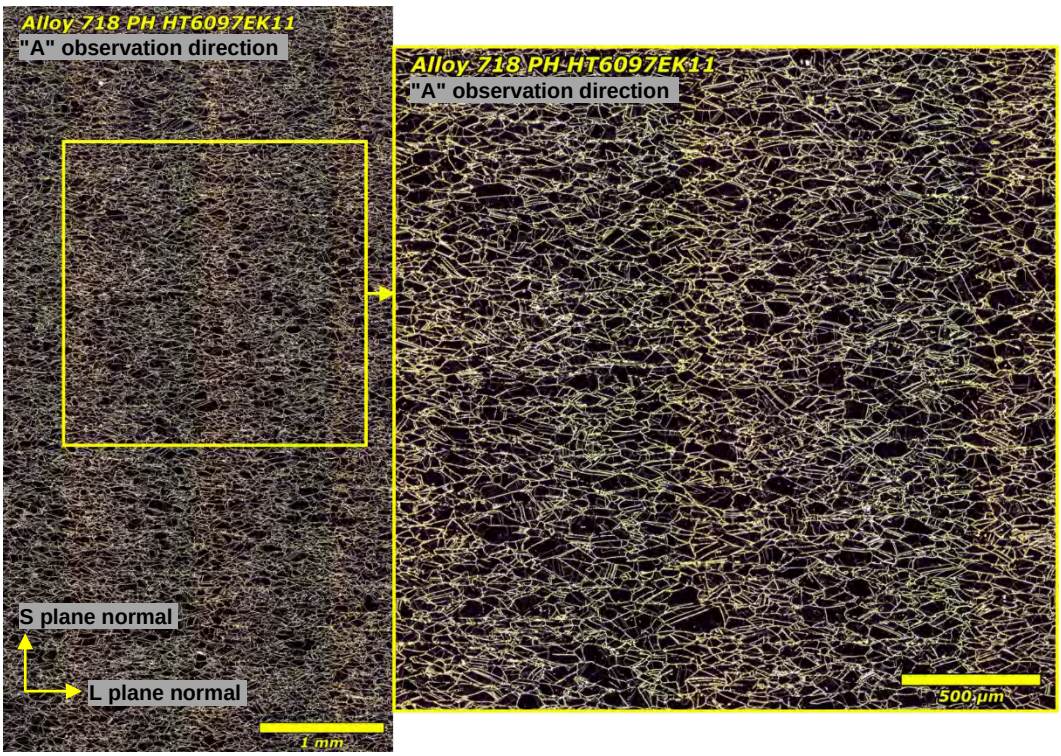

Figure 15. Representative optical micrograph of the microstructure revealed in the "A" observation direction of the precipitation-hardened (PH) Alloy 718 material.

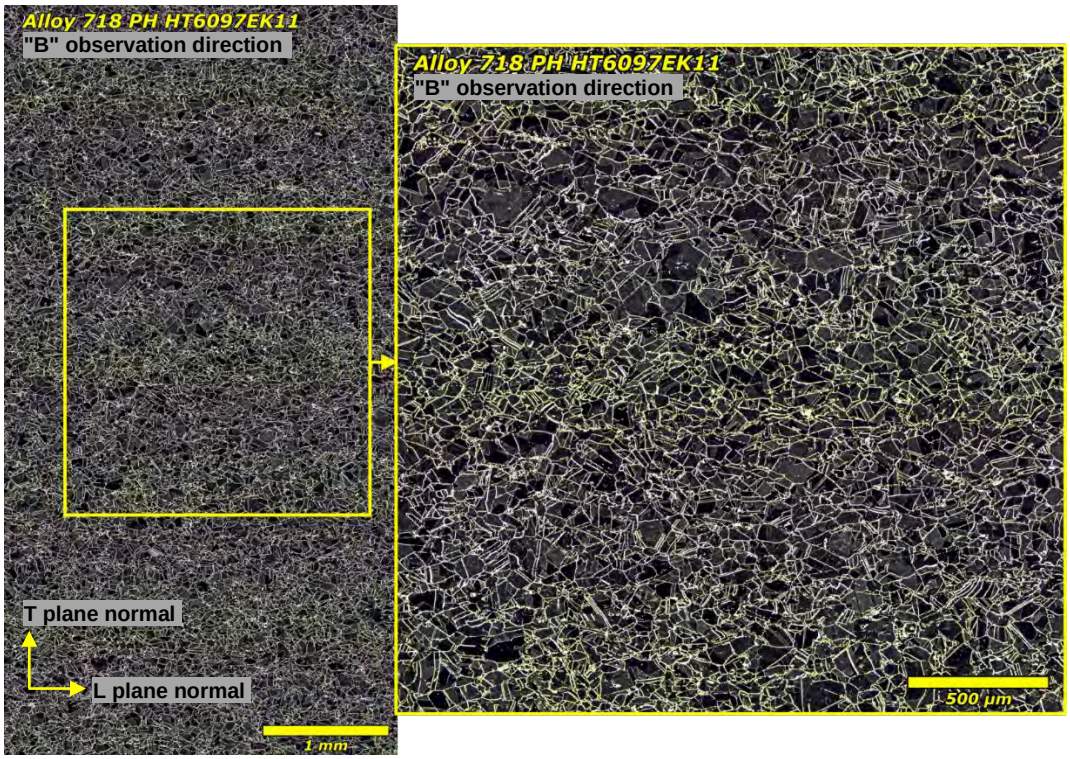

Figure 16. Representative optical micrograph of the microstructure revealed in the "B" observation direction of the precipitation-hardened Alloy 718 material.

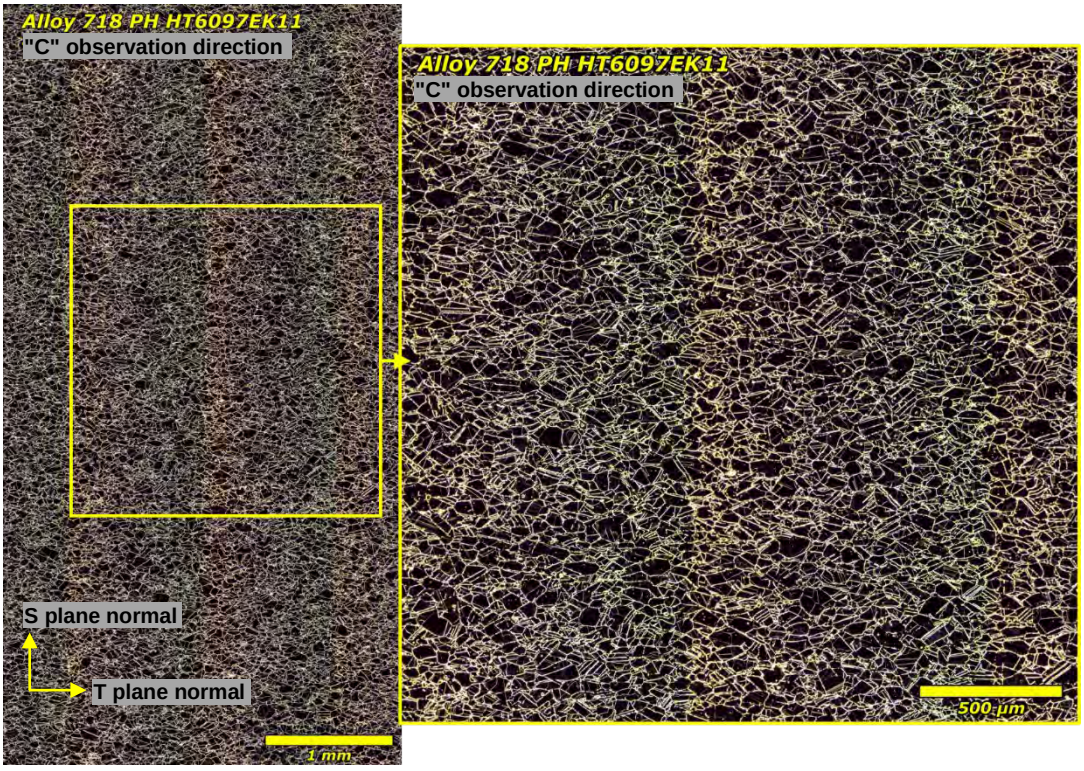

Figure 17. Representative optical micrograph of the microstructure revealed in the "C" observation direction of the precipitation-hardened Alloy 718 material.

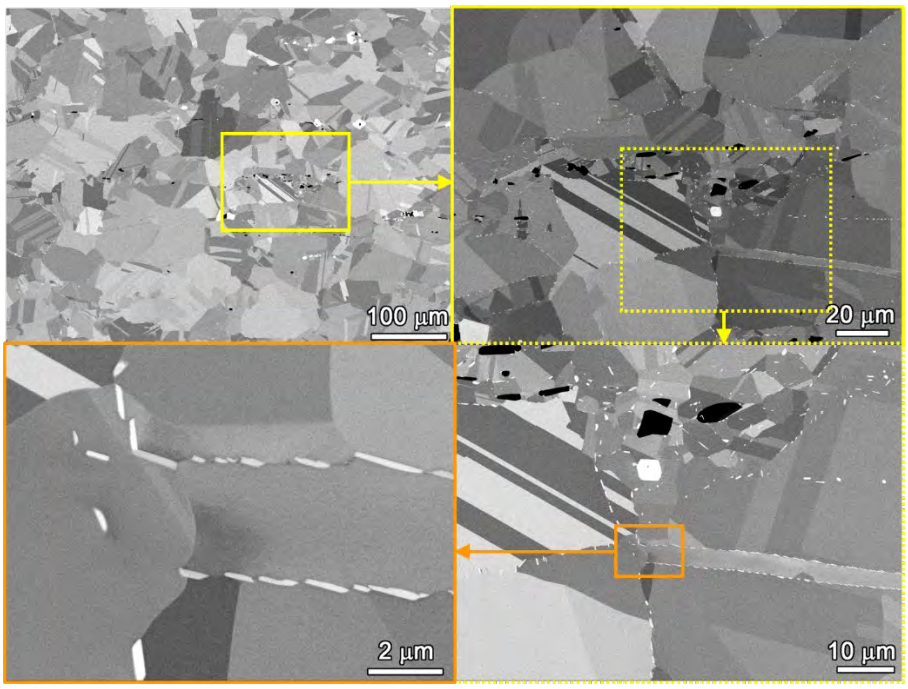

Figure 18. SEM-BSE images of larger precipitates on grain boundaries in the "A" observation direction of the precipitation-hardened Alloy 718 material.

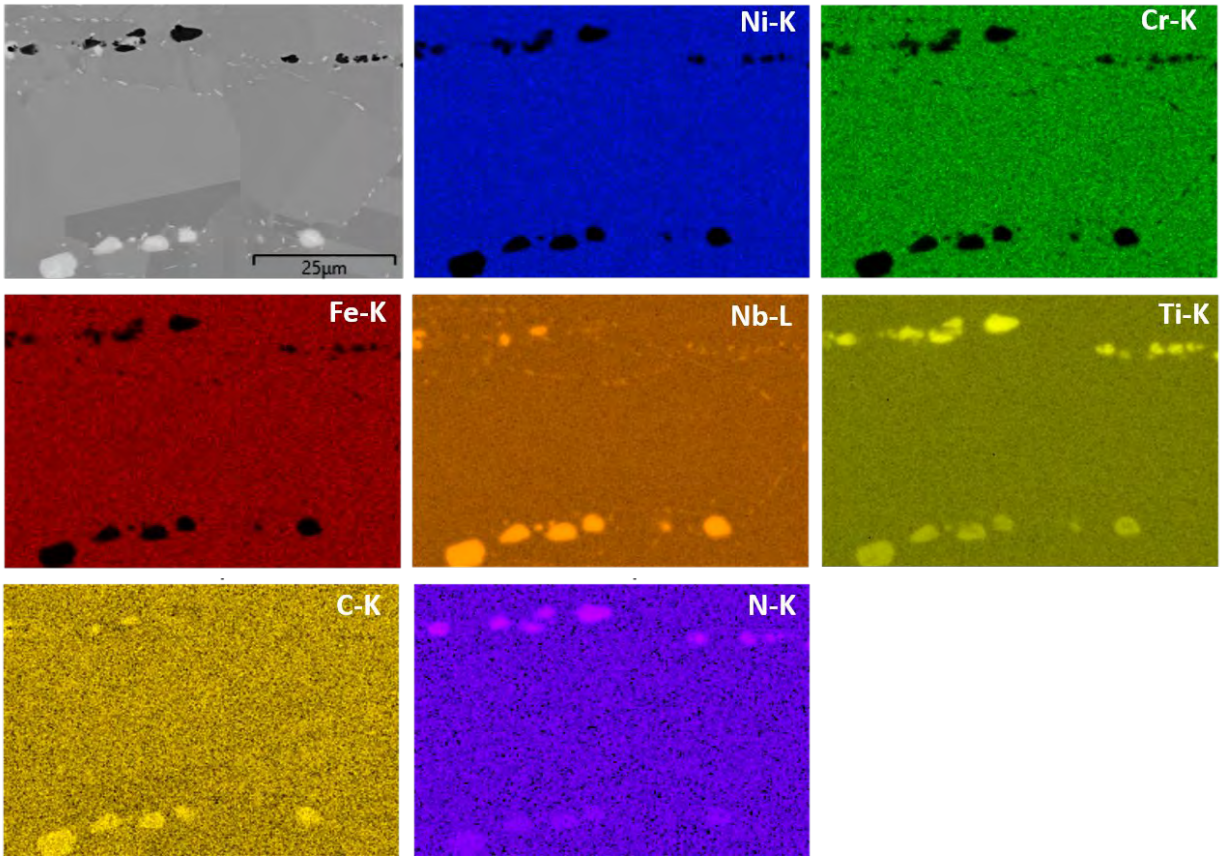

Figure 19. Qualitative SEM-EDS analysis of the chemical composition of the precipitates observed in the "A" observation direction of the precipitation-hardened Alloy 718 material.

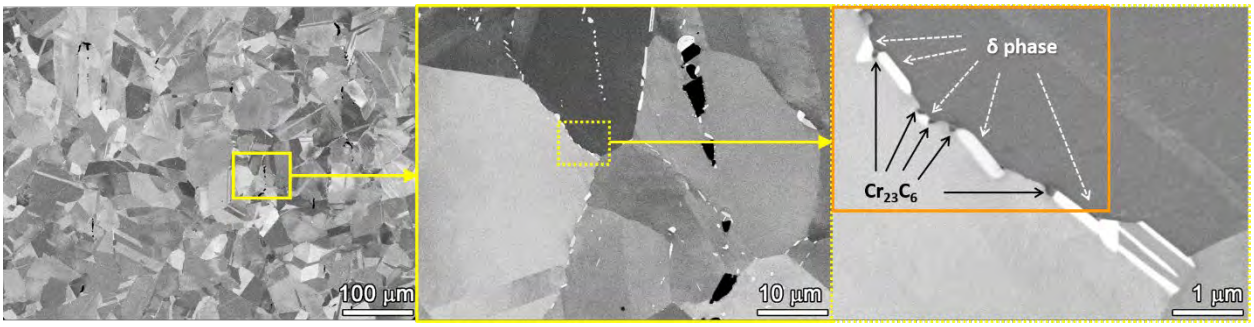

Figure 20. SEM-BSE images of larger precipitates on grain boundaries in the "B" observation direction of the precipitation-hardened Alloy 718 material.

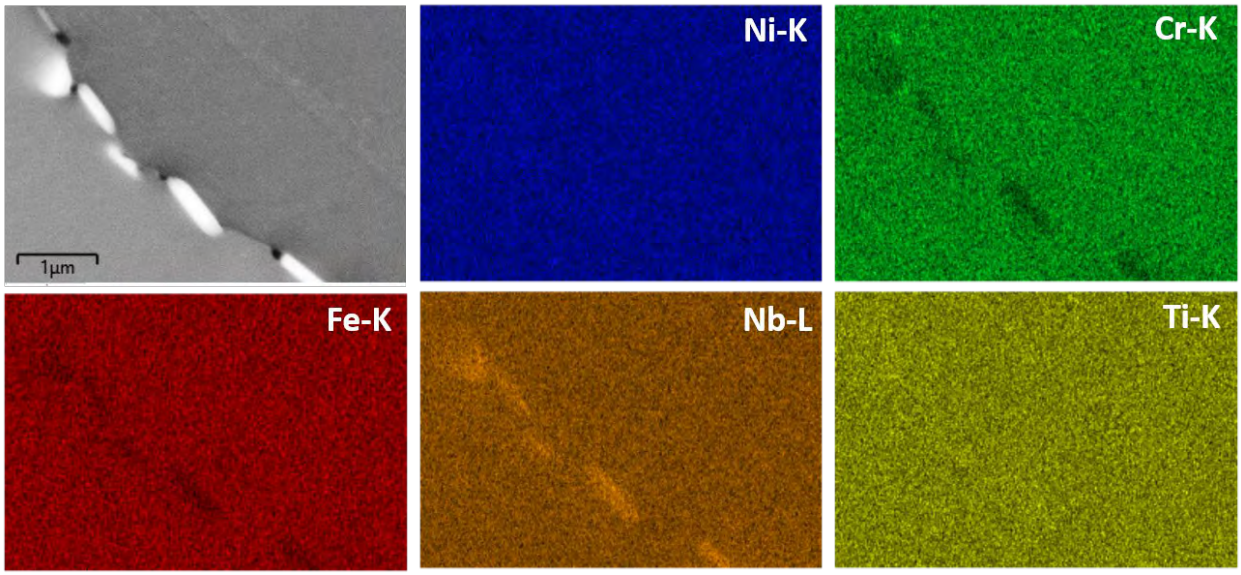

Figure 21. Qualitative SEM-EDS analysis of the chemical composition of the region highlighted in the orange box in the far-right image of Figure 20.

3.3 Alloy 82H

Alloy 82H is a compatible weld metal for Alloy 600 for automatic gas tungsten arc and submerged arc welding. The Alloy 82H weld (Heat 21719-2) used in this study is an in-house multi-pass build-up by Naval Nuclear Laboratory. The composition of this weld compared to the Alloy 82H specification is given in Table 6. As shown in Figure 22, the weld block was received in an "L" shape. It had received a post weld heat treatment (PWHT) at ~621 °C for 8.5 hours with a heat up rate of ~16.8 °C/hour from room temperature to 621 °C and a cooling rate of ~31 °C/hour from 621 to 310 °C, followed by air cool.

Table 6. Chemical composition (wt. %) of Alloy 82H Heat 21719-2 in comparison to the Alloy 82H specifications.

Element	A82 Spec	Alloy 82H Heat 21719-2
C	≤0.1	0.04
Cr	18–22	20.1
Fe	≤3	0.7
Mn	2.5–3.5	2.75
Ni	Bal.	72.8
Ti	≤0.75	0.47
Co	≤0.1	0.04
P	≤0.03	0.01
Cu	≤0.5	0.07
S	≤0.015	0.002
Si	≤0.5	0.07
Nb+Ta	2.0–3.0	2.5 (Ta: 0.069)
Pb		0.002

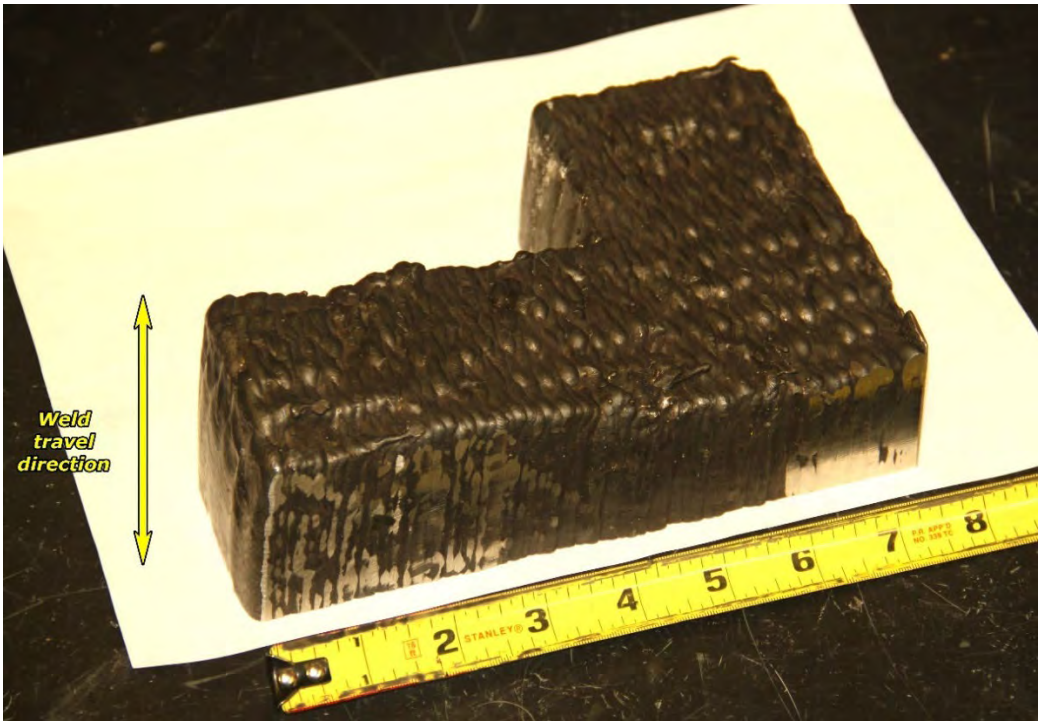

Figure 22. The as-received Alloy 82H (Heat 21719-2) block for this study.

4. SCC CRACK GROWTH BEHAVIOR OF Alloy X-750 IN KOH VS. LIOH-CONTAINING PWR PRIMARY WATER

4.1 SCC Growth Rate Test

Two Alloy X-750 specimens, CT223 and CT224, were machined in the T-L orientation from the block we received from INL. They were fatigue precracked individually in air at room temperature following the procedure described in Section 2.1.2. The side grooves of these two specimens were polished to a 1 μm finish, allowing the precrack morphology to be viewed and its length to be measured. In Figures 23 and 24, optical micrographs show the precrack produced by air fatigue in CT223 and CT224, respectively. While the target precrack length was set at 1.1 mm, the precrack in CT223 exhibited a certain degree of unevenness with a length of 0.605 mm on Side A and 1.506 mm on side B. In comparison, the precrack in CT224 has a more consistent length on both sides (1.185 vs. 1.225 mm). Therefore, it was decided to use CT224 as the controlling sample and CT223 as the companion sample in the SCC growth rate test, meaning that the load control during the test is implemented based on the response of CT224. This helps to guard against the possibility of inaccurate DCPD crack length data causing stress intensity to deviate substantially from the target value.

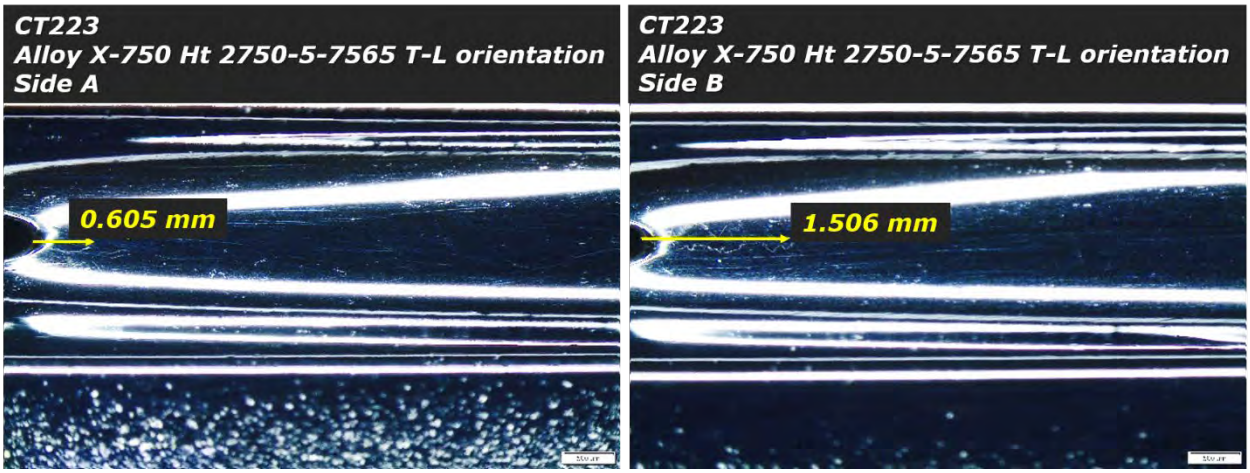

Figure 23. Optical micrographs of the polished side grooves of the Alloy X-750 specimen CT223. The length of the precrack produced by air fatigue is marked in both side grooves.

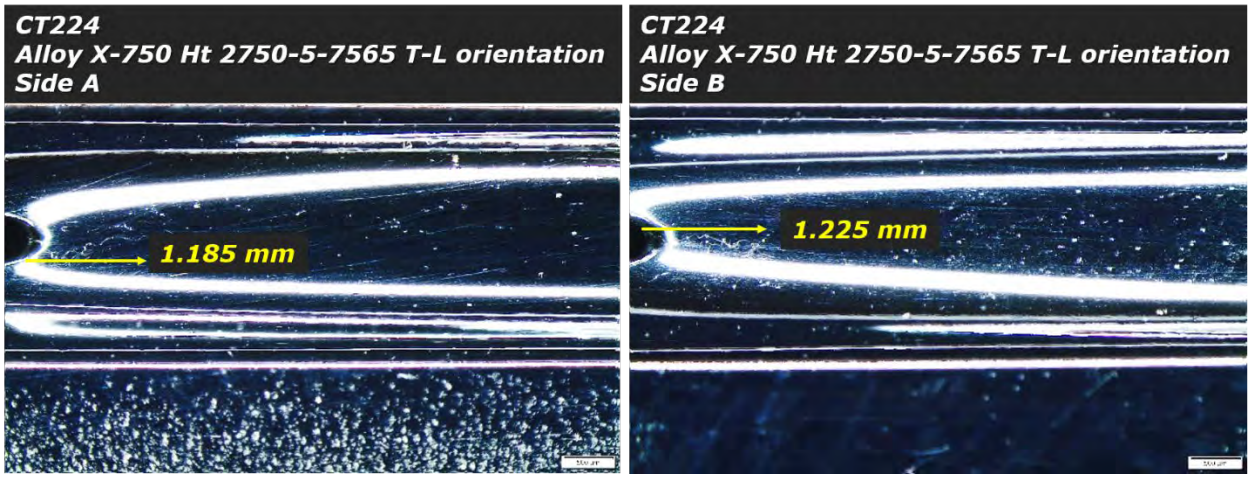

Figure 24. Optical micrographs of the polished side grooves of the Alloy X-750 specimen CT224. The length of the precrack produced by air fatigue is marked in both side grooves.

A test overview of the non-referenced DCPD crack growth response of CT223 and CT224 is provided in Figure 25. The non-referenced DCPD response is used here because the resistivity evolution monitored by referenced DCPD is very close to zero, and the crack length noise level is reduced when using the non-referenced DCPD crack length. Currently, the test has been completed with the SCCGR of both specimens evaluated in all three water chemistries specified in Table 1 through on-the-fly changes. In particular, the SCCGR response in the BOC chemistry has been evaluated twice at 325 °C with different dissolved hydrogen (DH) levels, which will be explained later.

The two specimens were loaded in series into an NRC SCC test system, and the test was started in the baseline PWR primary water condition containing 1500 ppm B and 2.2 ppm Li at 360 °C and 25 cc/kg H_2. Figure 26 presents the initial aggressive cycling in high-temperature water to further extend the precrack produced by air fatigue. A series of loading conditions were used to transition from the TG precrack to an IGSCC crack front that is typically much more susceptible to SCC growth in Ni-base alloys. Loading conditions started with cyclic loading with decreasing frequency from 1.0 to 0.01 Hz at a load ratio of 0.5, followed by a final cycling step of a 980 s rise and a 20 s fall (0.001 Hz) with R = 0.5 in a sawtooth form. The two specimens exhibited consistent crack growth behavior during these loading steps, and the CGR continued to drop as the cyclic loading conditions became more and more gentle. However, after a hold time of 2.5 h was added at K_{max} (20 MPa√m in this case) to the 980s/20s cycling, the CGR unexpectedly increased by ~2X in both specimens (compare the 980s/20s corrosion fatigue CGRs in Figure 27 to the 980s/20s+2.5 hr hold corrosion fatigue CGRs in Figure 27). This has never been seen in the testing of Alloy 600/690 and their weld metals at PNNL, but it has been observed by at least one other lab that has tested Alloy X-750 SCC growth behavior [10] and might be a unique trait of this precipitation-hardened high strength Ni-base alloy. The CGRs of the two specimens only dropped by a small fraction after constant K of 20 MPa√m was implemented, indicating a high susceptibility to SCC growth of this material in the baseline environmental condition. The observed constant K SCCGR values of ~5×10^{-7} mm/s at 360°C were considered too high for this test because the rapid crack growth would result in substantial crack extension before water chemistry changes could stabilize, leading to an excessive crack extension that would cause the specimens to run out of usable crack extension before all planned assessments are completed. As a result, it was decided to drop the test temperature from 360°C to 325°C and increase the dissolved hydrogen content from 26 to 29 cc/kg. These changes would decrease the kinetics of SCC and bring the DH level from the Ni/NiO stability line at 360°C to the Ni-stable regime at 325°C, further reducing the SCC susceptibility of the material. As shown in Figure 27, the SCCGR of CT223 and CT224 dropped instantly from ~5×10^{-7} mm/s to ~$8–9\times10^{-8}$ mm/s after these changes were made. The new SCCGRs values were more manageable for the test, so it was decided to

perform subsequent SCCGR assessments in this condition. This condition is closer to the actual environmental condition in the plant and has been widely used as a prototypic simulated PWR primary water environment for SCC testing of susceptible materials.

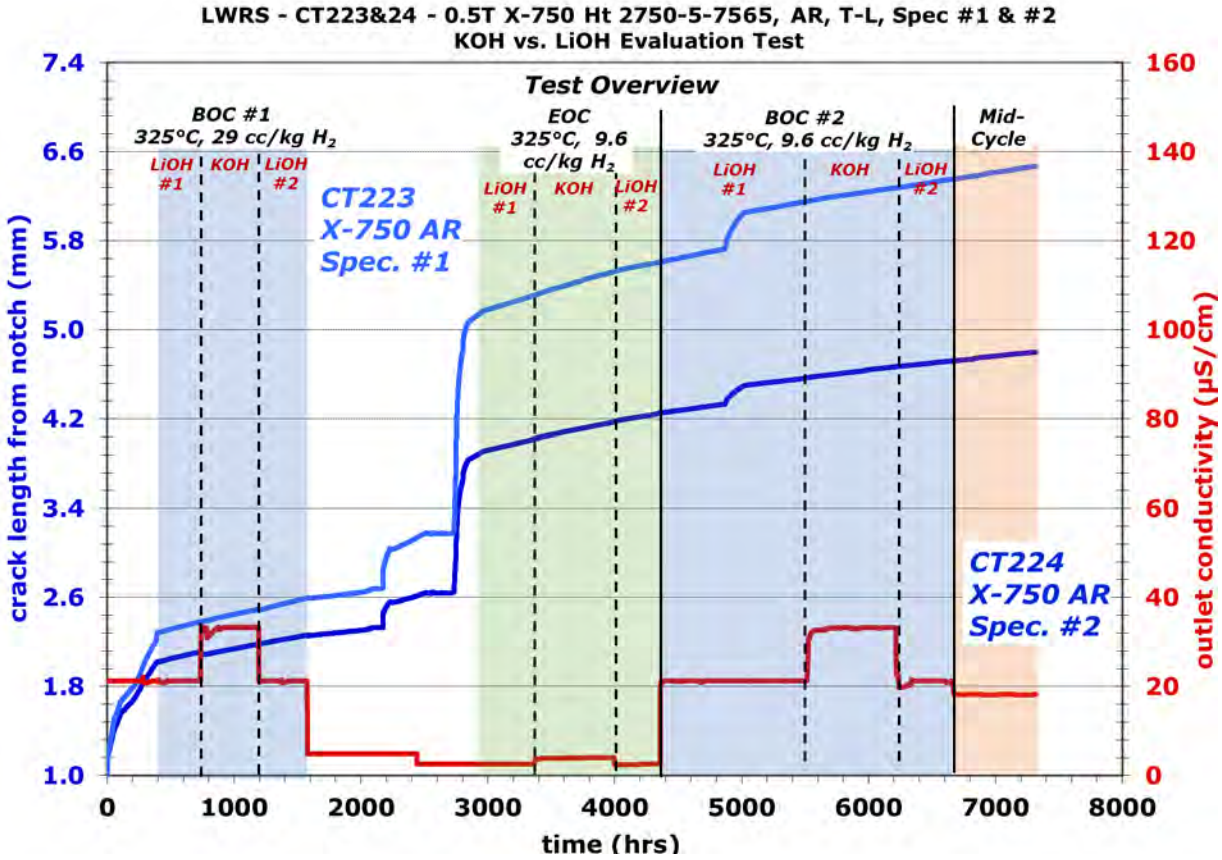

Figure 25. Test overview of crack growth response in the two Alloy X-750 specimens CT223 & 224 tested in T-L orientation. The effect of KOH vs. LiOH on the SCCGR of both specimens was evaluated in 325°C simulated PWR primary water at a constant load of 20 MPa√m.

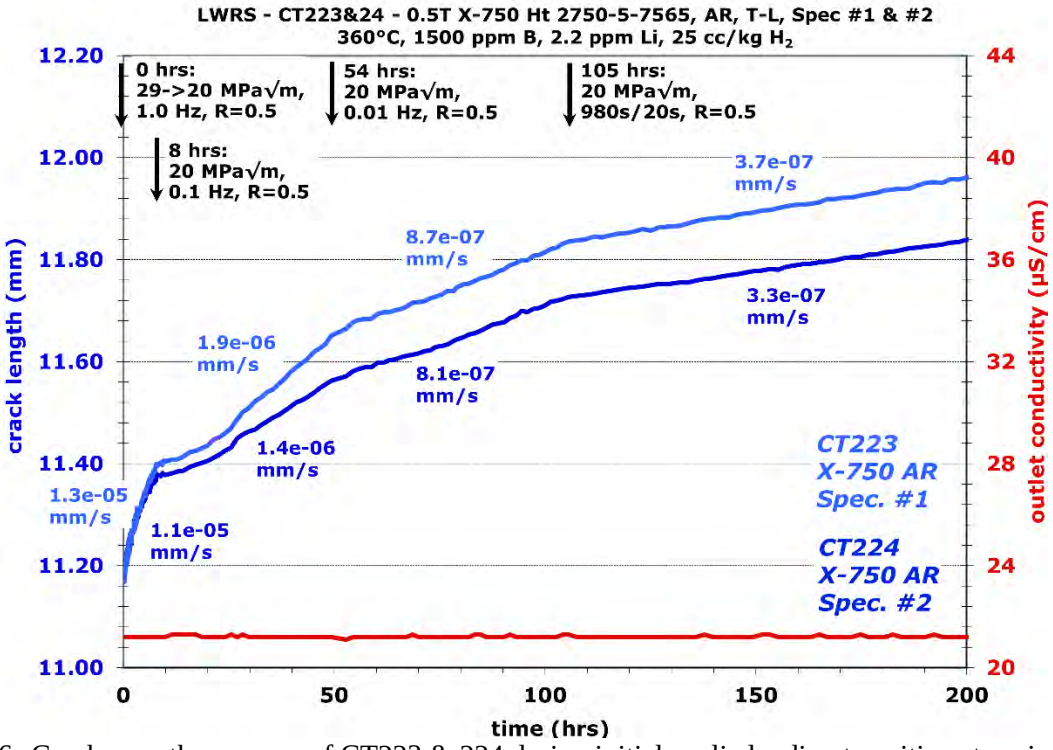

Figure 26. Crack growth response of CT223 & 224 during initial cyclic loading transition steps in 360°C simulated PWR primary water.

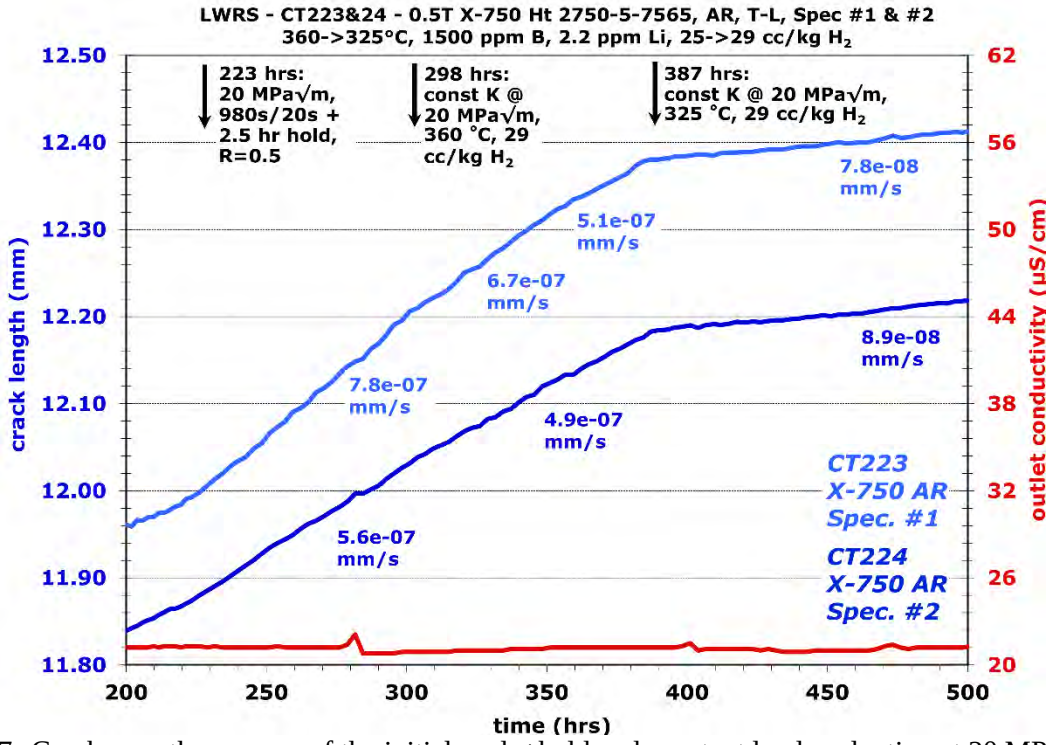

Figure 27. Crack growth response of the initial cycle+hold and constant load evaluation at 20 MPa√m of CT223 & 224 in 360°C simulated PWR primary water with 25 cc/kg H_2. The water chemistry was then changed to 325°C and 29 cc/kg H_2 due to high SCCGR observed at 360°C and 25 cc/kg H_2.

The SCCGR evaluation of the effect of KOH vs. LiOH began with the BOC water chemistry at 325°C, 29 cc/kg H_2, and a constant load of 20 MPa√m. An overview of the SCCGR response of CT223 and 224 during the BOC evaluation period is provided in Figure 28. The ideal increment of crack length over which to measure a steady SCCGR is several grain diameters. However, since the Alloy X-750 material exhibits a bi-modal grain size distribution, determining an optimal crack extension to be evaluated for steady crack growth response is not straightforward. Figure 10 suggests that while the larger grains in the T-L plane are often >200 μm in size, a high density of clusters of much smaller grains are dispersed in the microstructure. Since the crack front in the CT specimens spans a total length of ~12 mm, multiple fine-grained clusters should be encountered at any given time as the crack grows. Therefore, we chose 100 μm as the preferred crack extension to observe SCCGR during each water chemistry evaluation. As shown in Figure 28, the evaluation started with 1500 ppm B/2.2 ppm Li, moved on to 1500 ppm B/12.4 ppm K after the crack extension reached ~100 μm in both specimens, and then back to 1500 ppm B/2.2 ppm Li to confirm behavior. All the water chemistry changes were performed on-the-fly following the procedure described in Section 2.1.4. The two specimens exhibited very consistent crack growth behavior throughout this evaluation, with a maximum change of ~17% in SCCGR between adjacent test steps, which is well within the uncertainty of the measurement method (Section 2.1.3). Therefore, it can be concluded that KOH BOC water chemistry does not affect the SCC growth behavior of Alloy X-750.

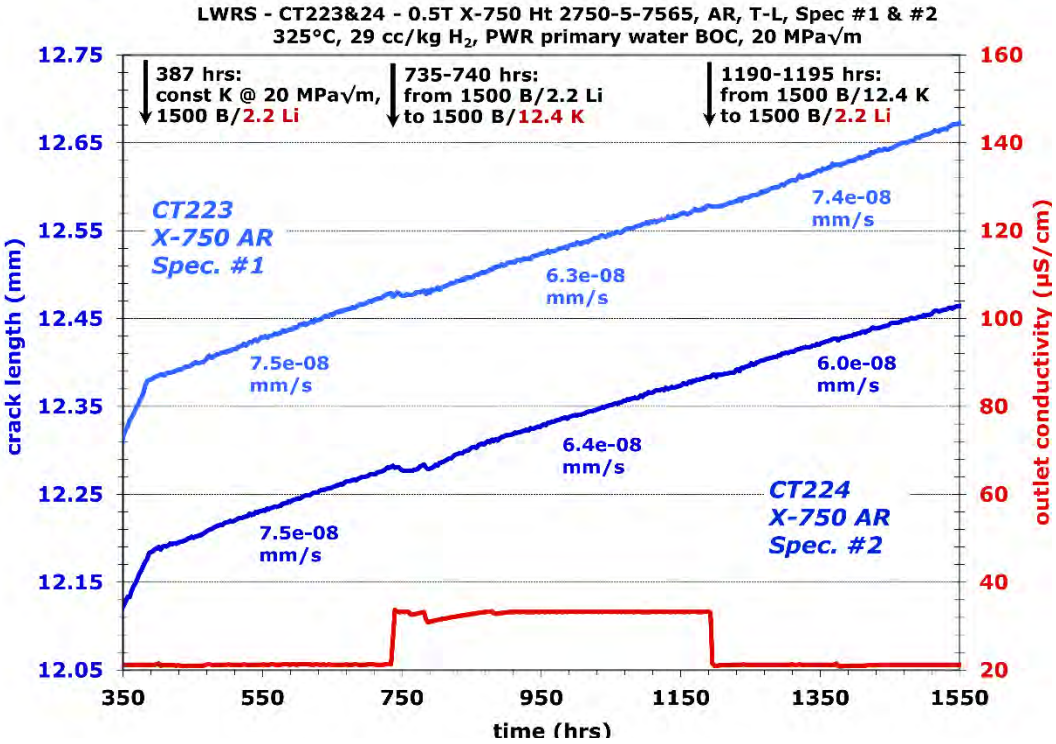

Figure 28. SCCGR response of CT223 & 224 in 325°C PWR primary water BOC chemistry with on-the-fly changes between LiOH and KOH. The concentrations of B, Li, and K in the plot are shown in ppm.

Once the SCCGR evaluation in the BOC water chemistry was completed, the test moved on to assess the effect of KOH vs. LiOH in the EOC water chemistry. An on-the-fly change from 1500 ppm B/2.2 ppm Li to 10 ppm B/0.23 ppm Li was implemented while all the other testing conditions were maintained the same. An obvious drop in SCCGR was observed in both specimens right after the change was made

(Figure 29). The variation in SCCGR between the 10 ppm B/0.23 ppm Li EOC chemistry and the 1500 ppm B/2.2 ppm Li BOC chemistry in both specimens reached ~55–58%, suggesting a real decrease in SCCGR beyond the uncertainty of the measurement method. This was unexpected because most studies suggest no change in SCCGR in Ni-base alloys between low and high B/Li concentrations [17, 18]. A recent KOH vs. LiOH study on cold-worked Alloy 600 also showed no change in SCCGR on shifting from the 1500 ppm B BOC chemistry to the 10 ppm B EOC chemistry [3]. Therefore, it was decided to have CT223 and 224 exposed for a longer duration in this water chemistry condition while closely monitoring their SCCGR response. For the next ~500 hours, both specimens exhibit a similar and steady SCCGR at ~2.5–3.3×10^{-8} mm/s that remains clearly lower than the SCCGR observed in the 1500 ppm B/2.2 ppm Li BOC chemistry. In an attempt to promote crack growth, a series of cyclic loading steps were implemented at 2,172 hours to extend the crack for ~200 µm in the controlling specimen CT224 before transitioning back to constant load evaluation at 2,509 hours. Surprisingly, both specimens exhibited a decreasing trend in their DCPD response (Figure 30). Since the test was running in the Ni-metal stable condition, the most likely cause for this observation is that Ni-metal conducting bridges had formed across the crack walls. These Ni-metal conducting bridges can lead to phantom DCPD crack length reduction over a multi-day period, hiding actual crack growth. To verify this hypothesis, the DH was changed from 26 to 9.6 cc/kg at 2,706 hours, which corresponds to the electrochemical potential of the Ni/NiO stability line in 325 °C PWR primary water that maximizes the SCC susceptibility of Ni-base alloys. As shown in Figure 30, an immediate increase was observed in CGR in both specimens right after this change was made, confirming that Ni-metal bridges had indeed formed along the crack wall. As a result, we again applied a series of cyclic loading steps to further mitigate the Ni-metal bridging issue by exposing fresh metal surface for crack growth via cycling (Figure 31). Typical, decreasing CGR was observed for both specimens with more and more gentle cycling conditions, and the constant load was implemented at 2,964 hours for assessments of LiOH vs. KOH on the crack growth behavior of the two specimens in EOC water chemistry.

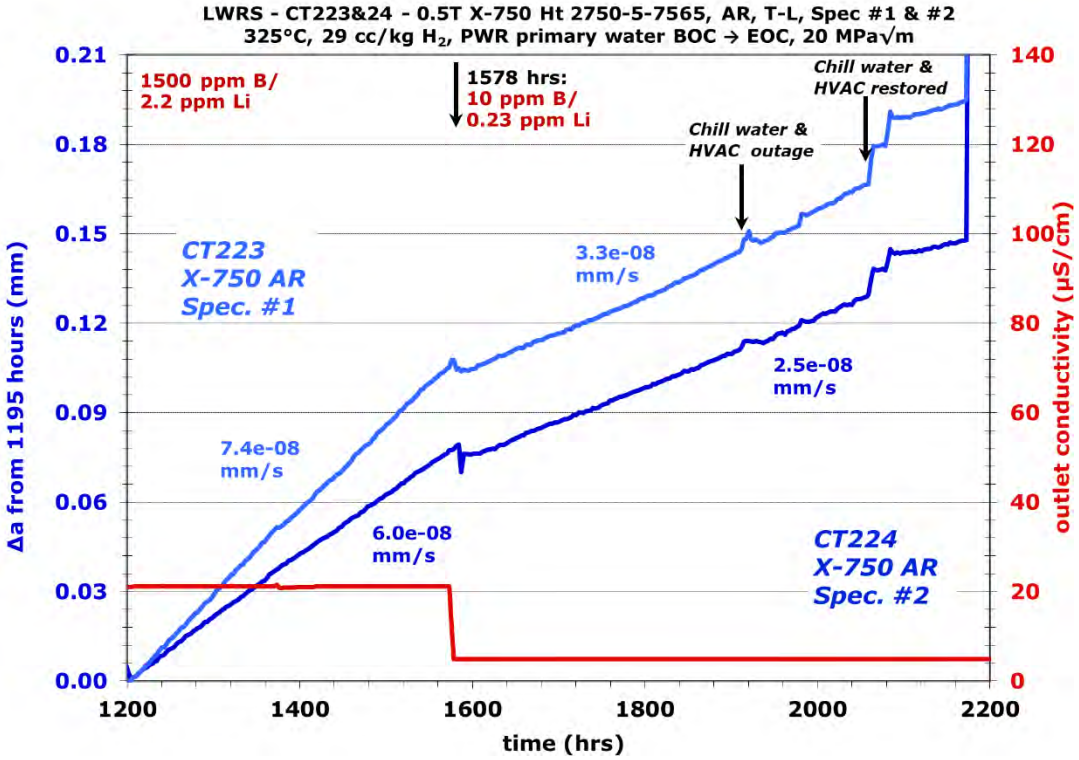

Figure 29. SCCGR response of CT223 & 224 in 325°C PWR primary water with on-the-fly change from LiOH BOC to LiOH EOC water chemistry.

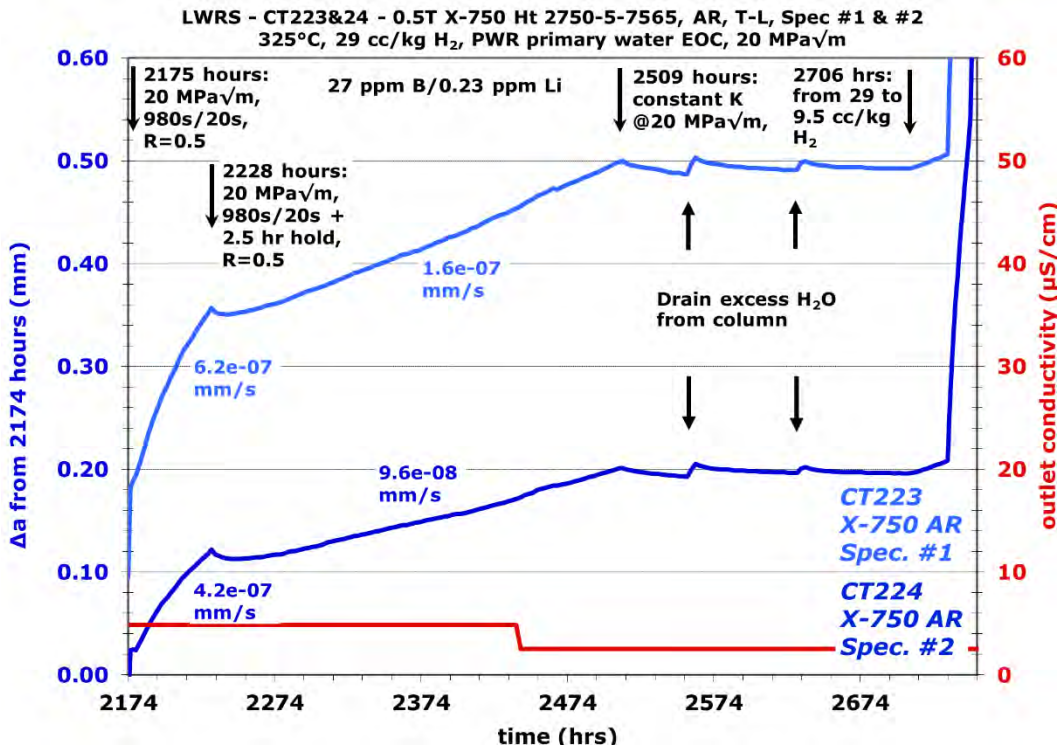

Figure 30. CGR response of CT223 & 224 during the first attempt to adjust crack growth behavior after the water chemistry change from LiOH BOC to LiOH EOC.

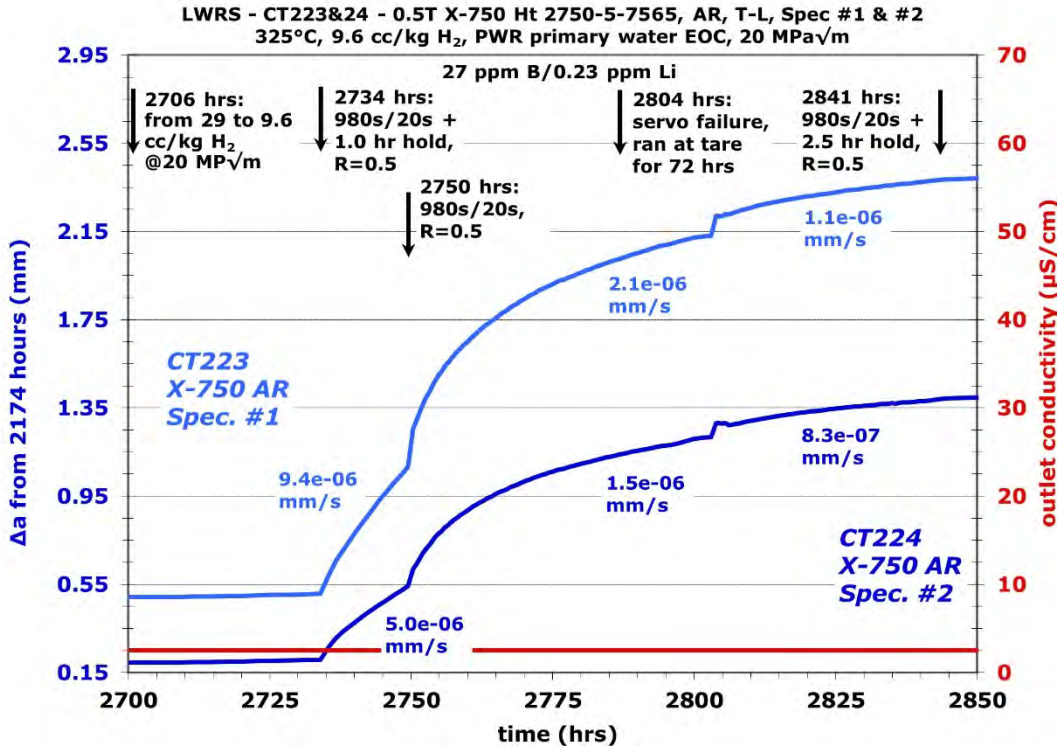

Figure 31. CGR response of CT223 & 224 in transition steps after the dissolved hydrogen in the water changed from 29 to 9.6 cc/kg.

Figure 32 provides an overview of the SCCGR of CT223 and CT224 during the entire evaluation in EOC chemistry with on-the-fly changes from LiOH to KOH and back to LiOH to confirm behavior. The SCCGR in each specific water chemistry condition was evaluated for at least 100 µm in crack extension. While the SCCGR in both specimens gradually decreased over the entire EOC water chemistry evaluation, the maximum change in SCCGR between adjacent test steps was ~14%, which is again well within the uncertainty of the measurement method (Section 2.1.3).

Since an adjustment was made in DH to move the specimens from Ni-metal stable regime to the Ni/NiO stability line, it was decided to re-evaluate the SCCGR response of CT223 and CT224 in BOC water chemistry at this new DH level. As shown in Figure 32, the water chemistry was changed on-the-fly from EOC-LiOH chemistry to BOC-LiOH chemistry while maintaining a constant load at 20 MPa√m. A very smooth transition was observed in both specimens with no obvious change in SCCGR before and after this change. Since the SCCGRs observed in the BOC chemistry were higher than that in the EOC chemistry when the specimens were in the Ni-metal stable regime (Figure 29), a cycle+hold step was performed to see if similar phenomenon would be reproduced at the Ni/NiO stability line after the cyclic loading step (Figure 33). Interestingly, no increase in SCCGR occurred in the BOC chemistry in either specimen this time. The test continued to evaluate the SCCGR response of both specimens with on-the-fly changes from LiOH to KOH and back to LiOH in the BOC water chemistry. As summarized in Figure 34, very consistent crack growth behavior was observed for both specimens with little change in CT224 and only up to ~12% variation in CT223 during the entire evaluation period. The test subsequently moved on to the final step to evaluate the SCC growth response of the two specimens in mid-cycle water chemistry, as shown in Figure 35. Again, SCCGR did not fluctuate over the on-the-fly change from EOC LiOH to mid-cycle chemistry and remained consistent throughout the evaluation.

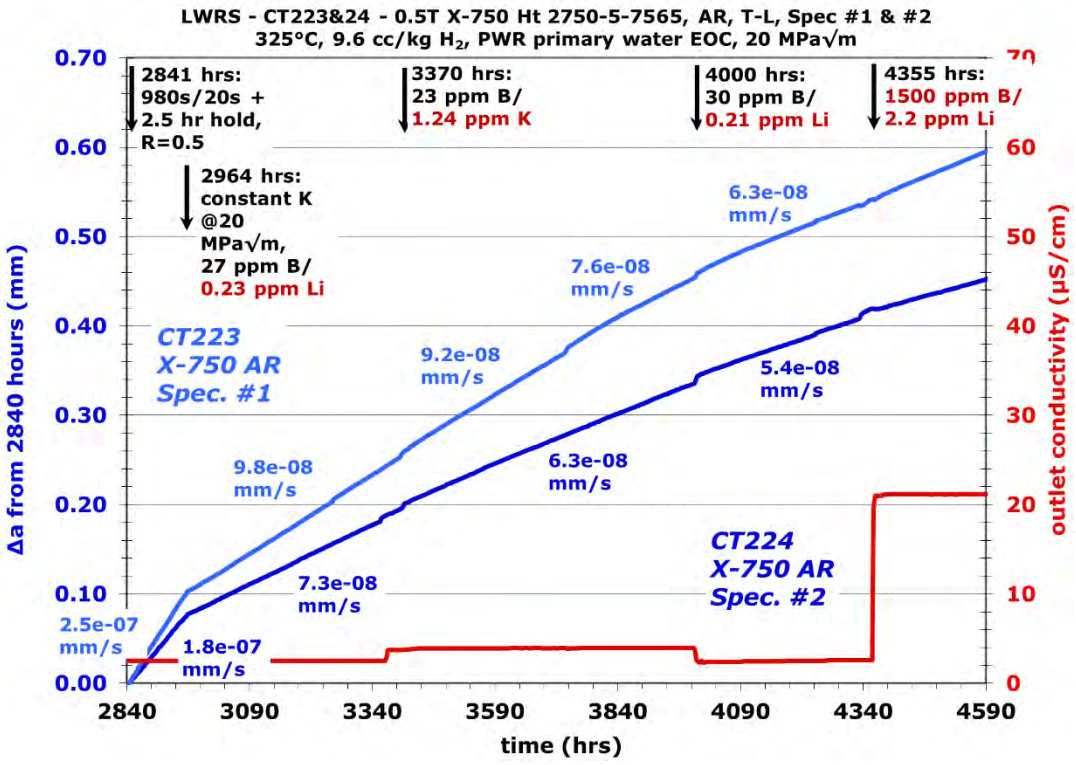

Figure 32. SCCGR response of CT223 & 224 in 325°C PWR primary water EOC chemistry with on-the-fly changes between LiOH and KOH.

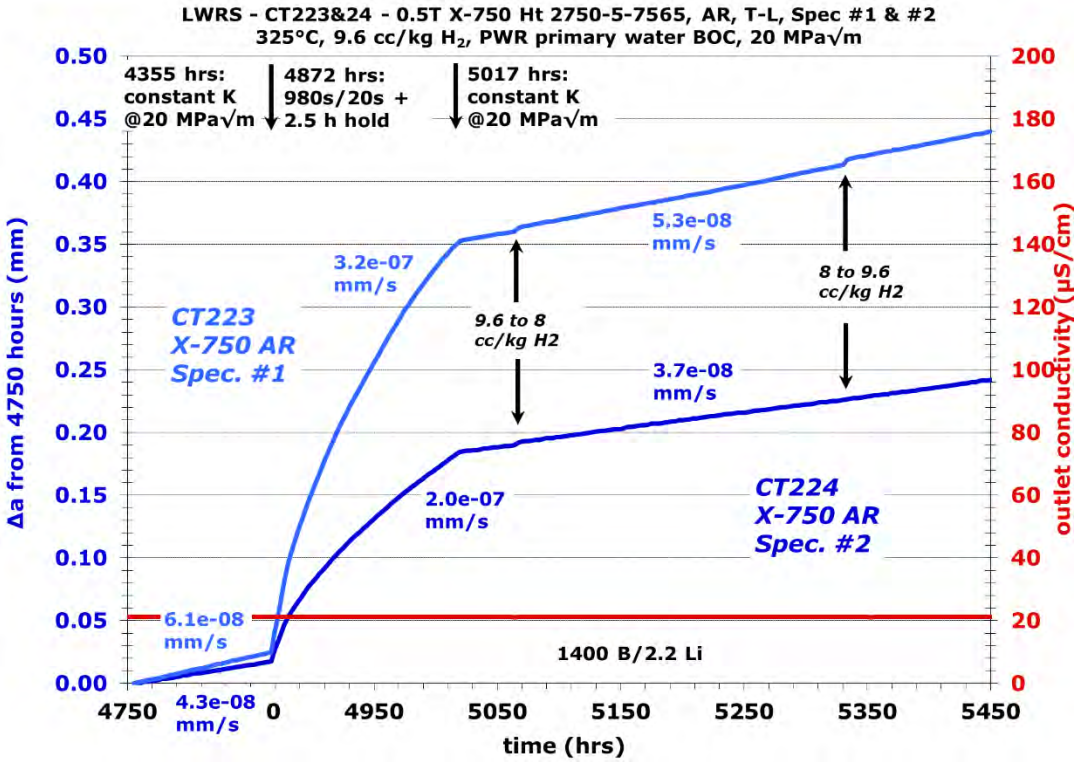

Figure 33. CGR response of CT223 & 224 in 325°C PWR primary water after the water chemistry changed back from EOC to BOC chemistry.

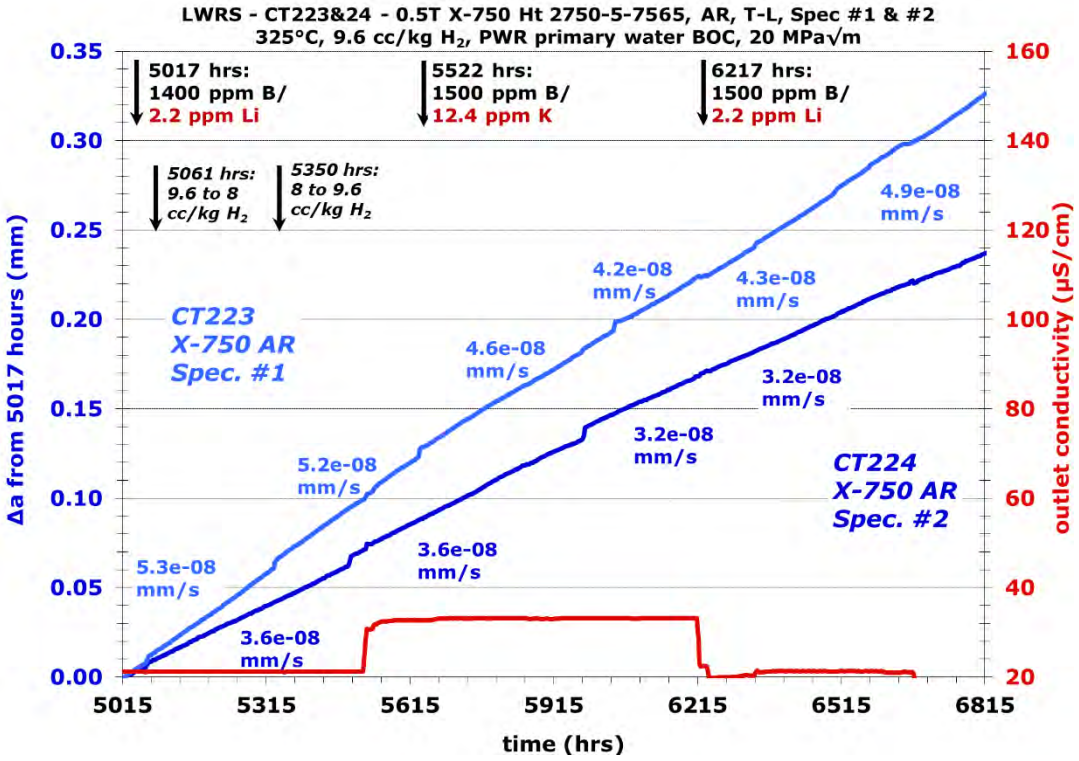

Figure 34. SCCGR response of CT223 & 224 in 325°C PWR primary water during the second BOC chemistry evaluation with on-the-fly changes between LiOH and KOH.

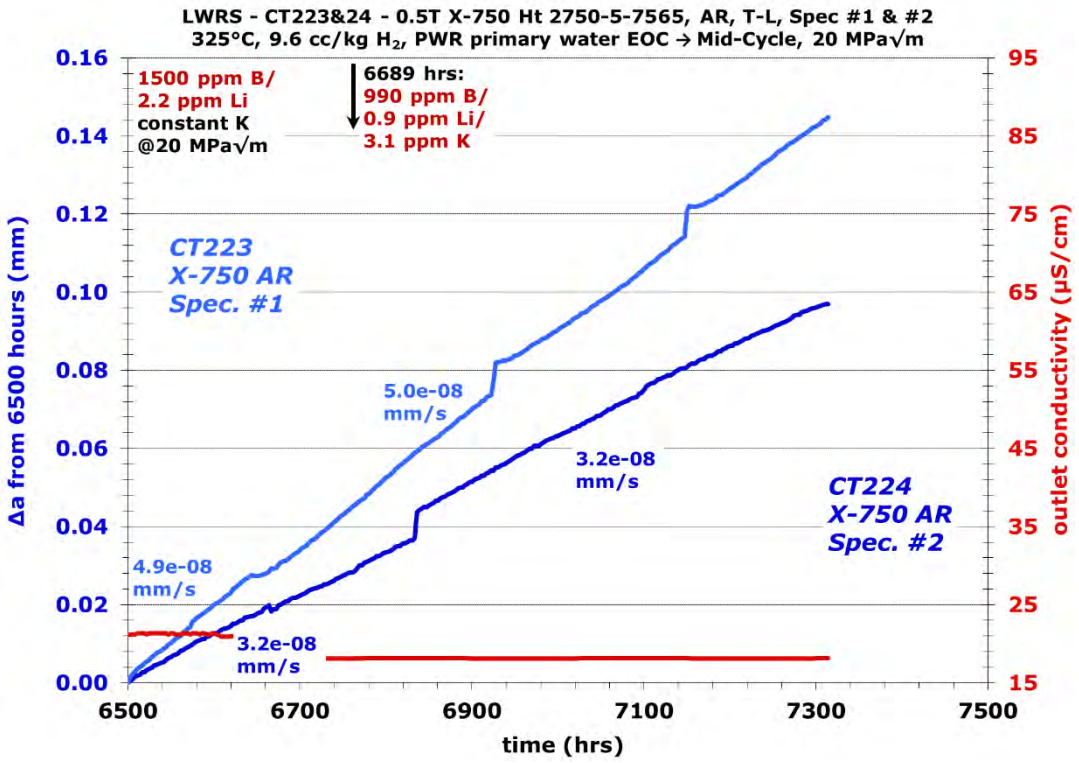

Figure 35. SCCGR response of CT223 & 224 in 325°C PWR primary water with on-the-fly change from EOC chemistry to mid-cycle chemistry.

4.2 Post-Test Characterization

After completion of the SCC growth rate test, CT223 and CT224 were removed from the test system, fatigue opened in air, and water bathed in deionized water to remove excess loose corrosion products accumulated on the crack surface. Optical and SEM characterizations were then performed on the crack growth surface of these two specimens to examine crack morphology and verify DCPD indicated crack length. The optical and SEM images are presented in Figures 36–38 for CT223 and Figures 39–41 for CT224, respectively. Despite the uneven pre-crack length observed in side grooves in the two specimens before the test (especially in CT223), the post-test optical micrographs revealed a relatively straight environmental crack front in both specimens (Figures 36 and 39). Nevertheless, some unbroken ligaments and off-plane cracking still exist in the primary crack growth surface of these two specimens, as highlighted in orange and blue, respectively. The average crack length from the notch was measured at ~7.04 mm in CT223 and ~6.50 mm in CT224, which are ~26% and ~8% higher than the DCPD estimated crack length. The difference between the actual and estimated crack length is acceptable considering the uncertainty in the DCPD measurement method (Section 2.1.3) and the complex microstructure of this tested material. The latter was evidenced in Figures 38 and 41 for CT223 and CT224, respectively, where the primary crack propagated intergranularly through highly banded microstructures with clusters of small grains interspersed in a network of >10X larger grains. In addition, cracking that formed at constant load and cyclic loading steps can be differentiated by the different coloration of oxides observed under low-kV SEM BSE imaging (Figure 37 for CT223 and Figure 40 for CT224). Two darker, strata-like bands are readily visible and sandwich a lighter band in between in the environmental crack portion in the crack growth surface of both specimens. The difference, in contrast, is caused by the different thickness of the oxide layer formed on the grains, which are further associated with the time the crack spent propagating in the specific areas. Therefore, the lighter region observed in the middle of the crack surface likely corresponds to the cycling steps implemented between 2,172–2,964 hours, while the darker bands can be

correlated to the two constant load evaluation periods during the early and later phase of the test. It is worthy to note that the morphology in the crack growth surface is 100% intergranular, including the portion that had undergone cyclic loading, confirming that Alloy X-750 is very susceptible to SCC propagation in PWR primary water.

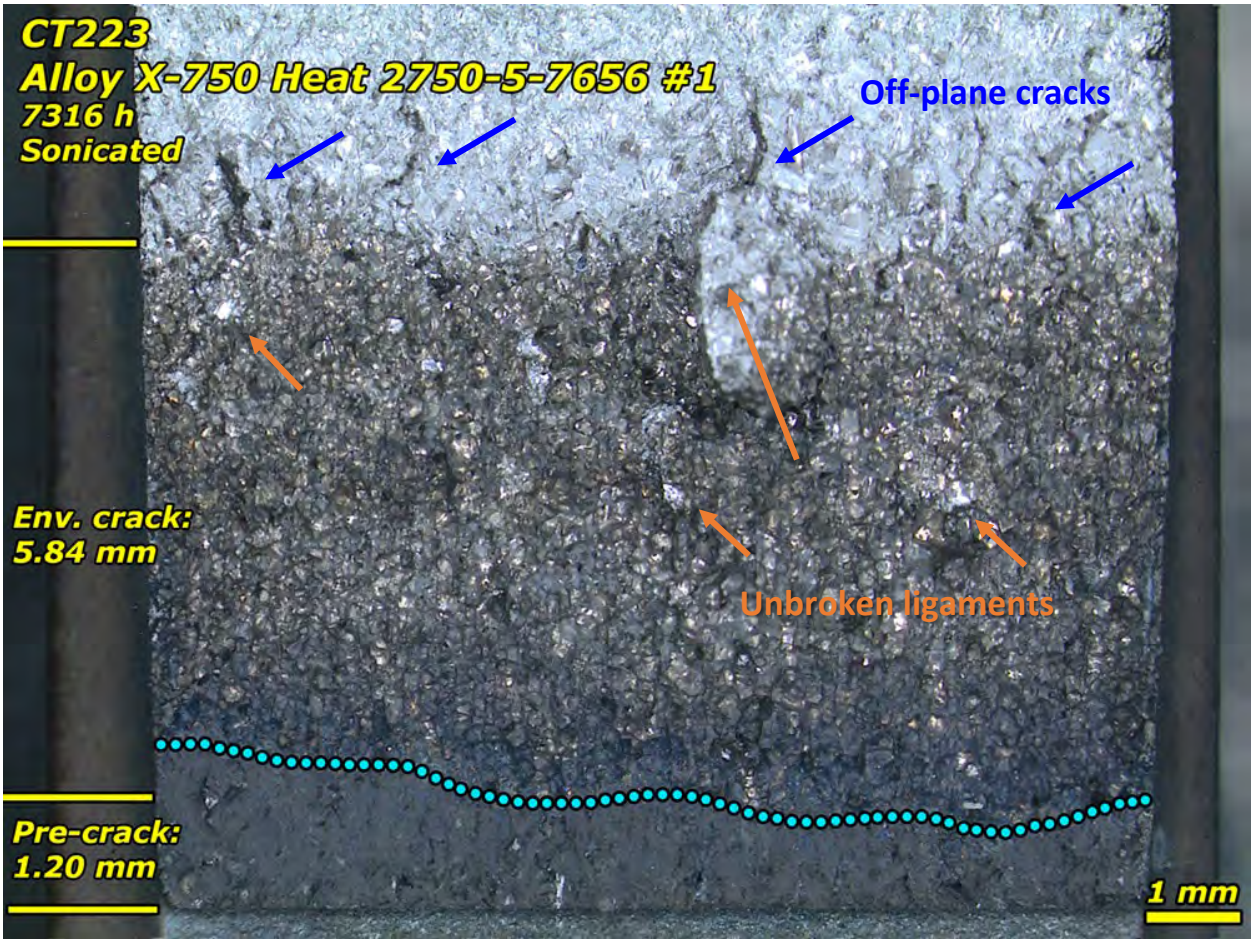

Figure 36. Post-test optical image of the crack growth surface of CT223. The extent of the fatigue pre-crack is highlighted by the blue dotted line. The average pre-crack length and environmental crack length are marked in yellow on the left.

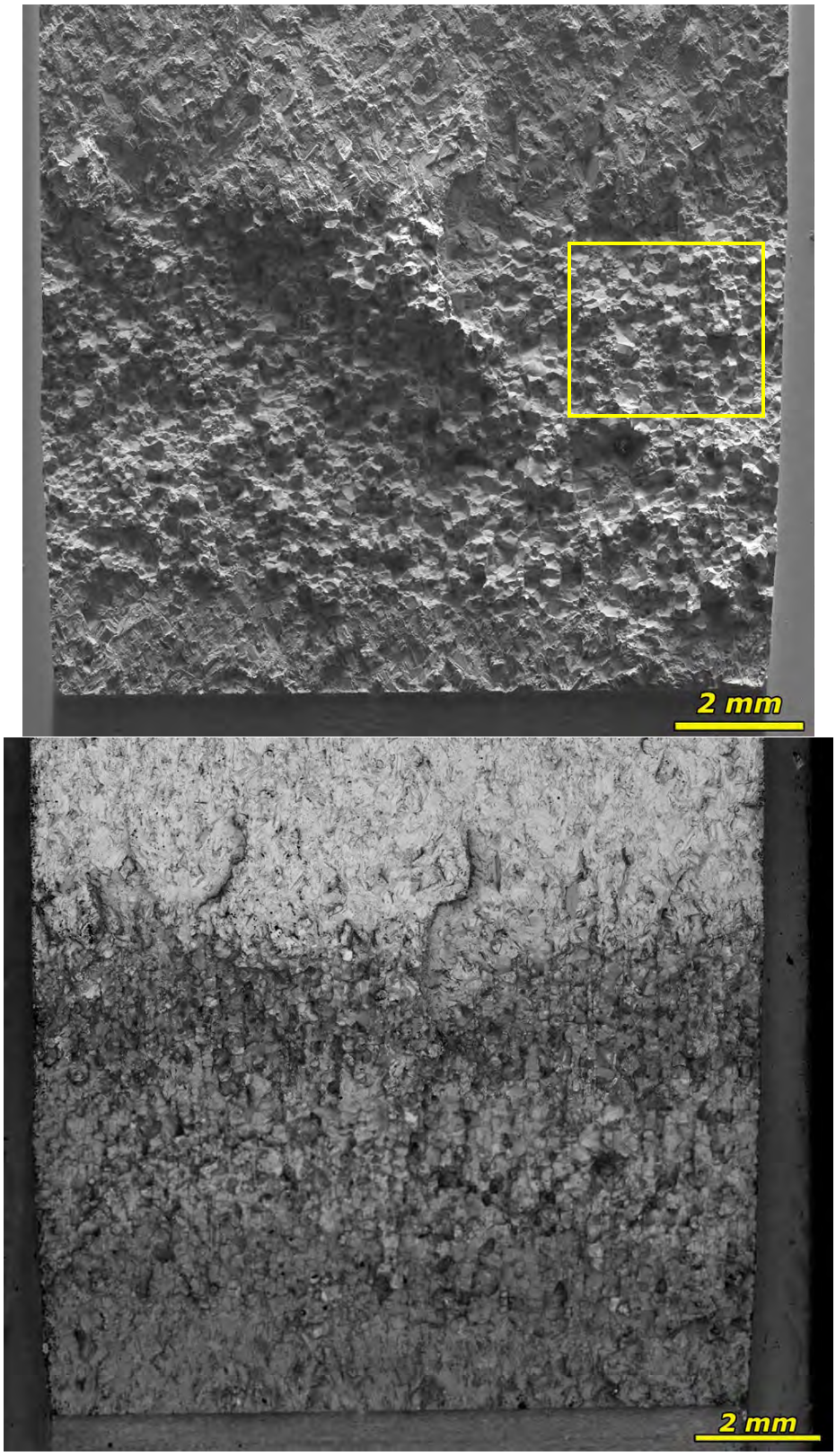

Figure 37. Post-test SEM image (top - SE, bottom – BSE) of the crack growth surface of CT223.

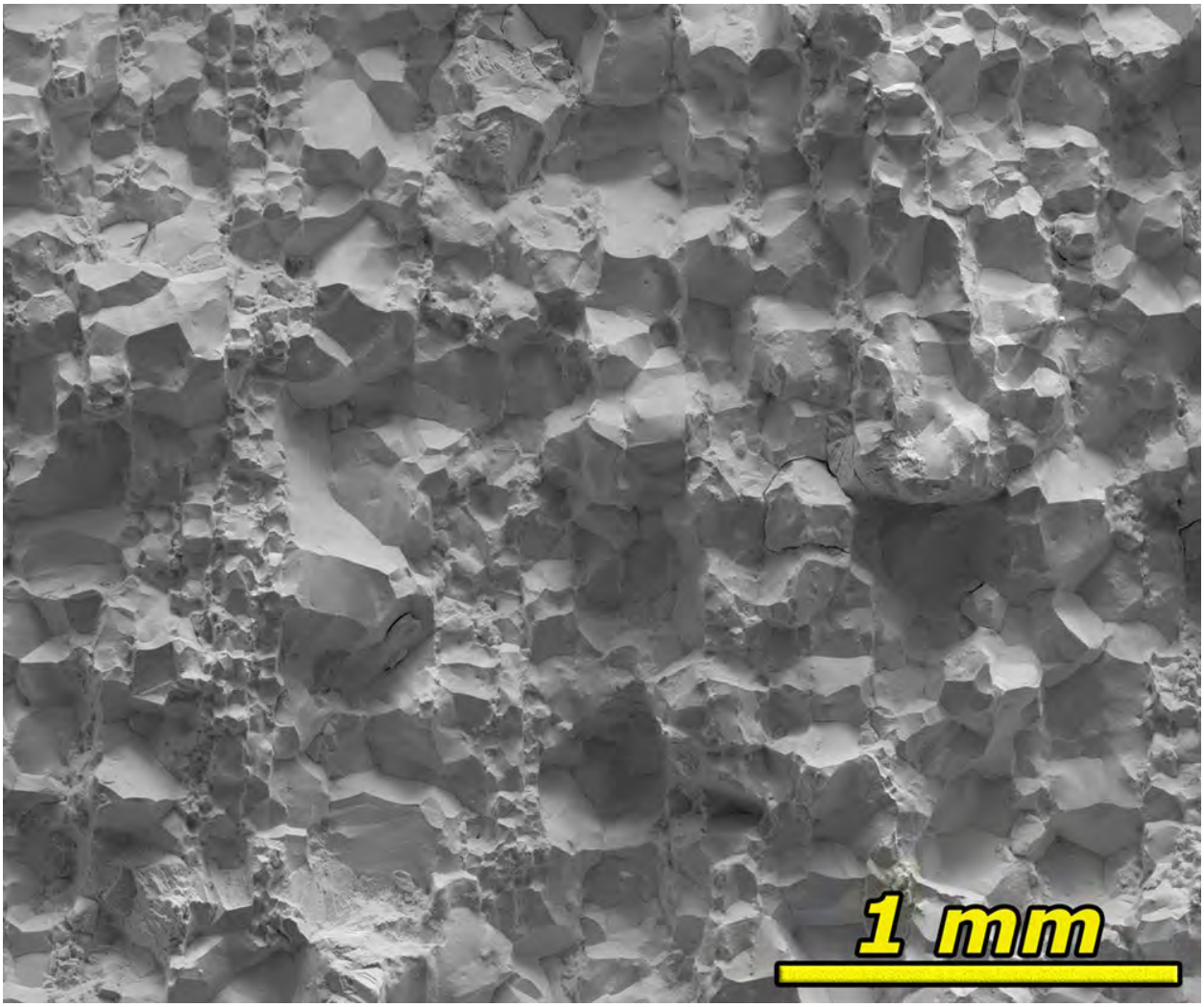

Figure 38. Zoom-in SEM-SE image of the representative crack growth surface morphology of the area highlighted in Figure 37 in CT223. The crack growth surface is 100% IG.

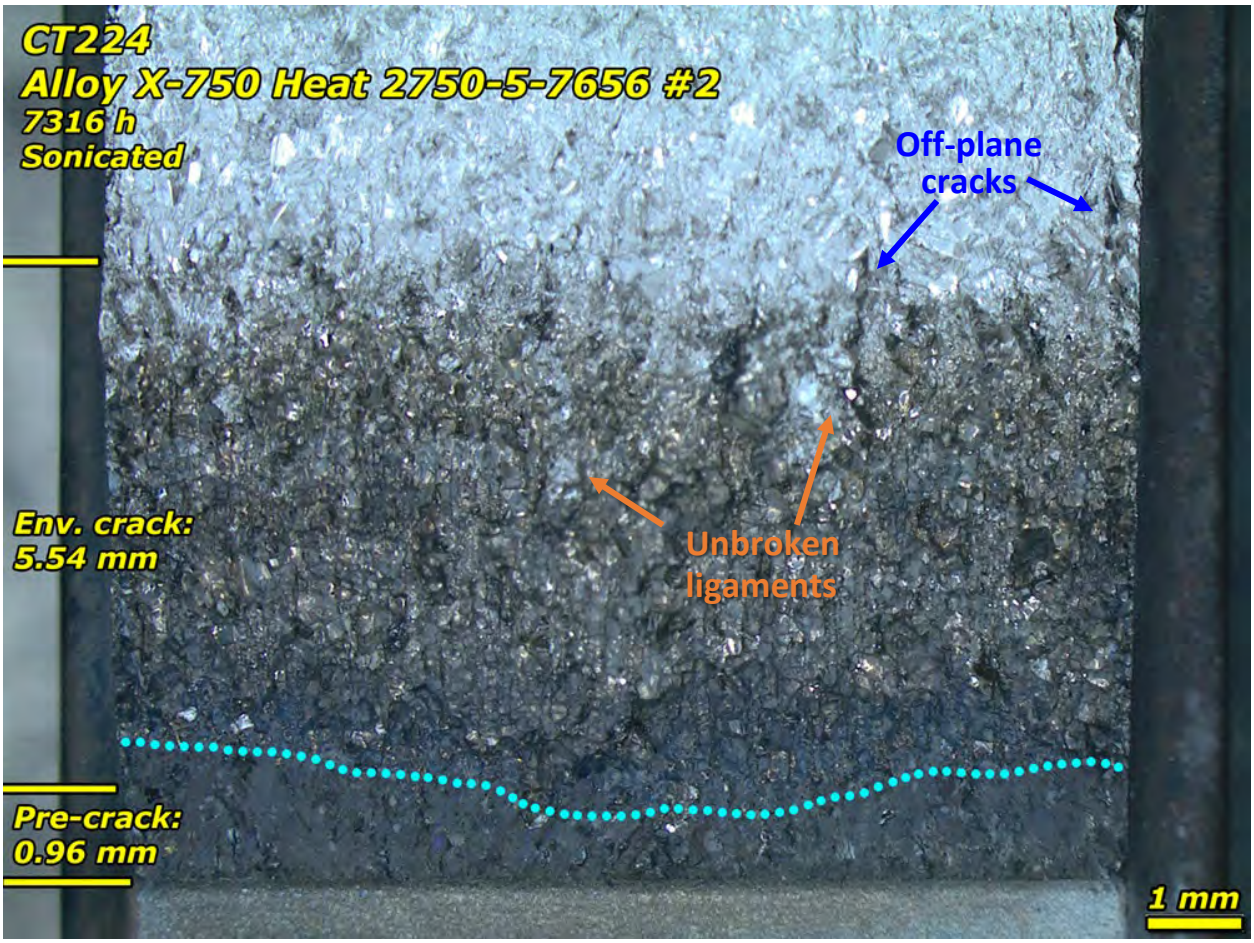

Figure 39. Post-test optical image of the crack growth surface of CT224. The extent of the fatigue pre-crack is highlighted by the blue dotted line. The average pre-crack length and environmental crack length are marked in yellow on the left.

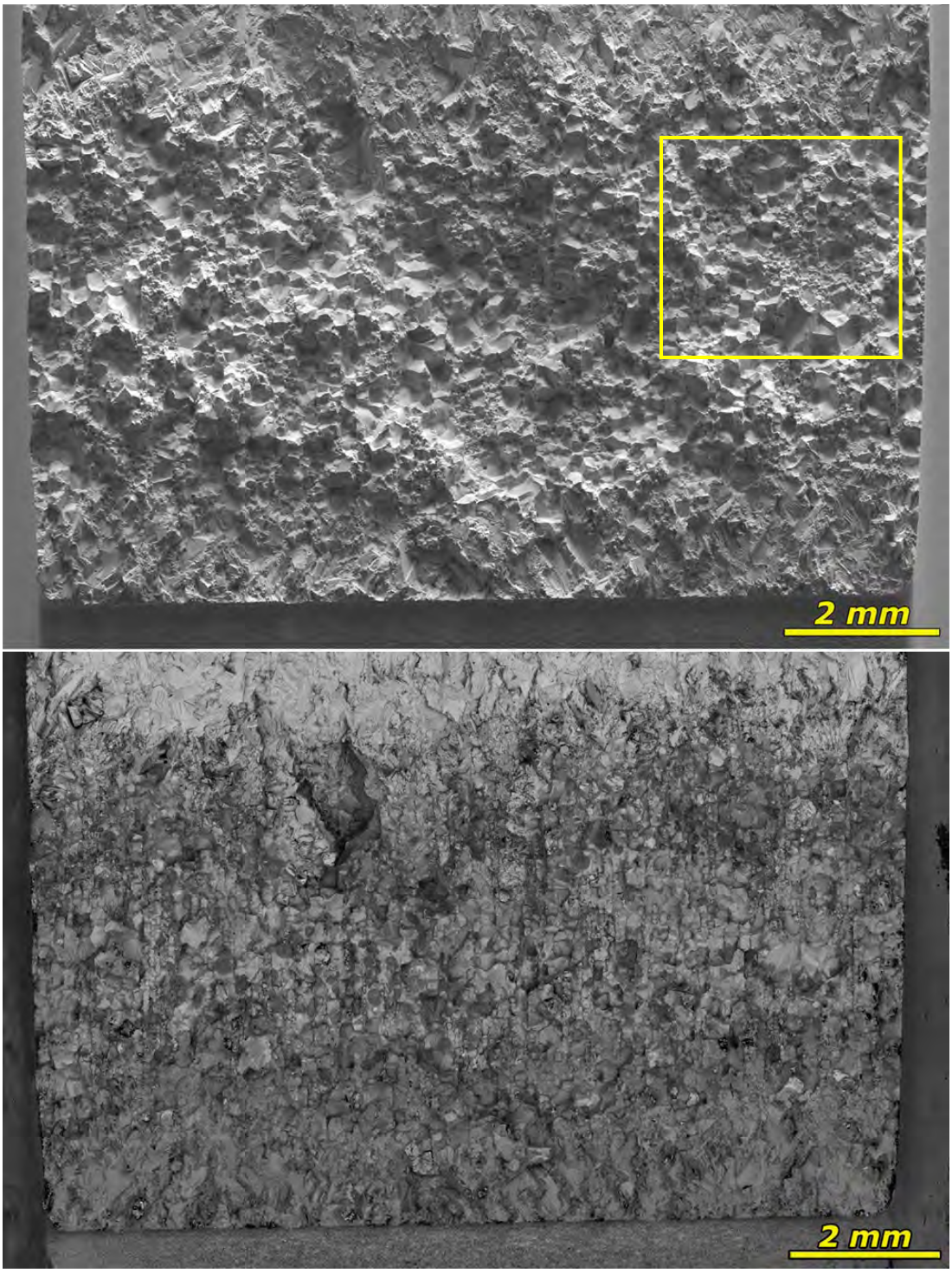

Figure 40. Post-test SEM image (top - SE, bottom – BSE) of the crack growth surface of CT224.

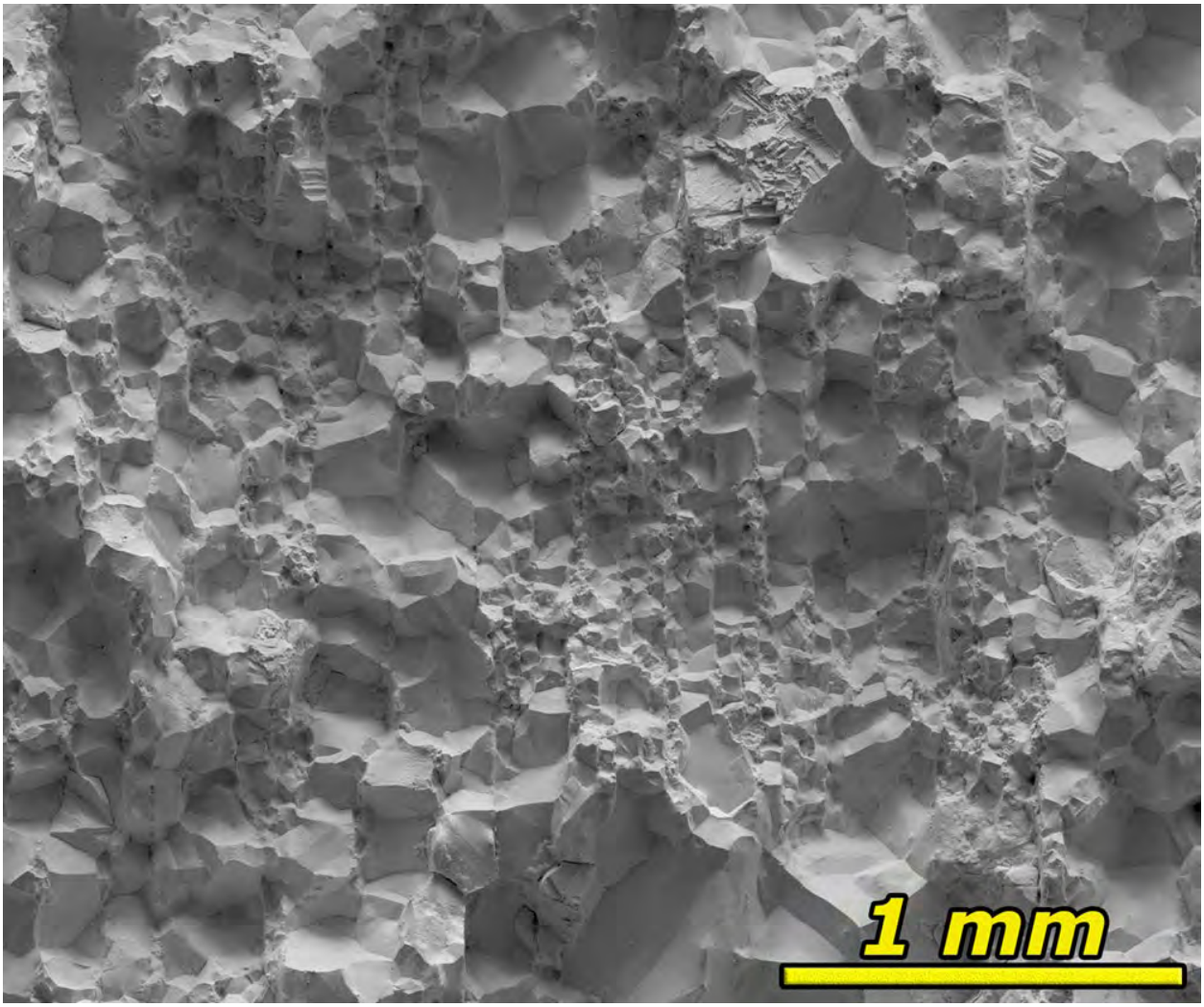

Figure 41. Zoom-in SEM-SE image of the representative crack growth surface morphology of the area highlighted in Figure 40 in CT224. The crack growth surface is 100% IG.

5. SCC CRACK GROWTH BEHAVIOR OF Alloy 718 IN KOH VS. LIOH-CONTAINING PWR PRIMARY WATER

5.1 SCC Growth Rate Test

Because precipitation-hardened Alloy 718 has a reputation of being very resistant to PWSCC initiation but relatively susceptible to propagation once an IG crack is initiated, only SCC growth rate testing is carried out for this material to investigate the KOH vs. LiOH effect on SCCGR. Two 0.5T CT specimens were extracted from the precipitation-hardened Alloy 718 block in the S-L orientation relative to the plate fabrication direction. This orientation was selected for its potentially maximized SCC susceptibility so that the test can be completed in a reasonable time frame. These two specimens, CT226 and CT227, were first fatigue precracked individually in air at room temperature following the procedure described in Section 2.1.2. The side grooves of these two specimens were polished to a 1 μm finish, allowing the precrack morphology to be viewed and its length to be measured. The results are shown in Figures 42 and 43 for CT226 and 227, respectively. CT227 exhibited a more uniform precrack length on both sides (1.045 vs. 1.136 mm) than CT226 (1.048 vs. 1.448 mm) and was therefore selected as the leading specimen for the SCC growth rate test. This means that the load control during the test would be implemented based on the response of CT227, whereas CT226 acts as a redundant companion specimen to confirm whether material behavior is reproducible under similar material and loading conditions.

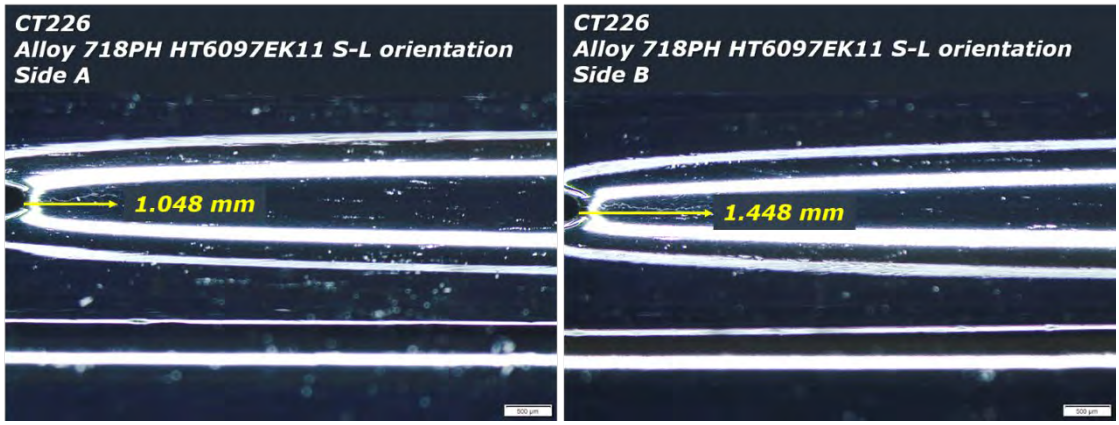

Figure 42. Optical micrographs of the polished side grooves of the Alloy 718 specimen CT226. The length of the precrack produced by air fatigue is marked in both side grooves.

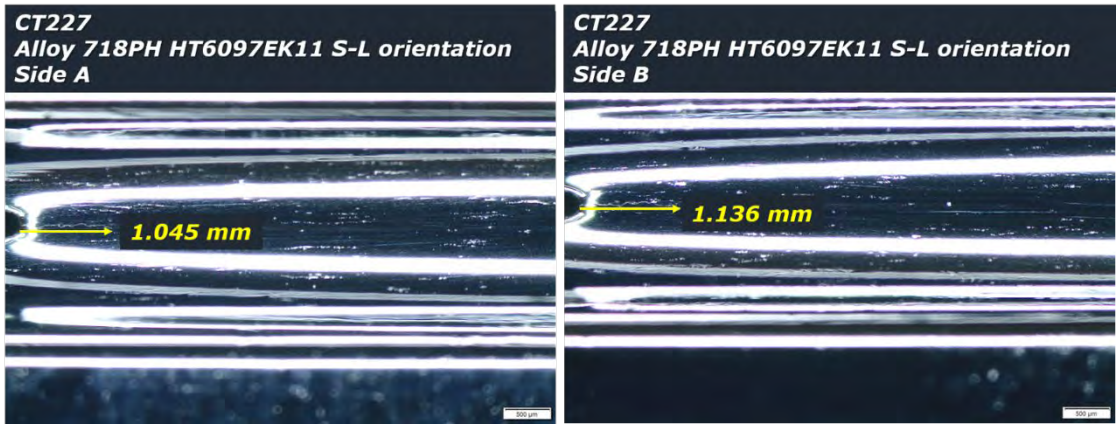

Figure 43. Optical micrographs of the polished side grooves of the Alloy 718 specimen CT227. The length of the precrack produced by air fatigue is marked in both side grooves.

The two specimens were loaded in series into an NRC SCC test system, and the test was started in the baseline PWR primary water containing 1500 ppm B and 2.2 ppm Li at 360 °C and 25 cc/kg H_2. A test overview of the referenced DCPD crack growth response of CT226 and CT227 is provided in Figure 44. The SCCGR evaluation of both specimens has been completed in all three water chemistries specified in Table 1 at constant load. As expected, the applied load on the controlling sample CT227 has been constant at ~25–26 MPa√m throughout the test. In comparison, the load on the companion sample CT226 had continued to increase due to a positive dK/da effect, likely because of the longer pre-crack length as indicated by the pre-test side groove crack length measurements (Figures 42 and 43).

The test started in the BOC-LiOH water chemistry containing 1500 ppm B and 2.2 ppm Li. Figure 45 presents the initial cyclic loading steps implemented with decreasing frequency to transition the TG precrack produced by air fatigue to an IGSCC crack front. This includes cyclic loading from 1.0 to 0.01 Hz at a load ratio of 0.5 and a K_{max} of 20 MPa√m, followed by a final cycling step of a 980 s rise and a 20 s fall (0.001 Hz) with R = 0.5 in a sawtooth form. Decreasing CGRs were observed for both specimens during the more and more gentle cycling at each step. No further reduction in CGR was observed once a 2.5 h hold time was added to the final cyclic loading step (Figure 46), but this is not uncommon for materials that are highly susceptible to SCC growth. The absolute values of the SCCGR under these conditions was not as high as we had hoped, so to accelerate the test process, an increase in K_{max} from 20 to 25 MPa√m via dK/da was implemented over a crack extension of 15 μm, as can be seen in Figure 46. This produced an approximate 3x increase in CGR during cycle+hold loading, which was deemed a sufficient increase in CGR to likely allow constant load observations to take place in a reasonable period of time. The test was then transitioned to constant load at 25 MPa√m for SCCGR evaluation between LiOH vs. KOH containing PWR primary water in the BOC condition. Figure 47 presents the SCCGR response of CT226 and CT227 through the entire BOC chemistry evaluation period with three on-the-fly changes between LiOH and KOH. SCCGR data of both specimens were continuously collected for at least 300 hours after each change, allowing assessments of not only the crack growth behavior immediately after the water chemistry change, but also the CGR after the new water chemistry was fully stabilized. As shown in Figure 47, the SCCGR of CT226 and CT227 were monotonic in general throughout the entire course of the BOC chemistry evaluation, with an average SCCGR of ~1.6–1.7×10^{-7} mm/s for CT226 and ~1.1–1.4×10^{-7} mm/s for CT227. A slight decrease in SCCGR was observed immediately after each switch between LiOH and KOH. Still, the magnitude was relatively small (≤20%), and the SCCGR always climbed back to similar values acquired at the previous step after the water chemistry fully stabilized. SCCGR evaluation of the EOC water chemistry followed directly after completing the 2nd SCC assessment in KOH BOC chemistry at the same constant load condition. As shown in Figure 48, CT227 exhibited similar SCCGR values as those obtained in the BOC water chemistry evaluation and had little or no change during switches from KOH to LiOH and back over a relatively long assessment time (>500 hours). In comparison, the SCCGR in CT226 continued to increase over the entire evaluation period in EOC water chemistry, primarily due to increased crack growth under an increasing dK/da effect. This is unavoidable when the crack length is longer in the companion specimen than in the controlling specimen tested in the same system. As indicated in Figure 48, the applied load is estimated to have increased from 26 to 34 MPa√m by the time the EOC water chemistry evaluation was completed, resulting in almost doubled SCCGR compared to that at the beginning of the EOC period. However, no obvious difference was observed in the SCCGR of the ±100 hours of each switch between KOH and LiOH. Finally, a mid-cycle SCCGR evaluation was performed for 500 hours, as shown in Figure 49. Again, the SCCGR returned to similar values in the previous step after a short initial decrease at the beginning of the water chemistry change.

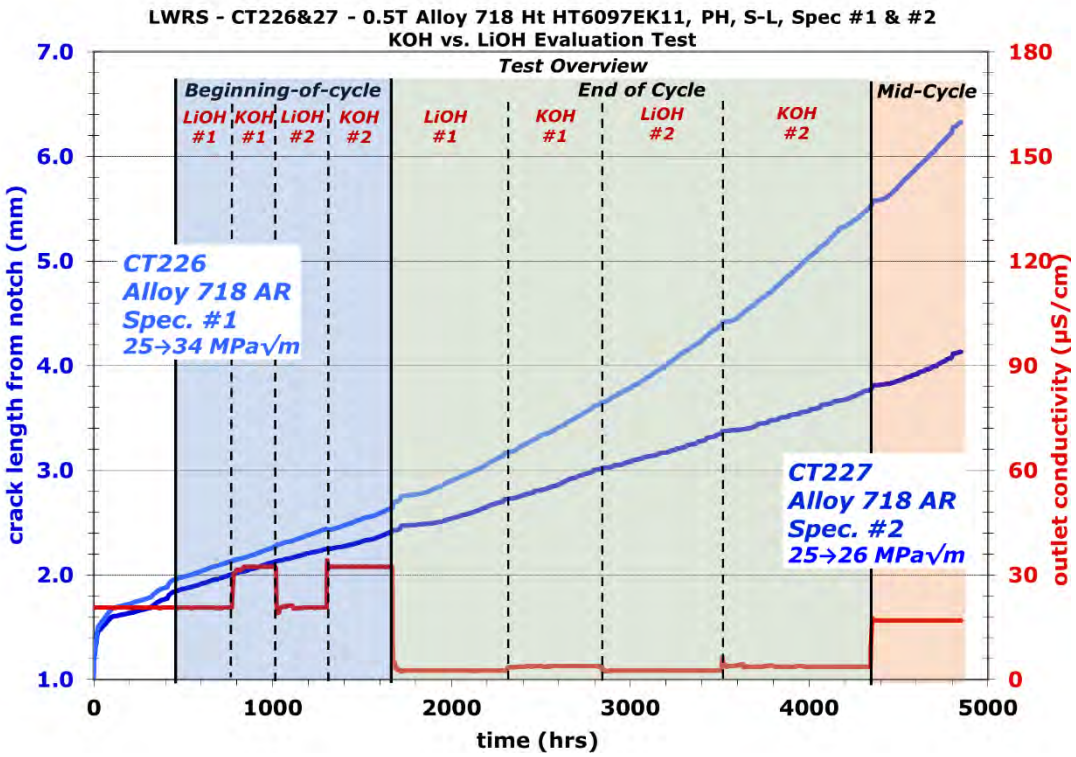

Figure 44. Test overview of crack growth response in the two Alloy 718 specimens CT226 & 227 tested in S-L orientation. The effect of KOH vs. LiOH on the SCCGR of both specimens is evaluated in 360°C simulated PWR primary water at 25 cc/kg H_2.

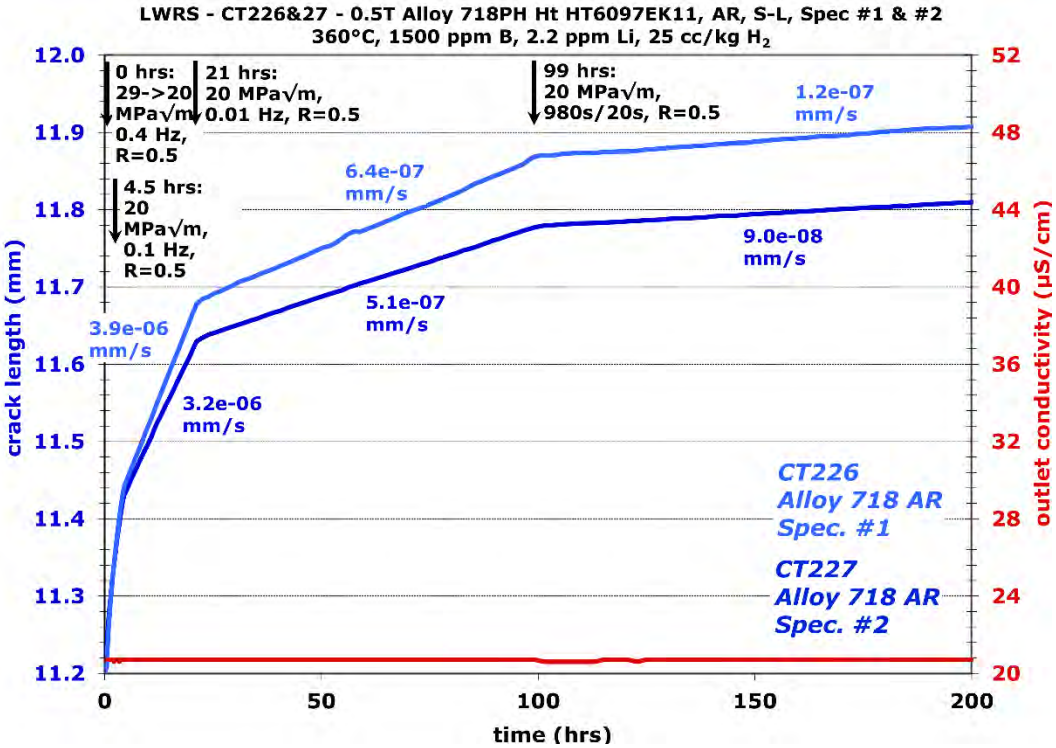

Figure 45. Crack growth response of the two Alloy 718 specimens CT226 & 227 during initial cyclic loading transition steps in 360°C simulated PWR primary water.

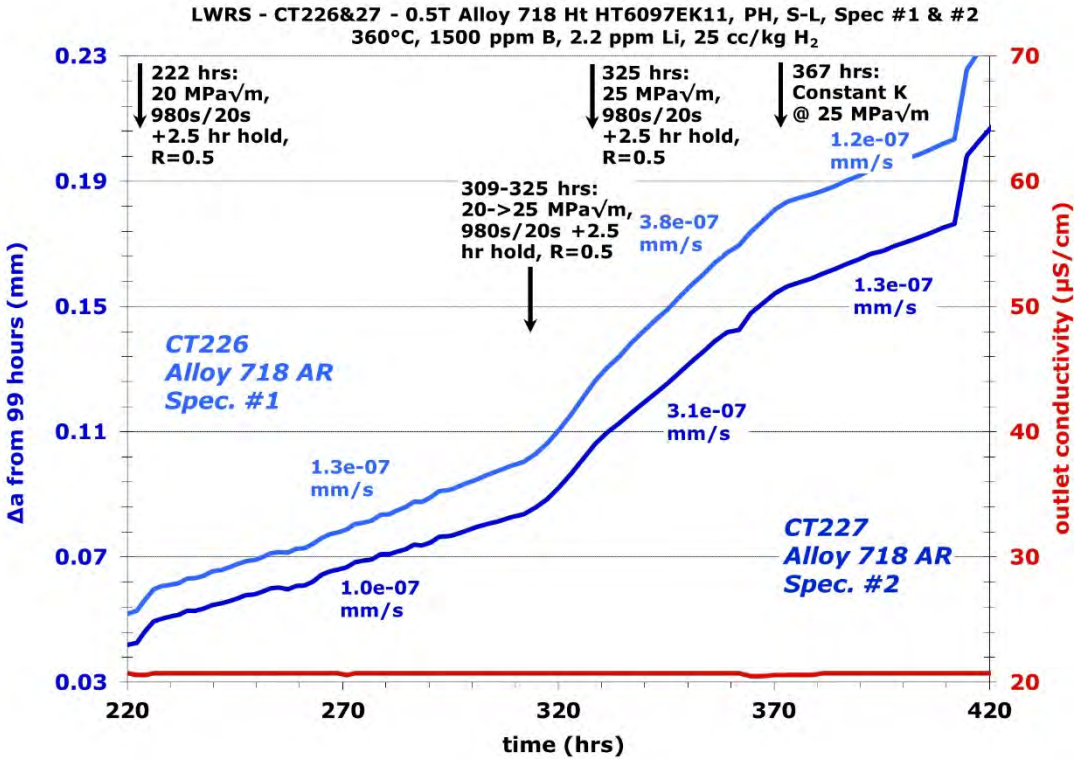

Figure 46. Crack growth response of the initial cycle+hold and constant load evaluation of the two Alloy 718 specimens CT226 & 227 in 360°C simulated PWR primary water with 25 cc/kg H_2.

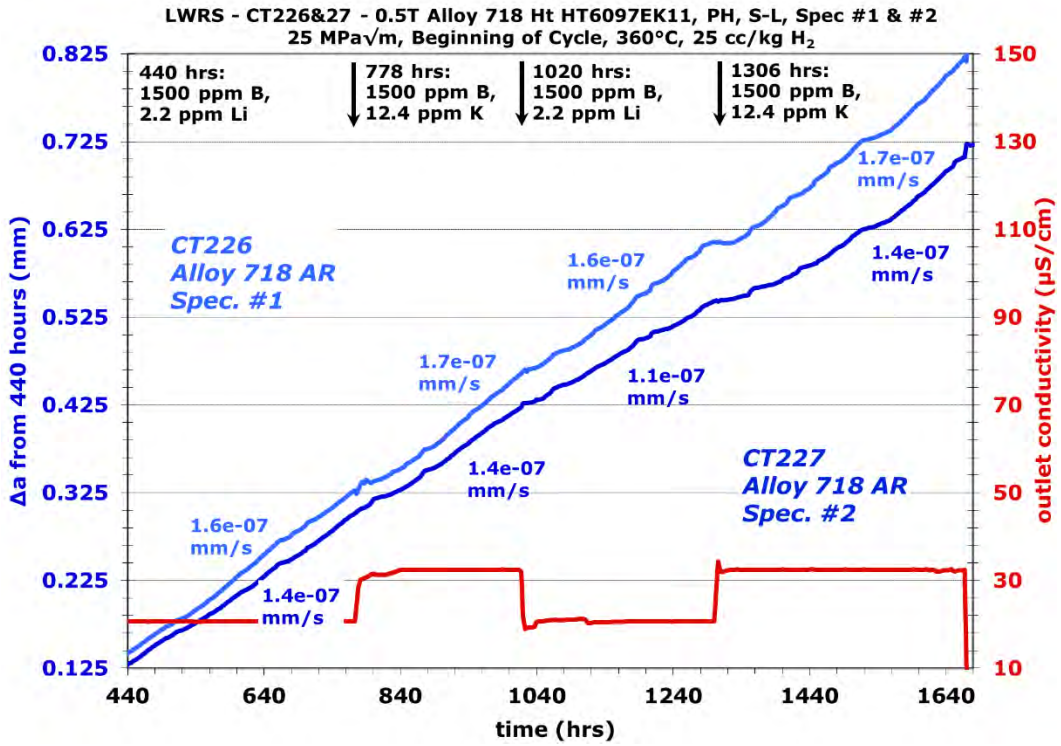

Figure 47. SCCGR response of the two Alloy 718 specimens CT226 & 227 in 360°C PWR primary water BOC chemistry with on-the-fly changes between LiOH and KOH.

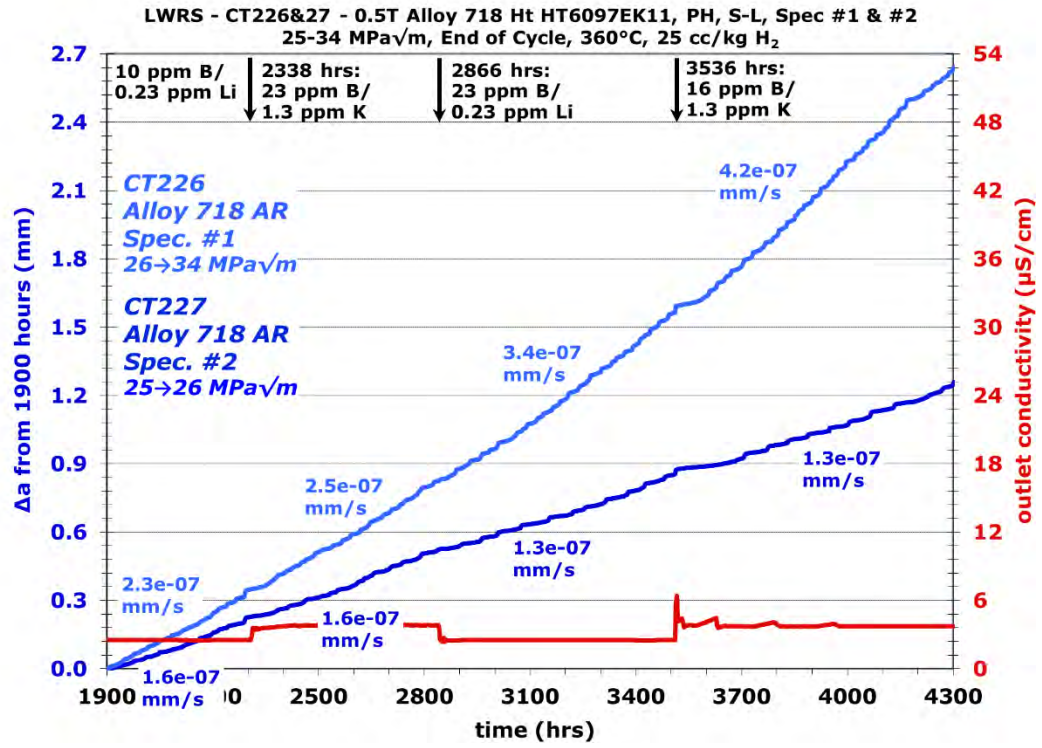

Figure 48. SCCGR response of the two Alloy 718 specimens CT226 & 227 in 360°C PWR primary water EOC chemistry with on-the-fly changes between LiOH and KOH.

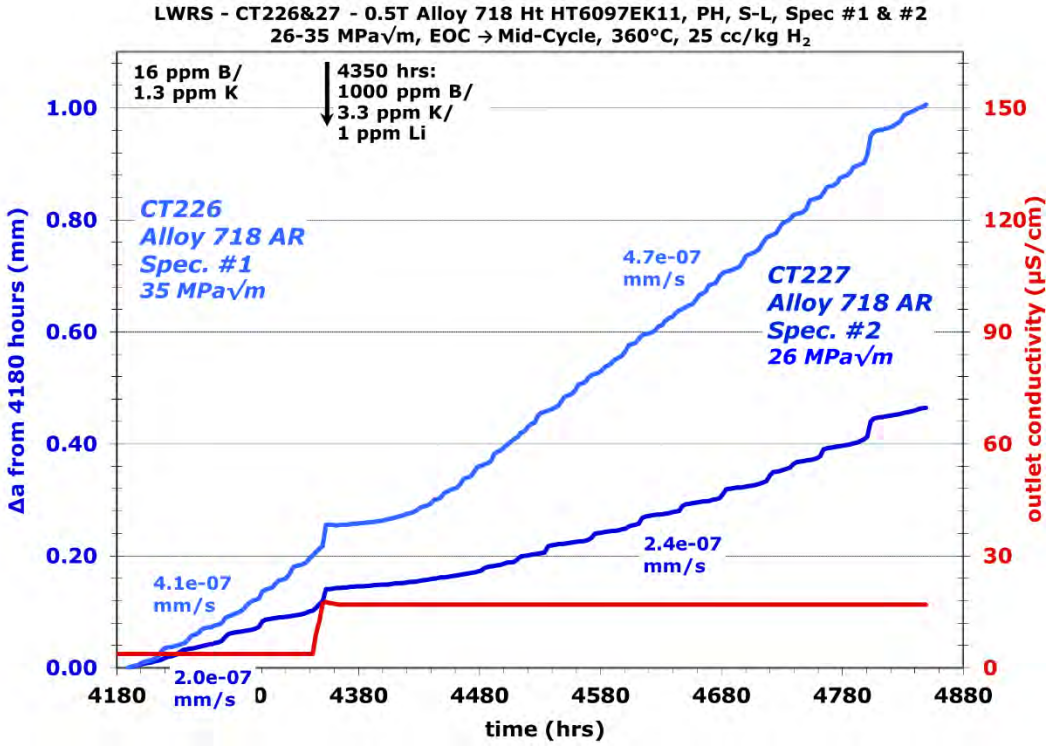

Figure 49. SCCGR response of the two Alloy 718 specimens CT226 & 227 in 360°C PWR primary water with on-the-fly change from EOC chemistry to mid-cycle chemistry.

5.2 Post-Test Characterization

Optical and SEM characterizations were performed on CT226 and CT227 after the conclusion of the test to examine crack morphology and verify DCPD indicated crack length. Side groove examination of CT226 revealed a crack extension of ~5.9 mm in Side A and ~6.2 mm in Side B. The cracking in the side grooves was continuous for the first ~3/5 fraction of the crack. In comparison, the last ~2/5 fraction exhibited multi-planar, intermittent cracks intersecting the side groove surfaces indicative of extensive cracking (Figure 50). Similar observations were made on CT227, albeit it exhibited shorter crack lengths (4.4 and 4.5 mm) in both side grooves (Figure 54). The two specimens were then fatigue opened in air to examine the crack growth surface. The optical and SEM images are presented in Figures 51–53 for CT226 and Figures 55–57 for CT227, respectively. Both specimens showed a relatively uniform crack front in the main crack growth plane and a 100% intergranular morphology during the constant load evaluation that underwent multiple on-the-fly water chemistry changes (Figures 53 and 57). Small unbroken ligaments (with bright contrast in the optical and SEM-BSE images) were also observed in the crack growth surface of both specimens, but only to a minor degree. In addition, it turned out the crack along the side grooves did not grow all the way to the crack front revealed in the crack growth surface in both specimens. This is a known issue for crack growth testing due to the lack of constraints along the side grooves. Although it underestimated the actual crack length, the difference does not affect the objective of this test. Based on the measurements performed on the crack growth surface in both specimens (Figures 51 and 55), the actual total crack length from the notch is ~6.78 mm in CT226 and 5.12 mm in CT227. These values suggest that DCPD underestimated the crack length by ~7% in CT226 and ~24% in CT227, which are acceptable discrepancies considering the uncertainty in DCPD measurements as discussed in 2.1.3. While this indicates that the SCCGR measured by DCPD would be lower than the actual SCCGR, the difference should be small and would not impact the SCCGRs differently in KOH and LiOH-containing water chemistries therefore no correction was made.

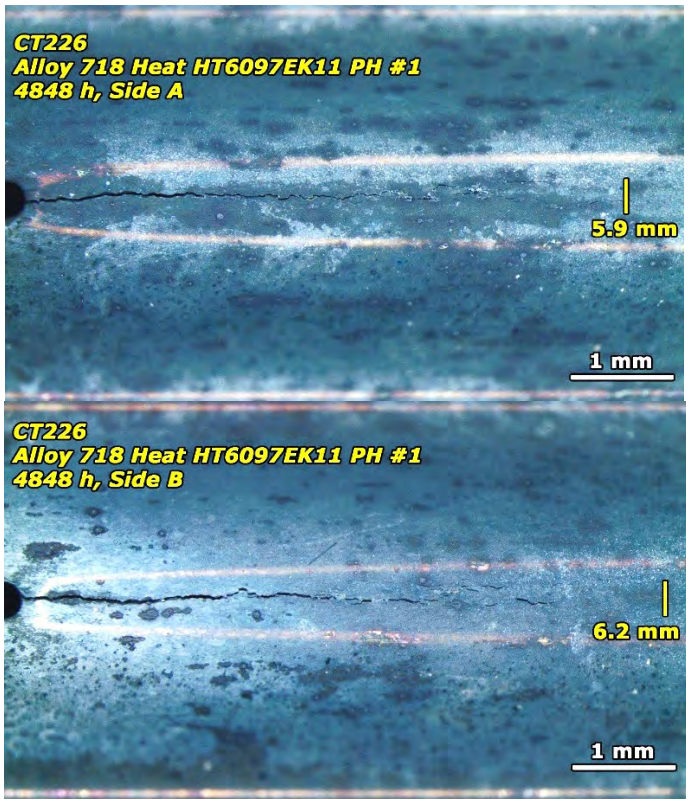

Figure 50. Post-test optical micrographs of the side grooves of CT226 (top – Side A, bottom – Side B).

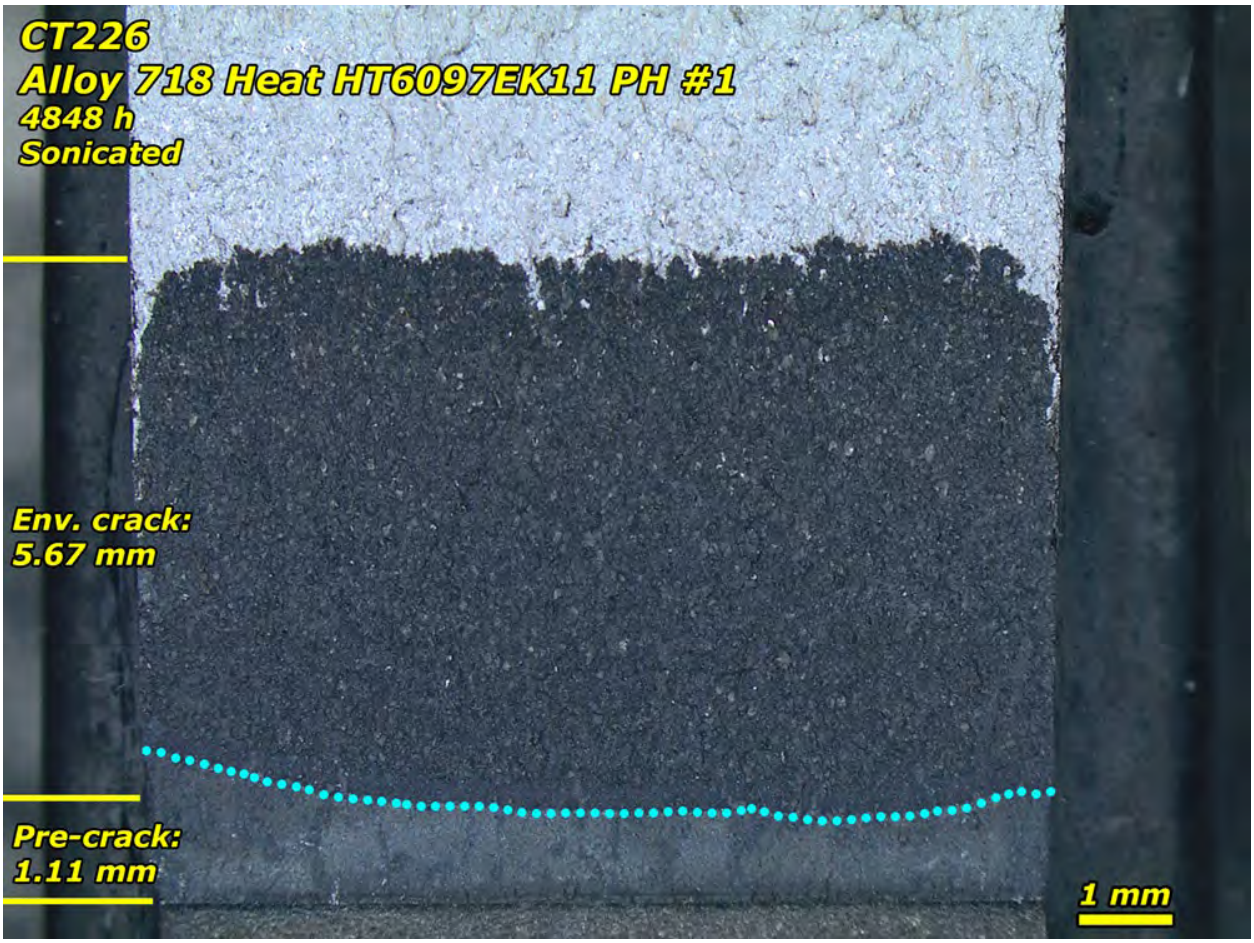

Figure 51. Post-test optical image of the crack growth surface of CT226. The extent of the fatigue pre-crack is highlighted by the blue dotted line. The average pre-crack length and environmental crack length are marked in yellow on the left.

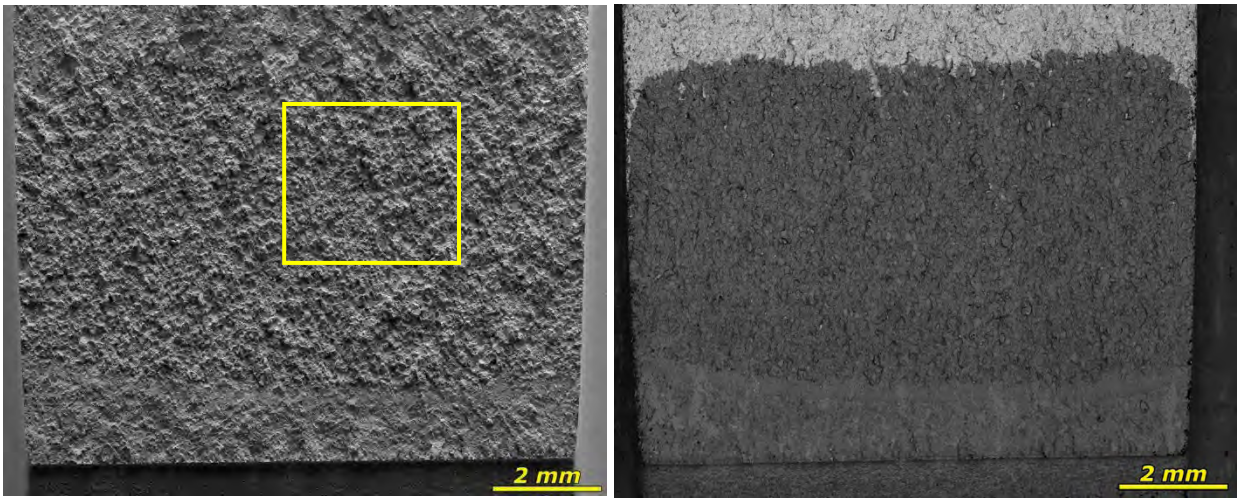

Figure 52. Post-test SEM image (left - SE, right – BSE) of the crack growth surface of CT226.

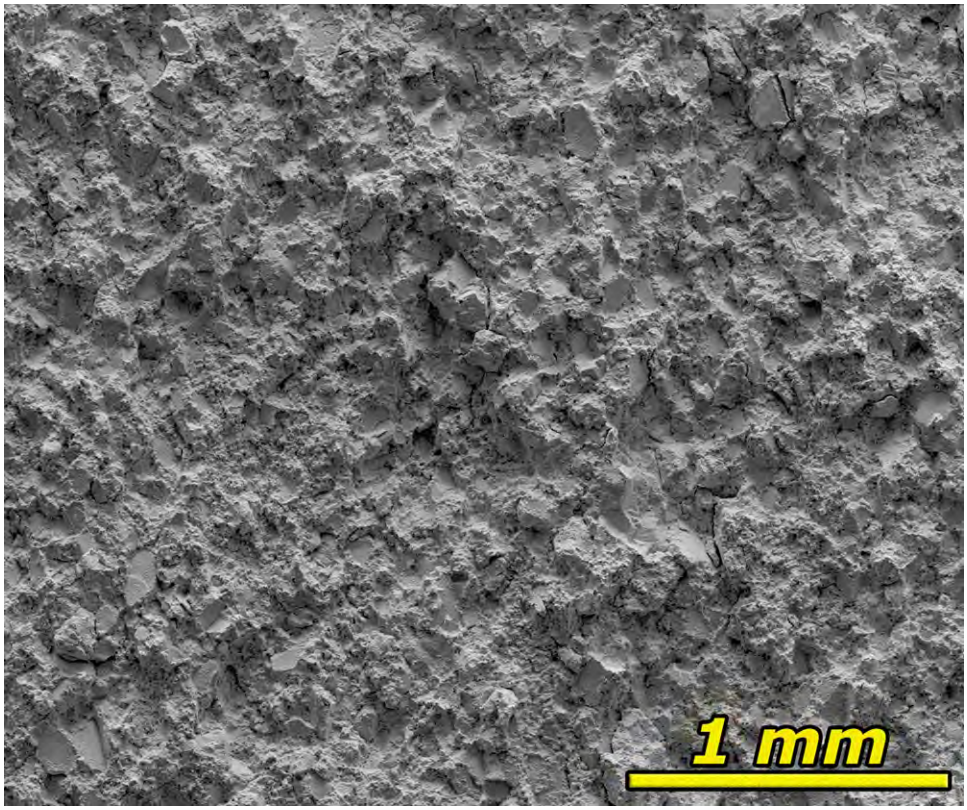

Figure 53. Zoom-in SEM-SE image of the representative crack growth surface morphology of the area highlighted in Figure 52 in CT226. The crack growth surface is 100% IG.

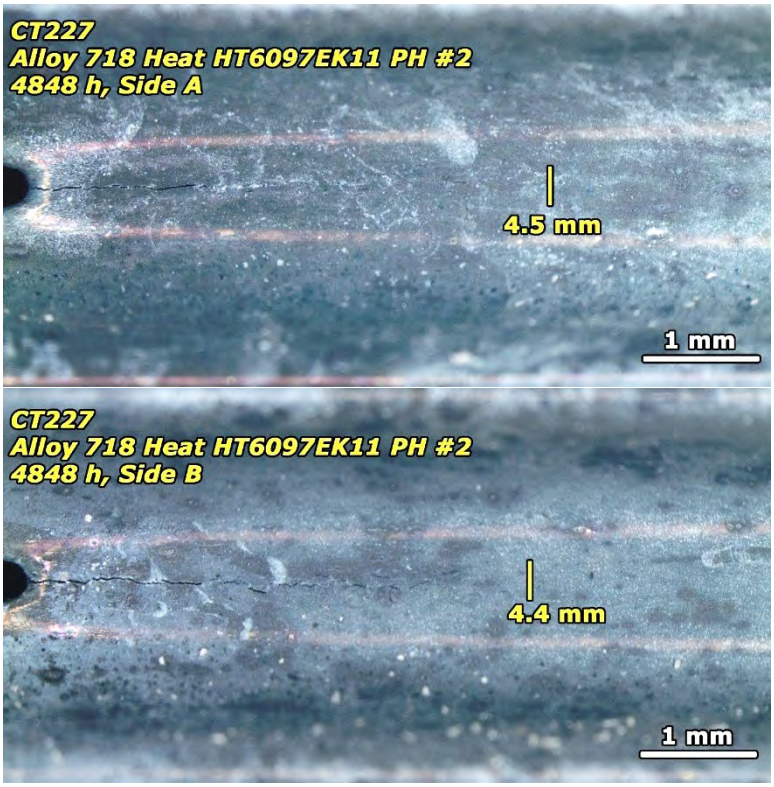

Figure 54. Post-test optical images of the side grooves of CT227 (top – Side A, bottom – Side B).

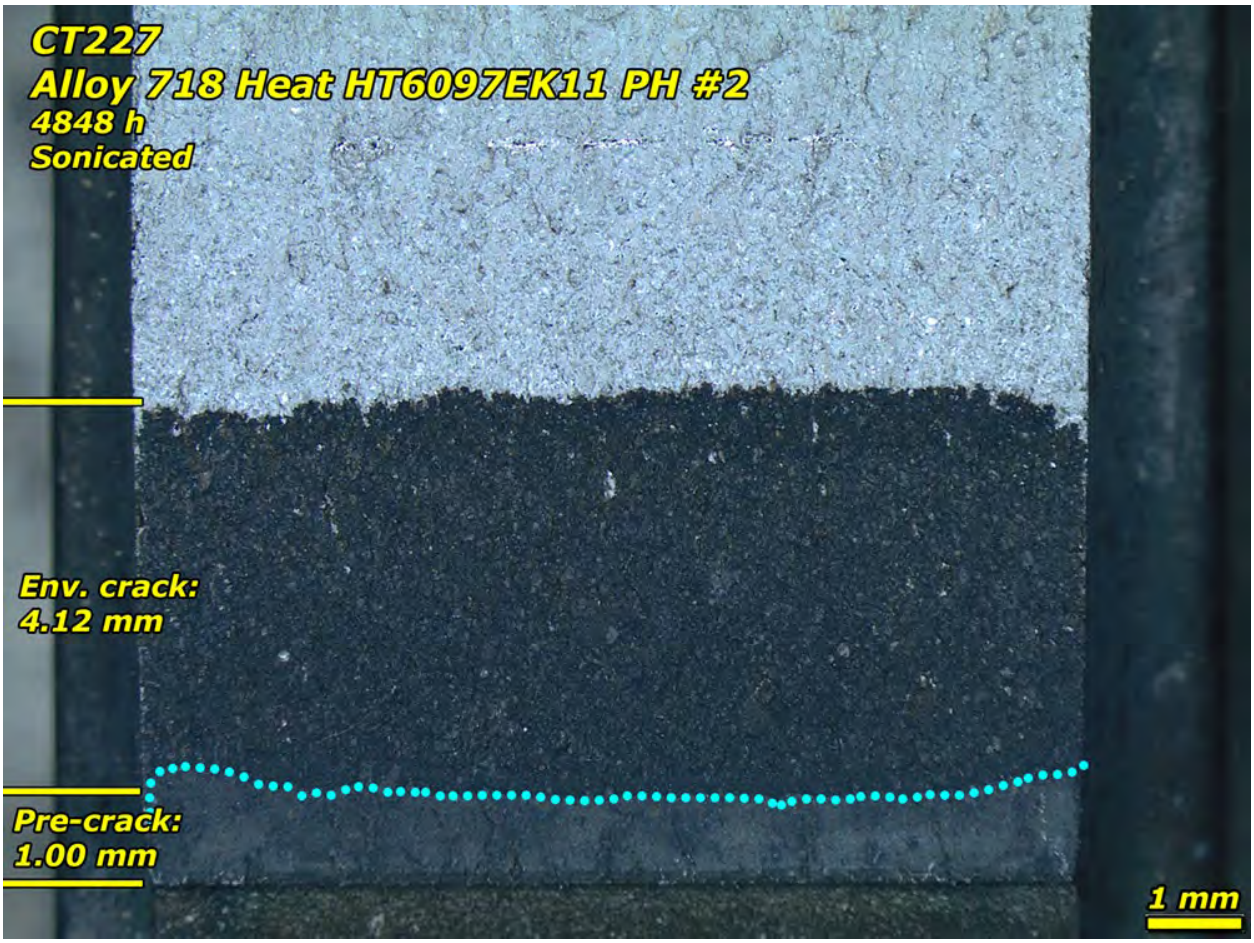

Figure 55. Post-test optical image of the crack growth surface of CT227. The extent of the fatigue pre-crack is highlighted by the blue dotted line. The average pre-crack length and environmental crack length are marked in yellow on the left.

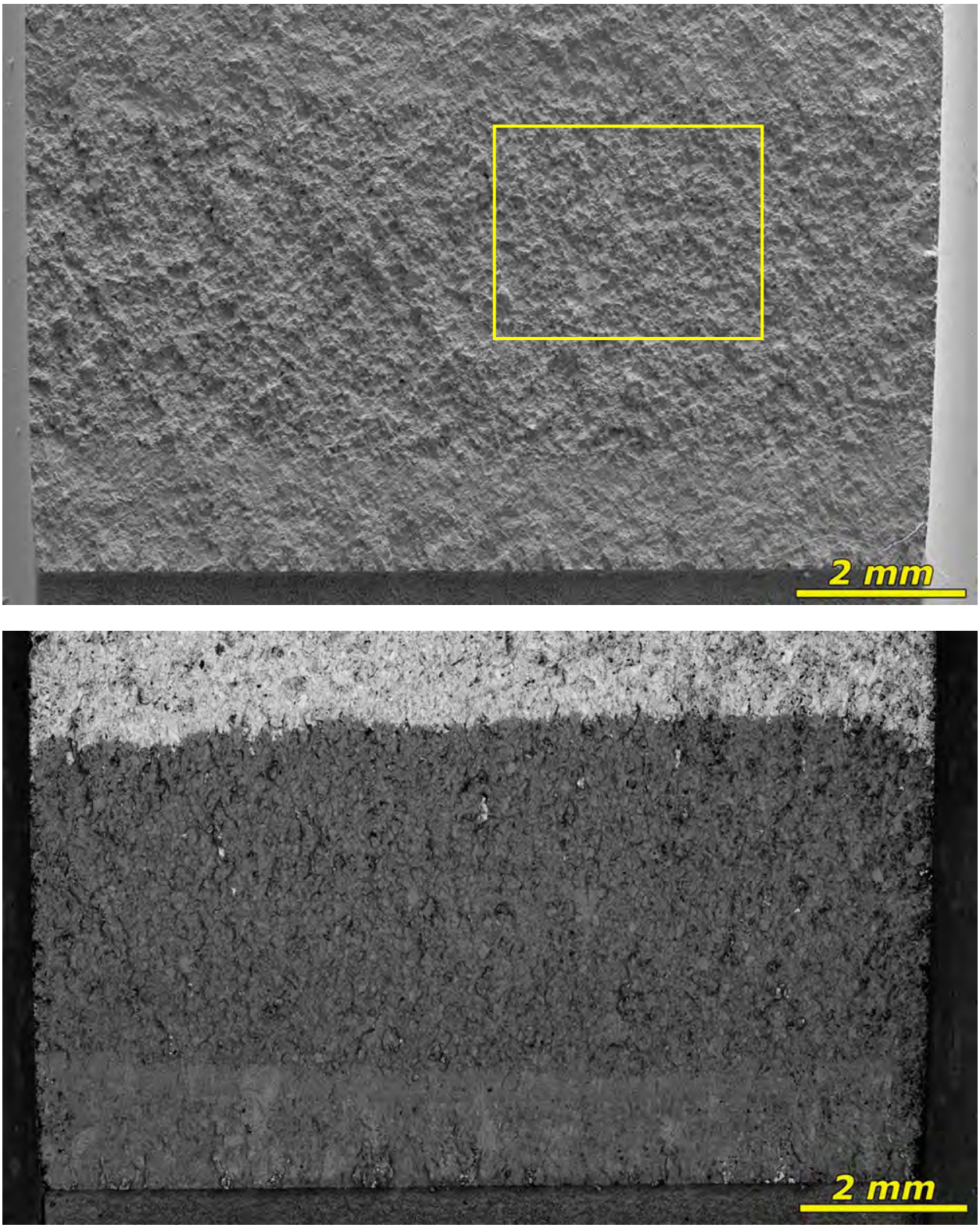

Figure 56. Post-test SEM image (top - SE, bottom – BSE) of the crack growth surface of CT227.

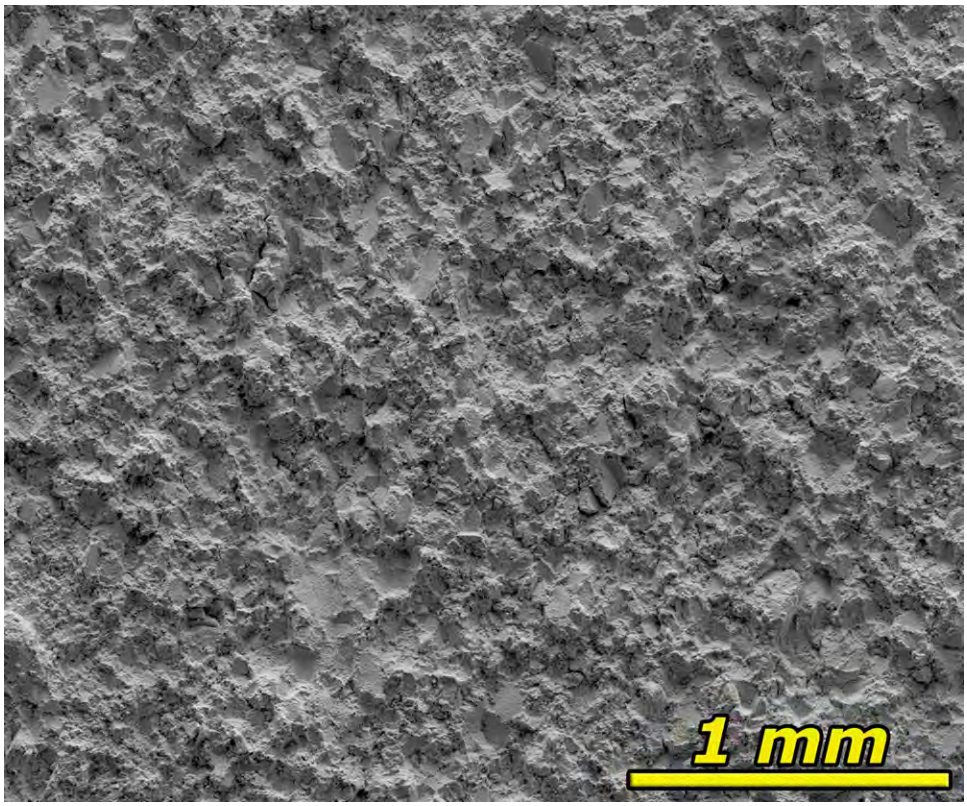

Figure 57. Zoom-in SEM-SE image of the representative crack growth surface morphology of the area highlighted in Figure 56 in CT227. The crack growth surface is 100% IG.

6. SCC CRACK GROWTH BEHAVIOR OF Alloy 82H IN KOH VS. LIOH-CONTAINING PWR PRIMARY WATER

As shown in Figure 58, one block was cut out from the "L" shaped Alloy 82H build-up in preparation for machining CT specimens for the SCC growth rate test. The welding direction is normal to the plane of the paper. Because Alloy 82H is known to be more resistant to SCC than Alloy 600 and Alloy 182, it was decided to cold forge the material to ~30% reduction in thickness to accelerate crack propagation so that the test can be completed within a reasonable timeframe. The cold work in the block was achieved by cold forging along the direction identified in Figure 58. Two 0.5T CT specimens, CT228 and CT229, were extracted from the blue-colored block in the S-L orientation for its maximized SCC susceptibility. In preparation for the SCC growth rate test, these two specimens were fatigue precracked individually in air at room temperature, following the procedure described in Section 2.1.2. The side grooves of these two specimens were polished to a 1 μm finish, allowing the precrack morphology to be viewed and its length to be measured. As shown in Figures 59 and 60, CT227 exhibited a slightly longer and more uniform precrack length on both sides (1.15 vs. 1.06 mm) than CT226 (1.13 vs. 0.94 mm) and was therefore selected as the leading specimen for the SCC growth rate test. The two specimens were then loaded in series into an NRC SCC test system, and similar to the previous two tests, the test was started in the baseline PWR primary water containing 1500 ppm B and 2.2 ppm Li at 360 °C and 26 cc/kg H_2.

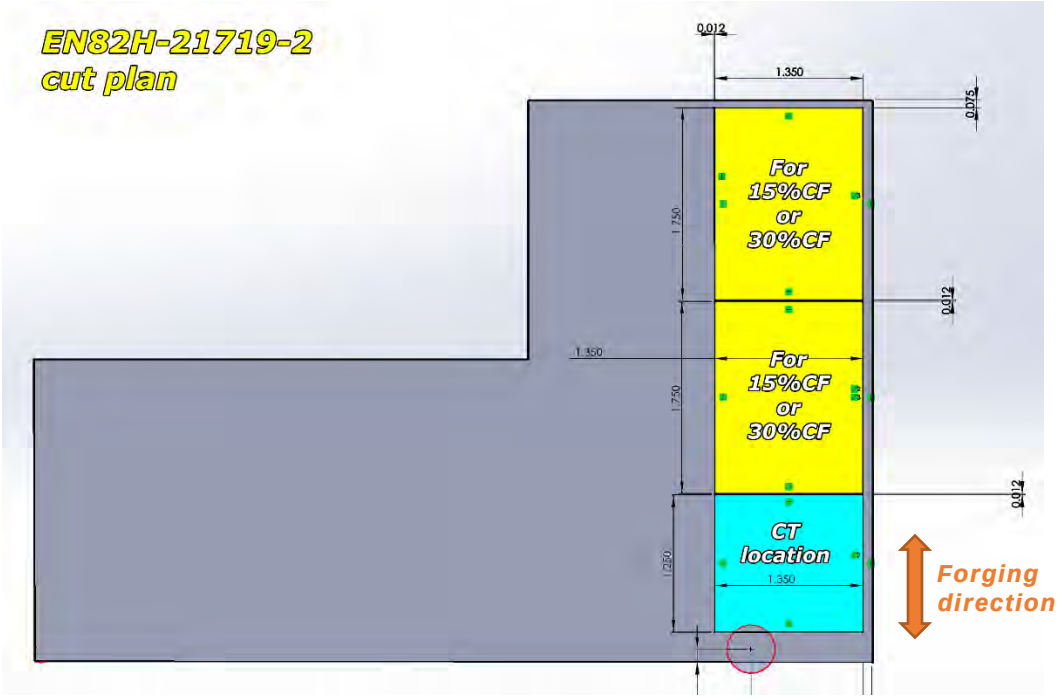

Figure 58. Cut plan of the Alloy 82H build-up shown in Figure 22 for cold forging and specimen preparation for this study. Three blocks were cut out, two for SCC initiation testing (highlighted in yellow) and one for SCC growth rate testing (highlighted in blue).

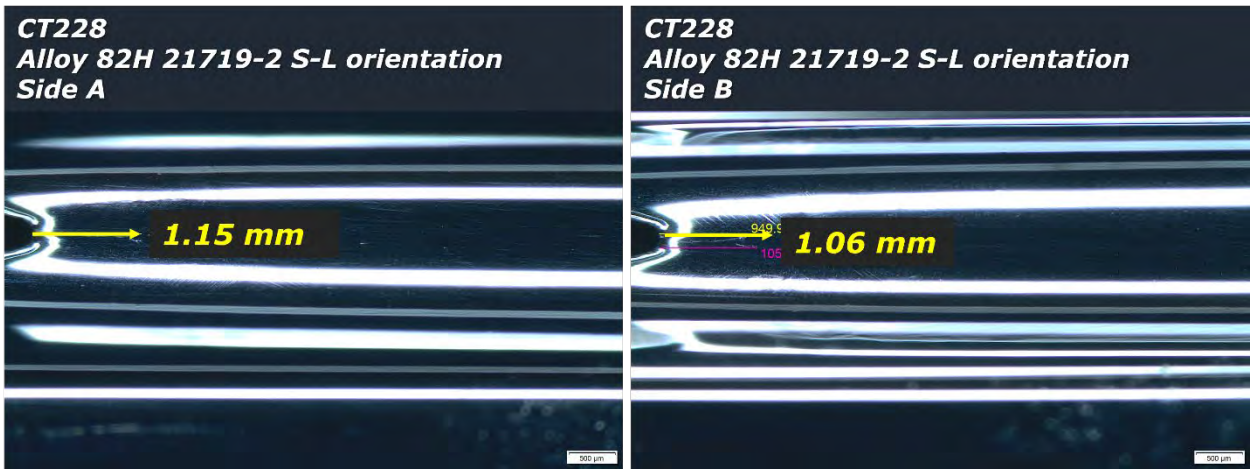

Figure 59. Optical micrographs of the polished side grooves of the Alloy 82H specimen CT228. The length of the precrack produced by air fatigue is marked in both side grooves.

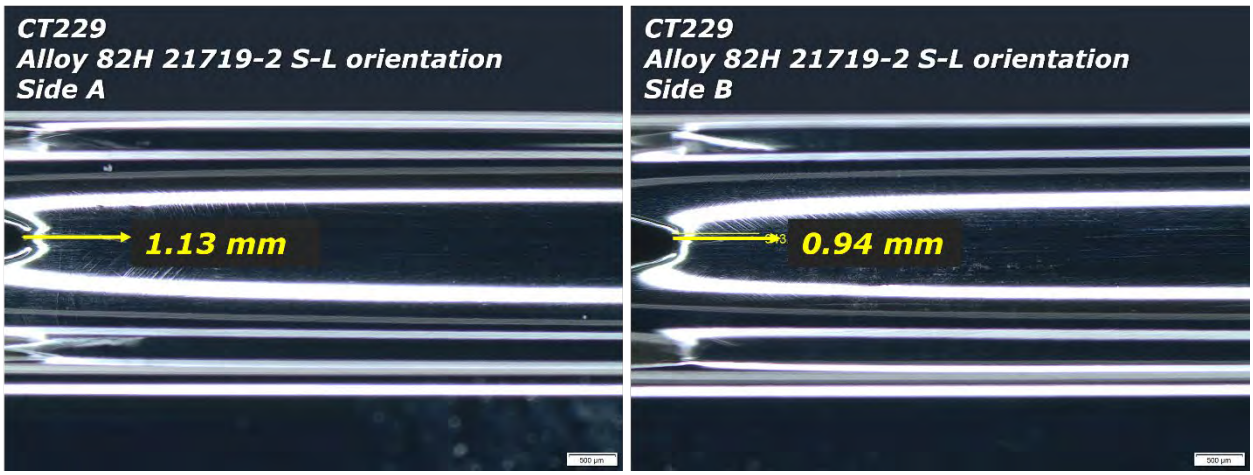

Figure 60. Optical micrographs of the polished side grooves of the Alloy 82H specimen CT229. The length of the precrack produced by air fatigue is marked in both side grooves.

A test overview is presented in Figure 61. Currently, SCCGR evaluation has been completed in the BOC water chemistry, while the assessment in EOC water chemistry is underway. Figure 62 presents the initial cyclic loading steps implemented with decreasing frequency to transition the TG precrack produced by air fatigue to an IGSCC crack front. This includes cyclic loading from 1.0 to 0.01 Hz at a load ratio of 0.5 and a K_{max} of 30 MPa$\sqrt{m}$, followed by a final cycling step of a 980 s rise and a 20 s fall (0.001 Hz) with R = 0.5 in a sawtooth form. Decreasing CGRs were observed for both specimens as the cycling reduced in frequency. As shown in Figure 63, the CGR of both specimens was a little low at the initial cycle+hold step, which may result in SCCGR values that are too low to be used for justifiable evaluation of water chemistry changes after the transition to constant load. Therefore, we went back one step and reduced the load ratio from 0.5 to 0.3, advanced the crack in both specimens for ~250 µm, and then transitioned back to cycle+hold. This time the CGR values for both specimens reached above 10^{-7} mm/s, which were considered more desirable (Figure 63). Hence, the test proceeded to constant load condition for the KOH vs. LiOH effect evaluation in BOC water chemistry.

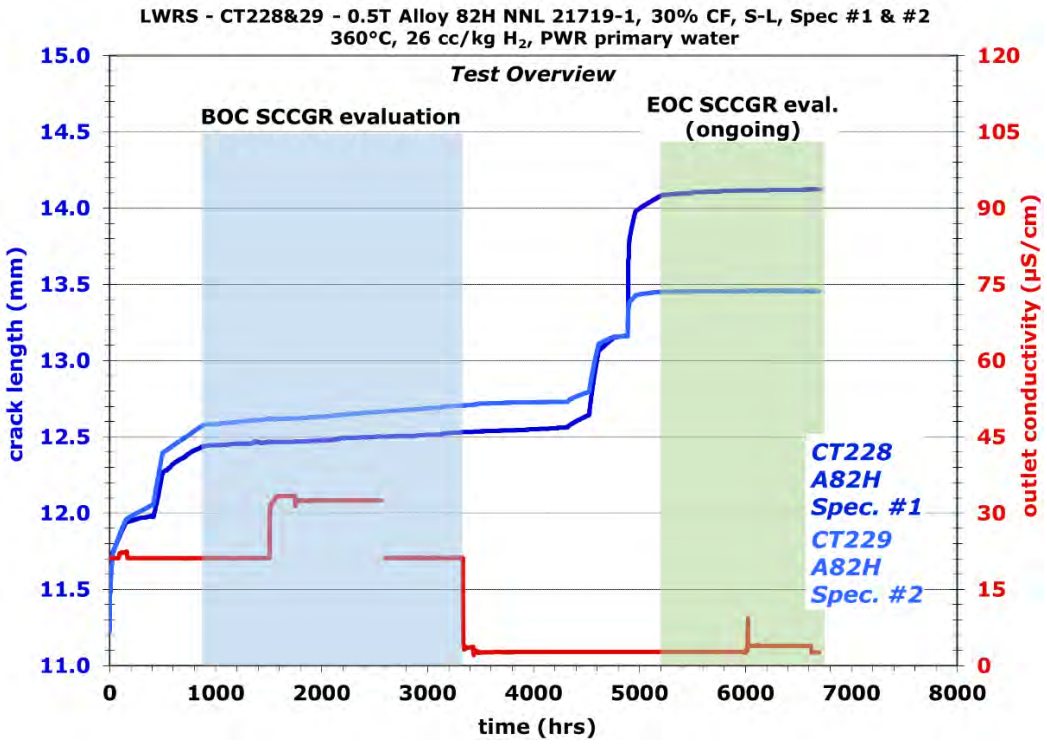

Figure 61. Test overview of crack growth response in the two Alloy 82H specimens CT228 & 229 tested in S-L orientation. The effect of KOH vs. LiOH on the SCCGR of both specimens is evaluated in 360°C simulated PWR primary water at 25 cc/kg H_2 at a constant load of 30 MPa√m. The test is ongoing as of July 2022.

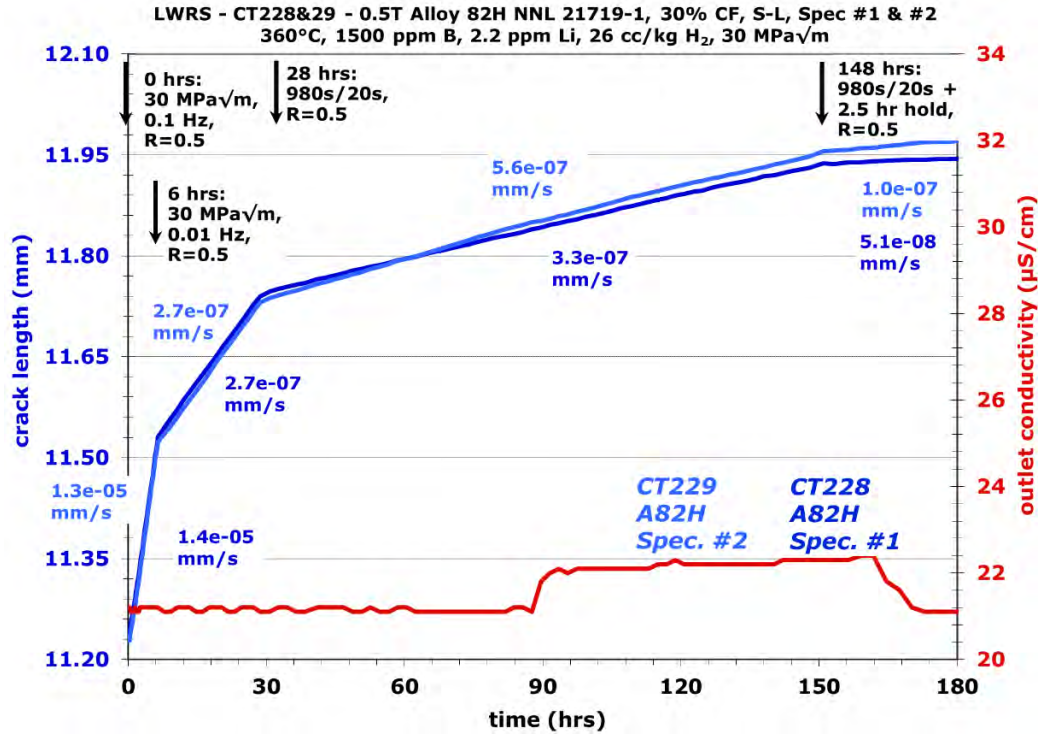

Figure 62. Crack growth response of the two Alloy 82H specimens CT228 & 229 during initial cyclic loading transition steps in 360°C simulated PWR primary water.

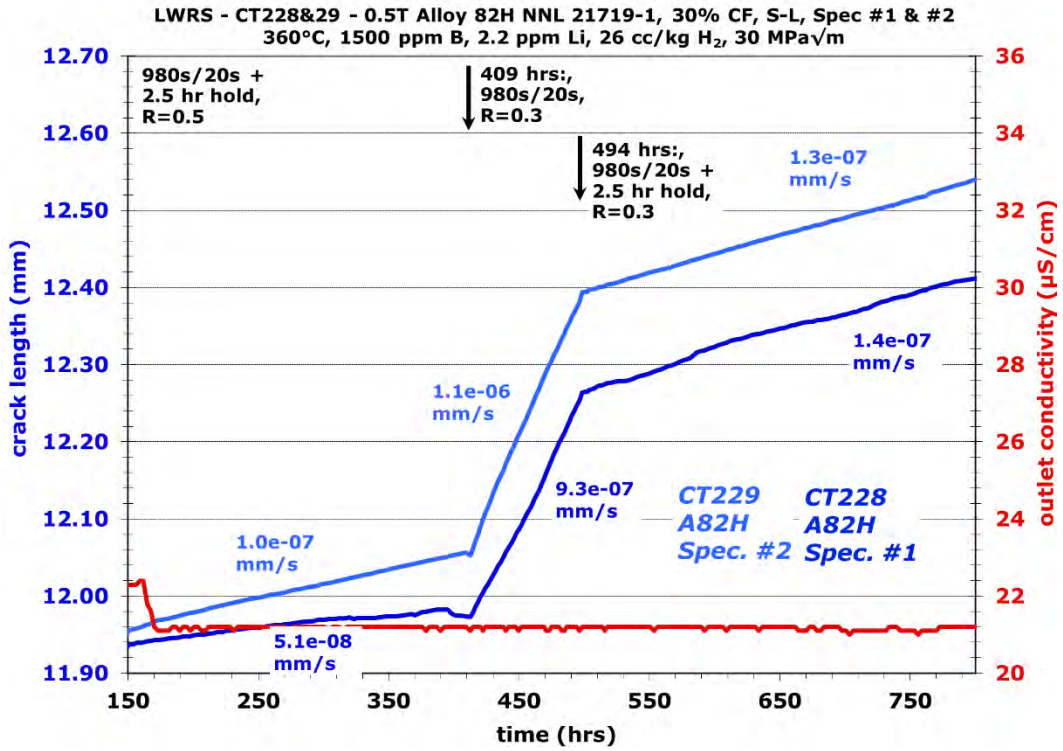

Figure 63. Crack growth response of the two Alloy 82H specimens CT228 & 229 during R adjustment in the initial cyclic loading transition steps in 360°C simulated PWR primary water.

The SCCGR response of CT228 and CT229 during the entire BOC water chemistry evaluation is provided in Figure 64. The test started in the BOC-LiOH condition as specified in Table 1, moved to the BOC-KOH condition, and then returned to BOC-LiOH for a final assessment. Because Ni-base weld metals are known to exhibit variability in CGR response, a longer evaluation time (>720 hours) was given for each step to allow sufficient data to be collected for assessing specimens' CGR response. While local variation in SCCGR was observed in both specimens, the difference in the average SCCGR at each neighboring step is within 10% for CT228 and 20% for CT229, which are well within the variability in CGR of weld metals. Therefore, it is concluded that the change between KOH and LiOH in the BOC water chemistry does not alter the SCC response of the investigated weld metal.

As shown in Figure 65, the test moved on to assess the SCCGR behavior of CT228 and CT229 in EOC water chemistry right after the completion of assessments in the BOC water chemistry. Only the water chemistry was adjusted on-the-fly while the load was maintained at 30 MPa√m. However, the SCCGR gradually increased in CT228 while continuously decreased in CT229 to 2.1×10^{-9} mm/s, a value that indicates little growth after ~700 hours in the EOC-LiOH water chemistry. Based on our experience with SCC growth rate testing, uneven, fingered growth along dendritic grain boundaries is a common phenomenon in Ni-base weld metals. The observed SCCGR reduction in CT229 is more likely associated with the crack front reaching a local microstructure of more SCC resistance (either microchemically or geometrically, or both) rather than the change in water chemistry. Therefore, aggressive cycling was applied in an attempt to grow the crack in both specimens for ~500 µm (Figure 66). This was considered as a sufficiently long distance to move the crack front out to a new area and straighten the crack front for subsequent SCCGR assessments. However, as shown in Figure 67, the SCCGR of CT229 was essentially unchanged after the test returned to constant load. In comparison, the SCCGR for CT228 was ~10X higher. As a result, another series of aggressive cycling steps were implemented to ameliorate this difference (Figure 68). Unfortunately, no improvement was achieved with one order of difference observed in the CGR values for CT228 and CT229 at the cycle+hold step. Nevertheless, since the

cycle+hold CGR for CT228 was acceptable, it was decided to continue the test in EOC water chemistry and only use data acquired on CT228 for the subsequent KOH vs. LiOH SCCGR assessment. However, as can be seen in Figure 69, a jump occurred in the crack length of CT228 at 5,500 hours, and the SCCGR continued to decrease starting from that point to essentially no growth after the most recent water chemistry change at 6,640 hours. Again, the decreasing SCCGR is suspected to be associated with crack front morphology/location instead of the implemented water chemistry changes. Therefore, CT228 and CT229 have been temporarily removed from the test for crack length adjustment by applying cyclic loading in air. This will allow us to move the crack front out of the current trapped area in both specimens and bring them to a similar length so that we can continue SCCGR evaluation in subsequent water chemistries on both specimens. As of the writing of this report, this effort is ongoing and progress will be included in future reports.

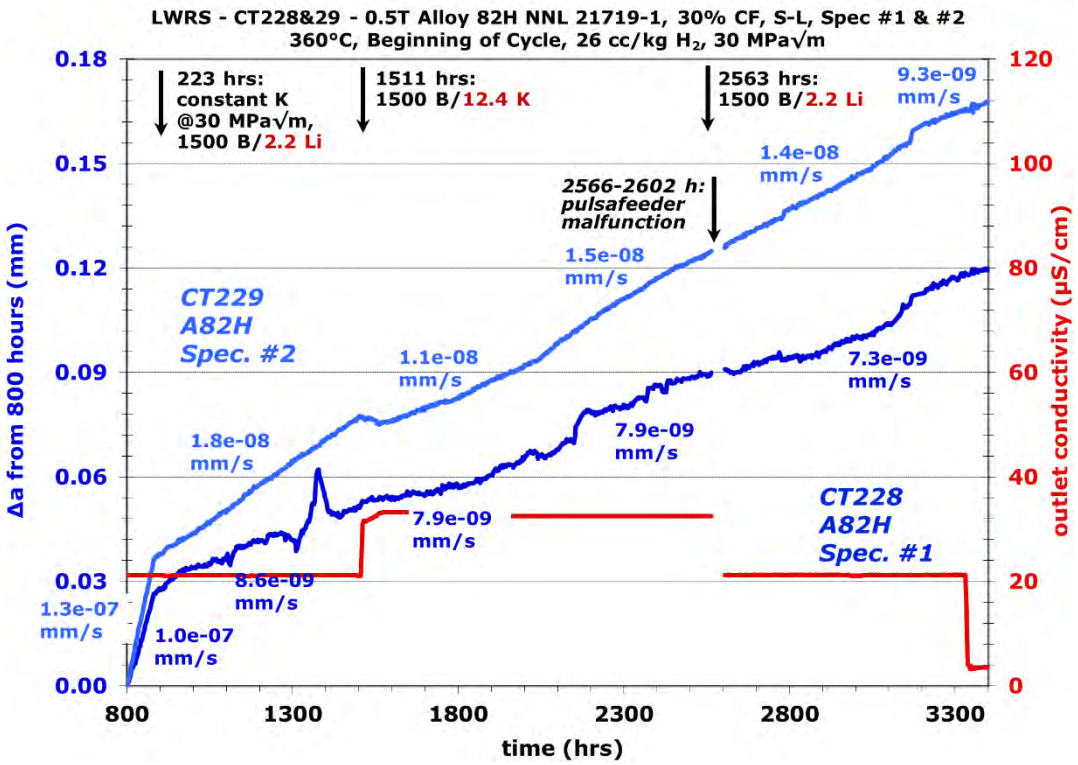

Figure 64. SCCGR response of the two Alloy 82H specimens CT228 & 229 in 360°C PWR primary water BOC chemistry with on-the-fly changes between LiOH and KOH.

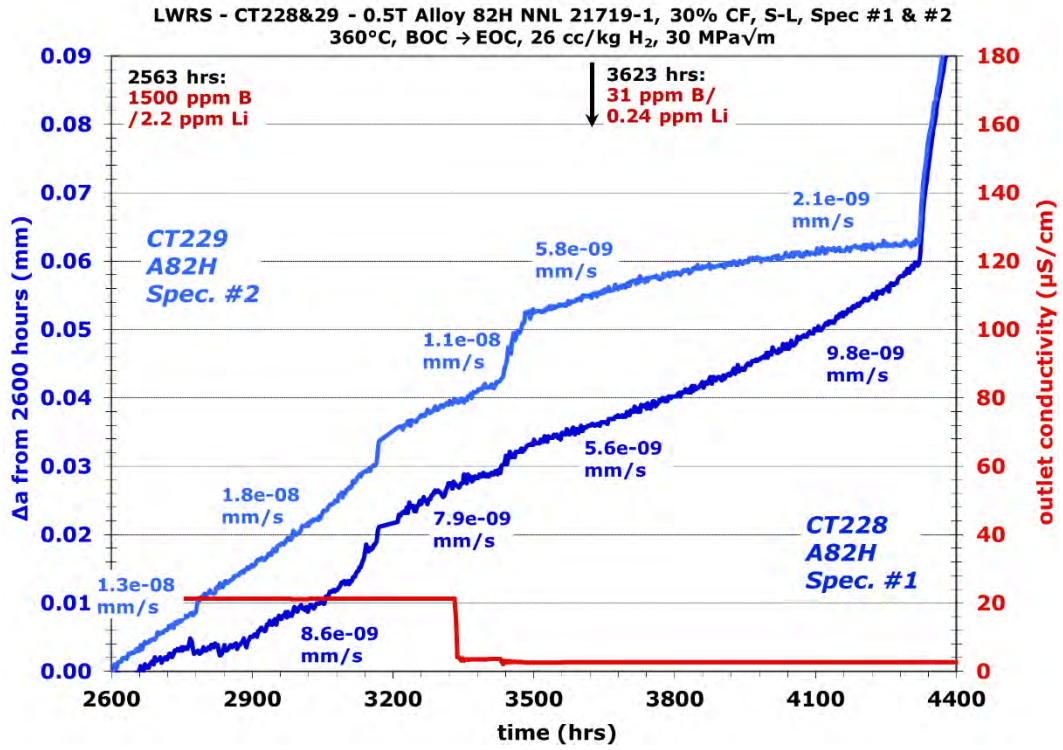

Figure 65. SCCGR response of the two Alloy 82H specimens CT228 & 229 in transition from BOC-LiOH water chemistry to the first EOC-LiOH water chemistry in 360°C PWR primary water.

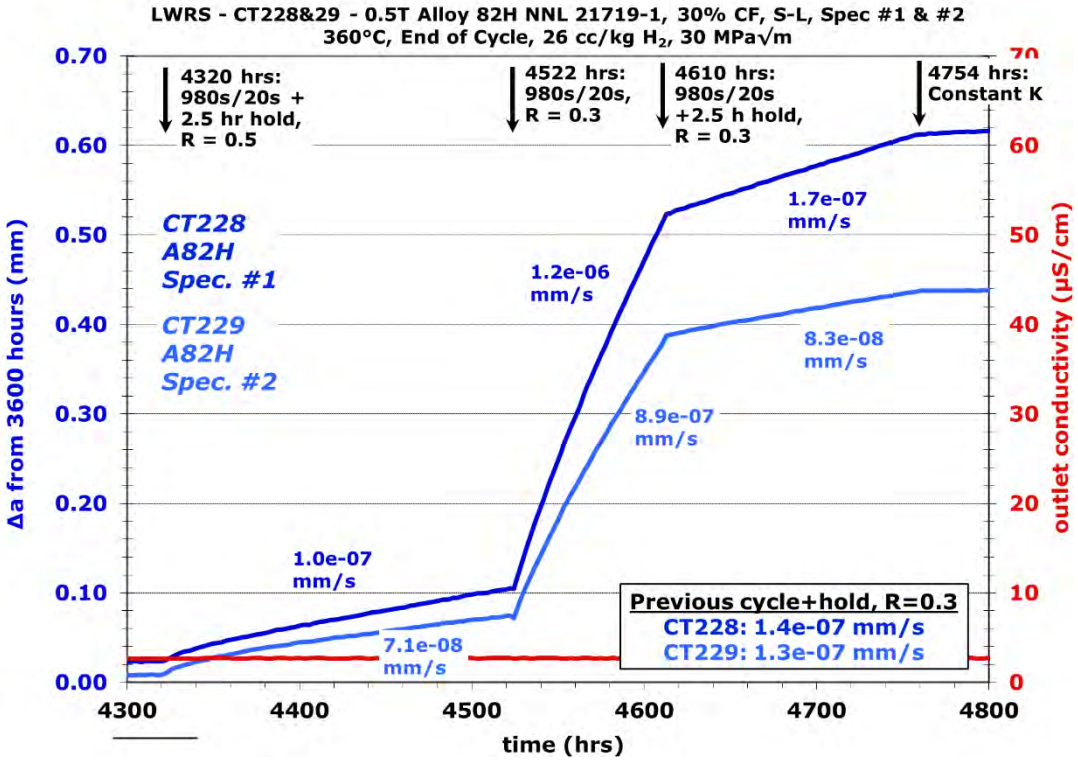

Figure 66. Crack growth response of the two Alloy 82H specimens CT228 & 229 during cyclic loading transition steps in an attempt to reactivate crack growth in CT229.

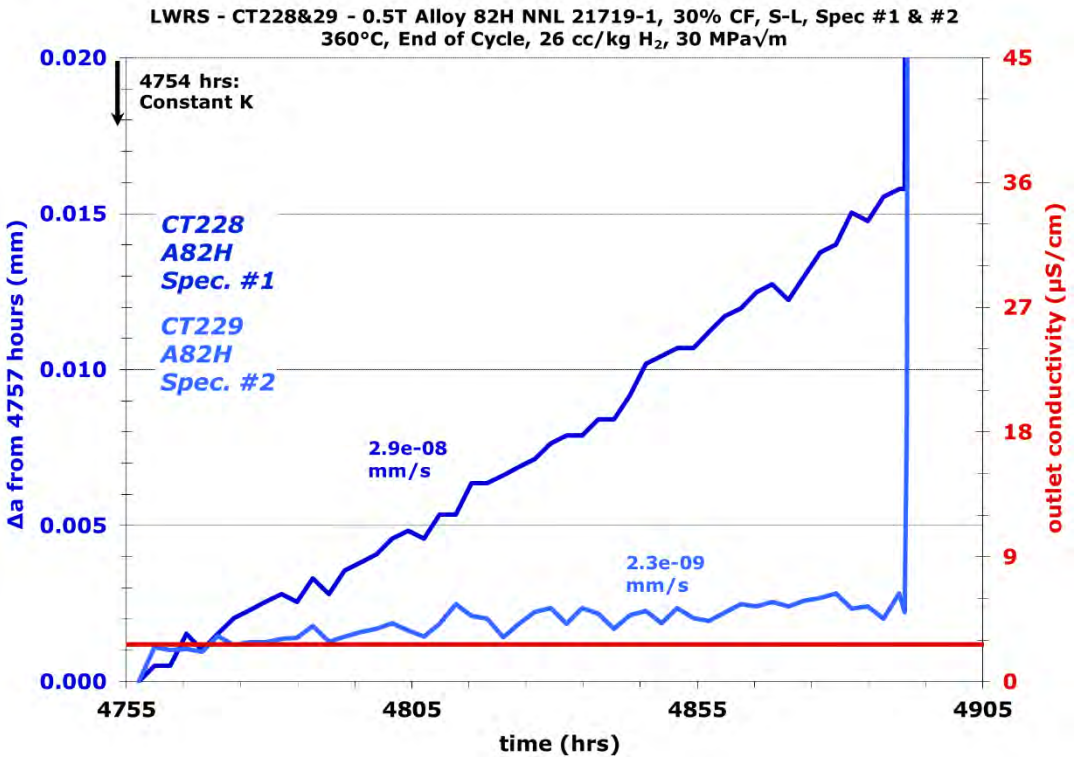

Figure 67. SCCGR response of the two Alloy 82H specimens CT228 & 229 in EOC-LiOH water chemistry after retransitioning.

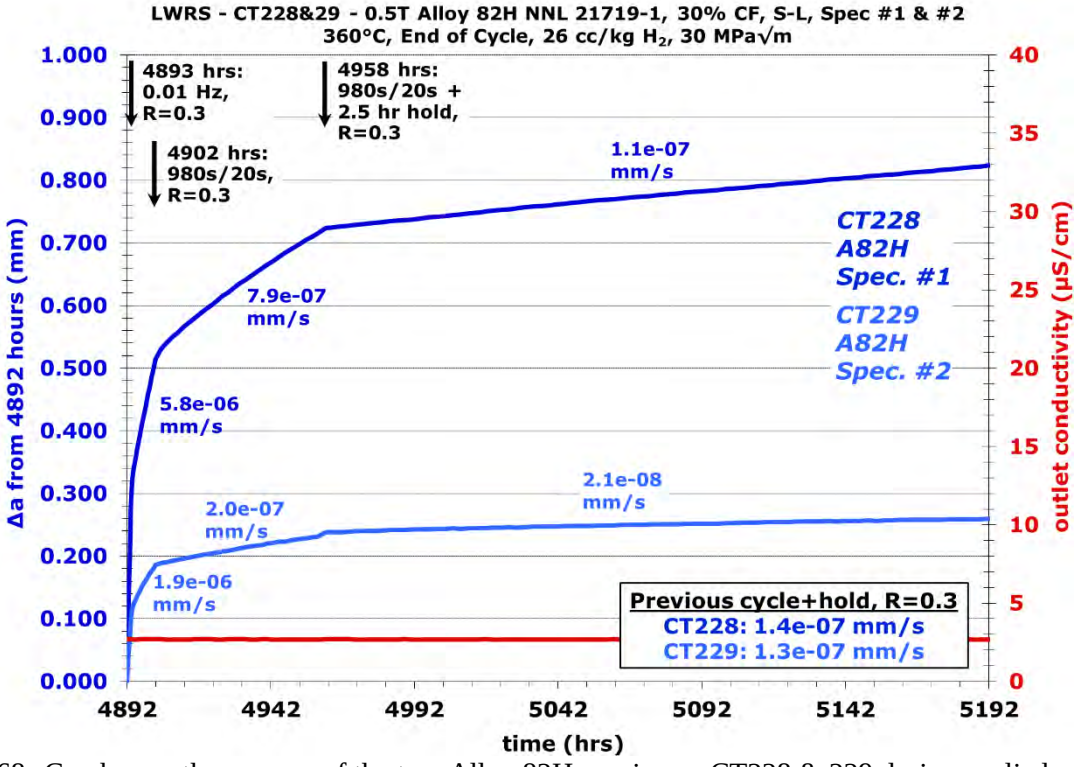

Figure 68. Crack growth response of the two Alloy 82H specimens CT228 & 229 during cyclic loading transition steps in the second attempt to reactivate crack growth in CT229.

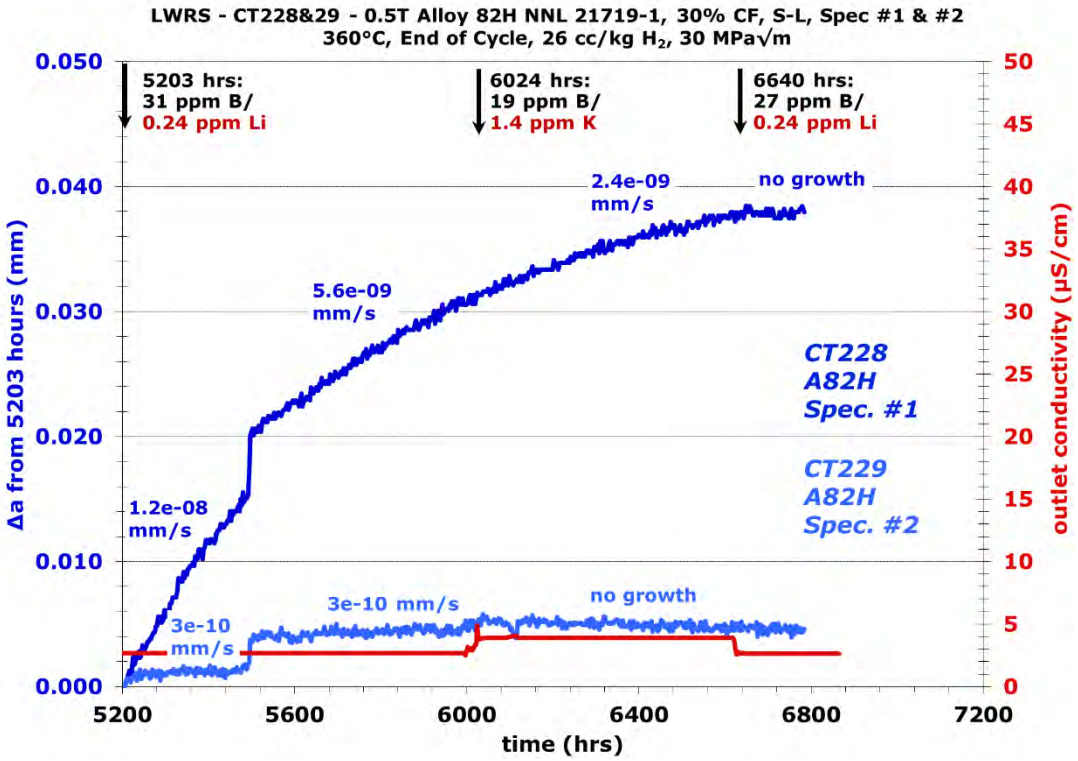

Figure 69. SCCGR response of the two Alloy 82H specimens CT228 & 229 in 360°C PWR primary water EOC chemistry with on-the-fly changes between LiOH and KOH.

7. SUMMARY

The cost and availability of Li-7 is creating interest in using KOH to replace LiOH for primary system pH control in PWRs. A key concern regarding the use of KOH is its potential effect on the structural materials employed in the reactor internals, especially on Ni-base alloys where there is limited prior experience with exposure to KOH water chemistry. In collaboration with an ongoing EPRI-led qualification program to determine if KOH PWR water chemistry is acceptable from a materials degradation perspective as compared to LiOH PWR water chemistry, PNNL is performing supporting tests under LWRS to investigate whether replacing LiOH with KOH has a negative impact on the SCC behavior of Ni-base alloys. The testing materials and water chemistries were determined together with EPRI. In FY22, this study focuses on SCC growth rate testing of the high-strength Ni-base Alloy X-750 and Alloy 718, and Alloy 82H, a compatible weld metal for Alloy 600.

To date, SCC growth rate testing has been completed for Alloy X-750 and Alloy 718 in all three water chemistries specified by EPRI (BOC, EOC, and mid-cycle), and the testing in Alloy 82H is ongoing (assessment in BOC water chemistry completed). For Alloy X-750, two specimens were tested in the T-L orientation at a constant load of 20 MPa$\sqrt{m}$ in 325°C PWR primary water with either 29 or 9.6 cc/kg H_2. For Alloy 718, two precipitation-hardened specimens were tested in the S-L orientation at a constant load of 25 MPa$\sqrt{m}$ in 360°C PWR primary water with 26 cc/kg H_2. For Alloy 82H, two specimens are being evaluated in ~30% cold forged condition in the S-L orientation in 360°C PWR primary water with 26 cc/kg H_2. The effect of LiOH vs. KOH was evaluated by monitoring the crack extension using a highly refined DCPD method during on-the-fly changes between LiOH and KOH to the content specified by EPRI for the BOC, EOC, and mid-cycle PWR primary water chemistries. In the BOC and EOC water chemistries, the assessment usually began with LiOH, proceeded to KOH, then returned to LiOH to confirm behavior. SCCGRs were collected right before and after each water chemistry change, and also after the crack had spent sufficiently long time in each specified water chemistry so that an average SCCGR could be determined. Comparing these data revealed no obvious change in SCCGR in KOH vs. LiOH in each water chemistry, nor on shifting from BOC, EOC, and mid-cycle water chemistries. These results suggest that replacing LiOH with KOH would not adversely impact the SCC growth susceptibility of the tested materials in PWR primary water.

REFERENCES

[1] P. Chou, J. Smith, A. Demma, M. Burke, K. Fruzzetti, Potassium Hydroxide for PWR Primary Coolant pH Control: Materials Qualification Testing, in: 21st NPC International Conference on Water Chemistry in Nuclear Reactor Systems, 2018, pp.

[2] K. Fruzzetti, A. Demma, P. Chou, J. Smith, D. Hussey, K. Kim, C. Gregorich, M. Burke, Potassium Hydroxide for PWR Primary Coolant pH Control: Qualification Program, in: 21st NPC International Conference on Water Chemistry in Nuclear Reactor Systems, 2018, pp.

[3] P. Andresen, P. Chou, SCC initiation and growth in PWR primary water containing KOH vs. LioH, in: 19th International Conference on Environmental Degradation of Materials in Nuclear Power Systems - Water Reactors, American Nuclear Society, 2019, pp. 363-372.

[4] M.B. Toloczko, N.R. Overman, M.J. Olszta, S.M. Bruemmer, Pacific Northwest National Laboratory Investigation of Stress Corrosion Cracking in Nickel-Base Alloys, Volume 3: Stress Corrosion Cracking of Cold-Worked Alloy 690, NUREG/CR-7103 Vol. 3, Nuclear Regulatory Commission, Office of Nuclear Regulatory Research, 2015.

[5] P.L. Andresen, J. Flores-Preciado, M.M. Morra, R. Carter, Microstructure and SCC of alloy X-750, in: 15th International Conference on Environmental Degradation of Materials in Nuclear Power Systems-Water Reactors, John Wiley and Sons Inc., 2011, pp. 679-700.

[6] J.H. Jackson, S.P. Teysseyre, Baseline Fracture Toughness and CGR Testing of Alloys X-750 and XM-19 (EPRI Phase I), INL/EXT-11-24173, February 2012.

[7] A.A. Stein, M.S. Gennaro, Material specification for Alloy X-750 for use in LWR internal components, EPRI Report NP-7032, 1990.

[8] C. Benhamou, J.L. Chambrin, P. Todeschini, J. Champredonde, E. Lemaire, Evolution de la conception, de la fabrication et du montage des broches de fixation des tubes guides de grappes en Alliage X750, in: Proceedings Convention Nationale SFEN, 2004, pp.

[9] M.M. Morra, BWRVIP-240: BWR Vessel and Internals Project, Metallurgical Analyses and Macro and Microstructural Mapping of Alloy X-750 and Alloy XM-19 Plates, EPRI Report 1021003, August 2010.

[10] Alloy 718 Review for Fuel Assembly Applications, EPRI, Palo Alto, CA: 2013. 3002002176., December 2013.

[11] M.T. Miglin, J.V. Monter, C.S. Wade, J.K. Tien, J.L. Nelson, Stress corrosion cracking of chemistry and heat treat variants of alloy 718. Part 1: Stress corrosion test results, in: 6th International Symposium on Environmental Degradation of Materials in Nuclear Power Systems - Water Reactors, The Minerals, Metals & Materials Society (TMS), 1993, pp. 815-819.

[12] M. Wang, M. Song, G.S. Was, J.L. Nelson, The roles of thermal mechanical treatment and δ phase in the stress corrosion cracking of alloy 718 in primary water, Corrosion Science, 160 (2019) 108168.

[13] P.M. Scott, 2000 F.N. Speller Award Lecture: Stress Corrosion Cracking in Pressurized Water Reactors—Interpretation, Modeling, and Remedies, Corrosion (Houston), 56 (2000) 771-782.

[14] S. International, AMS5596 - Nickel Alloy, Corrosion and Heat-Resistant, Sheet, Strip, Foil and Plate 52.5Ni-19Cr-3.0Mo-5.1Cb (Nb)-0.90Ti-0.50Al-18Fe Consumable Electrode Remelted or Vacuum Induction Melted 1775 °F (968 °C) Solution Heat Treated, in, 1964.

[15] S. International, AMS5663 - Nickel Alloy, Corrosion and Heat Resistant, Bars, Forgings, and Rings 52.5Ni-19Cr-3.0Mo-5.1Cb(Nb)-0.90Ti-0.50Al-19Fe, Consumable Electrode or Vacuum Induction Melted 1775°F (968°C) Solution and Precipitation Heat Treated, in, 1965.

[16] Z. Zhai, M.J. Olszta, M.B. Toloczko, Quantitative Analysis of Precursor Damage and Crack Evolution in Alloy 690 and Its Weld Metals after Long-Term SCC Initiation Testing in PWR Primary Water, Pacific Northwest National Laboratory: Technical Milestone Report M3LW-21OR0402033, Light Water Reactor Sustainability Program, DOE Office of Nuclear Energy, April 2021.

[17] P.L. Andresen, Materials Reliability Program: Effects of B/Li/pH on PWSCC Growth Rates in Ni-Base Alloys (MRP-217), EPRI, Palo Alto, CA: 2007. 1015008., 2007.

[18] P.L. Andresen, J. Hickling, K.S. Ahluwalia, J.A. Wilson, Effects of PWR primary water chemistry on PWSCC of Ni alloys, in: 13th International Conference on Environmental Degradation of Materials in Nuclear Power Systems - Water Reactors, Canadian Nuclear Society, 2007, pp. 1393-1413.